Invasive intracranial pressure monitor system: passive wireless LC sensor design and its novel read out circuit

By

Fa Wang

A dissertation submitted in partial fulfillment of

the requirements for the degree of

Doctor of Philosophy

(Electrical Engineering)

at the

UNIVERSITY OF WISCONSIN-MADISON

2017

Date of final oral examination: 05/10/2017

The dissertation is approved by the following members of the Final Oral Committee:

Yuhen Hu, Professor, Electrical and computer engineering

John G Webster, Professor, Biomedical Engineering

Bermans J. Iskandar, Professor, Neurological Surgery

Joshua E. Medow, Associate Professor, Neurological Surgery

Walter Block, Professor, Biomedical Engineering

Abstract:

Head trauma, hydrocephalus, intracranial tumors, hepatic encephalopathy, and cerebral edema cause increased intracranial pressure (ICP). Early and timely detection of elevated ICP is very important to mitigate symptoms during the entire life of the patient to avoid headaches, mental disability and death caused by abnormal increased ICP. We present a wide frequency range, low cost, wireless intracranial pressure (ICP) monitoring system, which includes an implantable passive sensor, and an external reader. The passive sensor consists of two spiral coils and transduces the pressure change to a resonant frequency shift. The improved circuit model and design process of this sensor are given. The external portable reader reads out the sensor's resonant frequency over a wide frequency range (35 MHz to 2.7 GHz). We propose a novel circuit topology, which tracks the system's impedance and phase change at a high frequency with low cost components. This circuit is very simple and reliable. A prototype was developed, and measurement results demonstrate that the device achieves a suitable measurement distance (>2 cm), sufficient sample frequency (>6 Hz), fine resolution, and good measurement accuracy for medical practice. Responsivity of this prototype is 0.92 MHz/mmHg and resolution is 0.001.84mmHg. COMSOL Specific absorption rate (SAR) simulation proves this system is safe.

Acknowledgments

I would like to express my special appreciation and thanks to my advisor Professor John Webster, I would like to thank you for encouraging my research and for allowing me to grow as a research scientist. I would also like to thank my committee members and project PI, Professor Bermans J. Iskandar and Professor Joshua E. Medow, thank you for supporting me and guide me in the past years. I also would like thank committee member Professor Yuhen Hu and Professor Walter Block, for letting my defense be an enjoyable moment, and for your brilliant comments and suggestions, thanks to you.

Special thanks send to my family. Words cannot express how grateful I am to my mother, my father for all of the sacrifices that you've made on my behalf since I was a little kid. Very special appreciation to my beloved wife and best friend Jiayang who spent sleepless nights and was always in my support.

I should also say thank you to my colleagues, Mehdi and Xuan. I really enjoy the time working with in this six years.

Contents

GLOSSARY

ABP	Arterial Blood Pressure
aICP	absolute ICP
AP	Arterial Pressure
CA	Cerebrovascular Autoregulation
CBFV	Cerebral Blood Flow Velocity
CBV	Cerebral Blood Volume
cICC	continuous Intracranial Compliance
CNS	Central Nervous System
CPP	Cerebral Perfusion Pressure
CSF	Cerebrospinal Fluid
CSFP	CSF Pressure
CT	Computed Tomography
CVR	Cerebrovascular Resistance
DPOAE	Distortion-product OAE
EEG	Electroencephalography
EVD	External Ventricular Drainage
FEM	Finite-element Model
FV	Flow Velocity
FVEP	Flash Visual-evoked Potential
IBV	Intracranial Blood Volume
ICH	Intracerebral Hemorrhage
ICP	Intracranial Pressure
IH	Intracranial Hypertension
IIH	Idiopathic Intracranial Hypertension
IOP	Intraocular pressure
LD	Lumbar Drain
LP	Lumbar Puncture
MAP	Mean Arterial blood Pressure

MCA	Middle Cerebral Artery
MEMs	Microelectromechanical Systems
MRI	Magnetic Resonance Imaging
MWA	Mean Wave Amplitude
nCPP	noninvasive determination of CPP
NFC	Near-field Communication
nICP	noninvasive ICP
NIH	National Institutes of Health
NIRS	Near-infrared Spectroscopy
OAE	Otoacoustic Emissions
OAEs	Otoacoustic Acoustic Emissions
OCT	Optical Coherence Tomography
ODM	Ophthalmodynamometry
ONSD	Optic Nerve Sheath Diameter
PDMS	Poly (Dimethyl Siloxane)
PHCH	Post-hemorrhagic Communicating Hydrocephalus
PI	Pulsatility Index
PLGA	Poly (Lactic-co-glycolic) Acid
RF	Radio Frequency
RNFL	Retinal Nerve Fiber Layer
ROC	Receiver Operating Characteristic
RPE	Retinal Pigment Epithelium
SAH	Subarachnoid Hemorrhage
SBS	Styrene-butadiene-styrene
SD	Standard Deviation
SDE	SD of Error
SPL	Sound Pressure Level
SVPs	Spontaneous Venous Pulsations
TCBF	Total Cerebral Blood Flow

TCD	Transcranial Doppler
TMD	Tympanic Membrane Displacement
TRA	Tissue Resonance Analysis
TST	Trans Systolic Time
VEP	Visual Evoked Potentials
VOP	Venous Outflow Pressure
VP	Ventriculoperitoneal

CHARPTER 1: INTRODUCTION

This chapter 1 is partly taken from:

Xuan Zhang, Joshua E. Medow, Bermans J. Iskandar, Fa Wang, Mehdi Shokoueinejad, Joyce Koueik, and John G. Webster. Invasive and noninvasive means of measuring intracranial pressure: A review May.2017 Physiol. Meas.

1.1 Background and motivation

Hydrocephalus is a medical condition in which there is excessive accumulation of cerebrospinal fluid (CSF), leading to an abnormal increase of intracranial pressure (ICP). Hydrocephalus occurs in children and adults, and is often congenital. It affects 1 to 2 of every 1000 live births, making it by far the leading cause of brain surgery in US children. The National Institutes of Health (NIH) estimates that 700,000 children and adults live with hydrocephalus, but less than 20% are properly diagnosed. The medical cost of hydrocephalus is over US$ 1 billion per year. Since CSF shunting was introduced in the early 1900s and one-way valve systems in the 1950s, countless lives have been saved. However, CSF shunt systems have not been significantly improved in the past 60 years. We need better treatment, more positive long-term monitoring, and diagnostic tests that are accurate, low cost, and noninvasive (Hydrocephalus Association 2016).

Abnormal CSF accumulation can cause headaches, mental disability, and death. Once the disease is identified treatment may consist of endoscopic techniques to restore adequate CSF flow, or the placing of a ventriculoperitoneal (VP) shunt to relieve the elevated ICP by shunting the fluid to other bodily cavities such as the pleural space, cardiac atrium or, most commonly, peritoneum. Timely detection of elevated ICP is essential to reduce the risk of permanent brain damage and is very important to ease hydrocephalus symptoms during the life of the patient.

1.2 Physiology and pathophysiology of intracranial pressure

Intracranial pressure is the pressure inside the brain. Its value is conventionally referenced to atmospheric pressure and expressed in mmHg. Normal ICP varies with age and body posture but is maintained in the range 5 to 15 mmHg in healthy supine adults, 3 to 7 mmHg in children, and 1.5 to 6 mmHg in term infants (Smith et al. 2008, Raboel et al. 2012).

The ICP value is significantly influenced by volume equilibrium within the brain (1100 to 1300 cm^3), CSF (130 to 150 cm^3), and blood contained in intracranial vessels (60 to 80 cm^3). Considering that brain volume is fixed, CSF and blood are the two most important determining factors of ICP. Cerebral blood flow is nearly constant and is based on mean blood pressure. If an imbalance occurs between the production of CSF in the brain ventricles and its absorption into the dural venous sinuses, abnormal ICP results (Mokri 2001, Popovic et al. 2009).

Cerebral perfusion pressure (CPP), the pressure of blood in the brain, is normally fairly constant in healthy people due to auto-regulation (Steiner and Andrews 2006). CPP is defined as the difference between mean arterial blood pressure (MAP) and ICP (CPP = MAP – ICP). In cases of elevated ICP, the CPP decreases. When treating increased ICP, CPP is therefore an important parameter to monitor and maintain (Steiner and Andrews 2006, Duschek and Schandry 2007).

Elevated ICP occurs in a variety of medical conditions. Frequent causes include intracranial mass lesions, disorders of CSF circulation such as hydrocephalus, more diffuse pathological processes, and head injury leading to intracranial hematoma or cerebral edema. Elevated ICP can compress and damage brain structures, cause brain herniation, and restrict blood supply to the brain (Graham et al. 2000, Steiner and Andrews 2006).

1.3 Role of ICP monitoring in current clinical practice

ICP monitoring plays an important role in various medical conditions. ICP monitoring is an important tool in clinical practice to determine brain pressure and compliance (Di Ieva et al.

2013). Currently, this area lacks universally accepted guidelines, and hospitals use different standards of ICP monitoring (Raboel et al. 2012).

Continuous ICP monitoring is utilized in the management of severe closed head injury in adults and children (Dunn 2002), subarachnoid and other brain hemorrhage, meningitis, acute liver failure causing cerebral edema, stroke, benign intracranial hypertension, and head shape deformities (craniosynostosis), as well as hydrocephalus and CSF shunt function (Czosnyka and Pickard 2004).

There is now a great need to study and integrate ICP monitoring into a multimodality and individualized approach to clinical care (Hawthorne and Piper 2014) with patient-specific parameters for ICP and CPP. Even more important, however, is to develop noninvasive ICP monitors, an essential future direction that is yet poorly supported by technology (Di Leva et al. 2013, Hawthorne and Piper 2014). The current ICP monitoring systems are invasive, and require opening of the skull and the implanting of sensors with wires or catheters, exiting the skin to connect to various monitors.

1.4 Complications of intracranial pressure monitoring

ICP monitoring complications include disconnection, device failure, infection, and hemorrhage. Ventricular-catheter related infection rates are around 10% and are associated with the duration of catheter placement (Fried 2016, Lozier 2002). The use of antibiotic impregnated catheters can potentially reduce the risk of infection by prolonging the mean duration to onset of infection (Fried 2016). Clinically symptomatic hemorrhages due to the catheter range from 0.7% to 2.4% (Fried 2016).

CHARPTER 2: CURRENT ICP MEASUREMENT METHOD

This chapter 2 is partly taken from:

Xuan Zhang, Joshua E. Medow, Bermans J. Iskandar, Fa Wang, Mehdi Shokoueinejad, Joyce Koueik, and John G. Webster. Invasive and noninvasive means of measuring intracranial pressure: A review May.2017 Physiol. Meas.

2.1 Invasive ICP monitor.

The invasive method is the standard technique for direct ICP monitoring. Several different invasive ICP measuring methods exist. ICP measurement can be undertaken at various intracranial anatomical locations determined by different techniques: intraventricular, epidural, subdural, subarachnoidal, and intraparenchymal. Furthermore, under certain circumstances ICP may be assessed by lumbar puncture for patients with communicating CSF pathways (Eide and Brean 2006, Lenfeldt et al. 2007, Speck et al. 2011).

ICP can be measured at different sites of the brain. Intraventricular and intraparenchymal measurements are more common, whereas extradural and subdural measurements are only rarely used. The standard technique is an invasive procedure that involves catheter insertion into the intracranial compartment, usually through a small hole drilled in the skull. A pressure probe/sensor is then advanced through the brain tissue into the ventricular space, or the brain parenchyma, epidural space (between skull and dura), or subdural space (between brain and dura) (Zhong et al. 2003, Ross and Eynon 2005, Rai and Varadan 2010, Kashif et al. 2012).

2.1.1 Lumbar puncture (LP) or lumbar drain

Quincke (1891) introduced the lumbar puncture (LP) technique as a new option to investigate the intrathecal environment. It involves the percutaneous introduction of a needle into the lumbar

spinal CSF space and the measurement of a column of water, which reflects intraspinal pressure. Langfitt et al. (1964) believed that LP could accurately estimate ICP when CSF circulates freely. As mentioned above, under certain circumstances ICP may be assessed by lumbar puncture for patients with communicating CSF pathways. Lumbar puncture is not strictly an ICP measurement, but a neuraxis CSF pressure measurement. Mertz et al. (2004) found that there is a good correlation between the brain sensor's CSF pressure and lumbar pressure. Wiegand and Richards (2007) noted that performing an LP and observing the opening and closing pressure is the most simple and longest-standing ICP measurement method. CSF pressure measured by LP is usually recorded in cmH_2O, whereas ICP is ordinarily measured in mmHg. A conversion factor of 13.6 to convert mmHg to cmH_2O is therefore required.

Kapadia and Jha (1996) showed that, following aneurysm surgery, drainage of lumbar CSF results in an equivalent decrease of both lumbar and ventricular pressures in most patients. Simultaneous measurement of lumbar and ventricular pressures allows the identification of patients at risk of transtentorial or transforamenal herniation following CSF drainage by lumbar puncture, as a pressure gradient between the two cavities starts to build up.

Lumbar drainage (LD) is similar to LP, except that a catheter is placed into the lumbar spinal intrathecal space through a spinal needle before the needle is removed. This allows pressure measurement as well as the ability to drain CSF as needed. Speck et al. (2011) performed a total of 1806 lumbar drain measurements in 43 patients with subarachnoid hemorrhage (SAH, $n = 21$) or intracerebral hemorrhage (ICH, $n = 22$), to assess feasibility and realibility of a lumbar drain when compared to EVD. They showed that LD-ICP recordings correlate well with EVD-ICP recordings, implying that LD an accurate albeit less-invasive option for ICP monitoring in patients suffering from post-hemorrhagic communicating hydrocephalus (PHCH) after SAH and ICH.

Eide and Brean (2006) assessed simultaneous CSF pressure (CSFP)/ICP recordings during lumbar infusion and long-term, overnight ICP monitoring in 27 consecutive idiopathic normal-pressure hydrocephalus patients, recording a total of 35,532 CSFP/ICP wave pairs. The results showed that, during lumbar infusion, the amplitudes of lumbar cerebrospinal fluid pulse pressure could be used to predict the amplitudes of intracranial pulse pressure during long-term, overnight ICP monitoring.

ICP monitoring via LD may have several advantages compared to direct EVD measurement or a parenchymal probe. The major advantage of the LD technique is that lumbar CSF pressure monitoring is less invasive and can be performed at the bedside within minutes (Speck, 2011). Intracranial device placement is always associated with brain injury and hemorrhage risk (Gardner et al. 2009). Additionally, lumbar drainage allows therapeutic CSF release for lowering ICP; this is not feasible with intracranial probes, with the exception of EVD (Münch et al. 2001, Tuettenberg et al. 2009).

LP and LD are not recommended when ICP is suspected to be high from a mass lesion or obstruction because of brain herniation risk (Kashif et al. 2012). Although LP provides a spot estimate of ICP, it cannot capture dynamic ICP trends which are often more accurate indicators of pathology. In addition, LP may give a falsely high reading for children requiring anesthesia or heavy sedation, depending on the different anesthetic agents used and their length of application (Wiegand and Richards 2007). Instant CSF pressure measurement using the height of a fluid column via lumbar puncture may therefore be misleading (Czosnyka and Pickard 2004).

In addition, CSFP data may not reflect ICP, especially in the setting of an obstruction between the intracranial and intraspinal cavities (Eide and Brean 2006). A LP in a patient with such an obstruction can also cause brain herniation because of the difference in pressure between the intracranial and intraspinal compartments. Positioning should also be considered while performing a lumbar puncture. A seated LP can impair the measurement and lead to a falsely high

pressure because of the column of water created in the sitting position. Further research is required to investigate whether lumbar catheter ICP monitoring—with or without CSF release—is safe and accurate in patients with other underlying cerebral diseases. LD is absolutely contraindicated when an intracranial mass lesion is suspected. However, a lumbar puncture may be therapeutic as well as diagnostic in communicating hydrocephalus or benign intracranial hypertension, in which case there is full communication between the ventricular and subarachnoid spaces.

2.1.2 External ventricular drainage (EVD) by catheter

This technique is the original method described for monitoring ICP, and intraventricular catheters are still considered as the gold standard (The Brain Trauma Foundation 2000). A ventricular catheter is placed through a twist drill or burr hole into the ventricle, and CSF pressure is measured via an external pressure sensor.

A significant advantage of this system is that CSF drainage can be used as a therapeutic measure when the ICP is elevated. Currently, systems exist in which catheters and ICP probes are used together as one device, so that ICP can continue to be monitored even if the catheter were to obstruct.

The disadvantages of an EVD are as follows. (1) CSF leakage may lead to falsely low readings. (2) There is a higher risk of CSF infection (up to 10% in some series) and mechanical complications than when using ICP probes (Czosnyka et al. 1996). EVD catheter infections can be mild and easily treatable or can be severe such as meningitis and ventirculitis, causing neurological symptoms and possible death. (3) Incorrect placement can lead to injuries to important cerebral structures such as the internal capsule, thalamus, basal ganglia, and others (Raboel et al. 2012). Saladino et al. (2009) found that, among 138 patients who underwent placement of intra-ventricular catheters for EVD, the rate of mal-placed catheters was 12.3%. (4)

Insertion of the catheter into very small ventricles, often related to brain swelling, may be difficult and more hazardous.

2.2 Noninvasive monitoring of ICP

Several different invasive ICP measurement methods exist, but the development of a noninvasive ICP (nICP) monitoring system with clinically acceptable accuracy is needed. The idea of measuring ICP noninvasively is attractive: (1) to minimize complications in invasive ICP measurement methods such as hemorrhage and infection; and (2) to provide ongoing long-term measurements of ICP without having to insert a new device every time it needs to be measured for clinical changes, a procedure which can only be performed by a neurosurgeon in a specialized facility. Partial information can be obtained using magnetic resonance imaging (MRI), ultrasound, or Doppler flow (Rosenberg et al. 2011).The correlation coefficient between nICP and ICP describes how well ICP can be predicted using nICP. A variety of methods have been suggested for nICP monitoring (Popovic et al. 2009, Kashif et al. 2012), which in general measure physiological variables that indirectly correlate with ICP.

Different numerous non-invasive methods have been proposed and developed for nICP monitoring and are classified in the following five broad categories: Fluid dynamic, Ophthalmic, Otic, Electrophysiologic and Others. Magnetic resonance imaging (MRI), Transcranial Doppler Ultrasonography (TCD), Cerebral blood flow velocity (CBFV), Near-infrared spectroscopy (NIRS), Transcranial time-of-flight are discussed in the Fluid dynamic section. They have been applied to dynamic fluid changes study in ICP, cerebral blood flow and cerebral compliance. Spontaneous venous pulsations (SVPs), Venous ophthalmodynamometry, Optical coherence tomography (OCT) of retina, Optic nerve sheath diameter (ONSD) assessment, and Pupillometry are discussed in the Ophthalmic section. Use of the eye is one possible way for ICP estimation because of the dural extension of the optic nerve sheath and communication between the perioptic nerve CSF and cerebral CSF (Bruce 2014). Sensing tympanic membrane displacement (TMD),

Analyzing otoacoustic emissions (OAE)/acoustic measure and Transcranial acoustic (TCA) signals methods are discussed in the Otic section. The ear has a direct communication with CSF, ear leverage and the cochlear aqueduct help realize connection between the perilymph of the cochlea and posterior cranial fossa CSF for ICP evaluation. Visual-evoked potentials (VEP) and Electroencephalogram (EEG) are discussed in the Electrophysiologic section. ICP has been predicted using nICP from recordings of VEP and EEG methods to record the electrical brain activity and derived ICP levels. Skull vibrations, Brain tissue resonance, and Jugular vein are discussed in the Others section for ICP prediction and evaluation.

2.2.1 Magnetic resonance imaging (MRI)

MRI can be used to measure transcranial blood and CSF volumetric flow rates, which allow the ICP to be determined via an elastance index (Alperin et al. 2000). This method calculates the change of intracranial volume, which is obtained by analyzing the arterial inflow and venous outflow in the brain. The flow is calculated by multiplying the blood velocity and cross-sectional areas of arterial and blood vessels. Velocity is proportional to the difference between the incident and resonant RF signals, and cross-sectional areas are obtained from static MRI scans (Popovic et al. 2009). Normal values have been shown to be a strong predictor of elevated ICP resolution in patients with hydrocephalus without a surgical intervention (Glick et al. 2006), as well as to correlate with the shunt valve opening pressure in children with hydrocephalus (Muehlmann et al. 2013).

Overall, MRI could potentially detect chronic disorders associated with increased ICP values. However, the method is expensive (a basic MRI scan costs over US$1000), cumbersome, and impractical for continuous monitoring of ICP. The equipment is not flexible and portable (Smith 2008); instead, it is heavy and consumes high quantities of energy.

2.2.2 Transcranial Doppler Ultrasonography

Transcranial Doppler (TCD) ultrasonography may be useful for nICP. TCD can measure red cell flow velocity in real time, which can provide an estimate of ICP (Bhatia and Gupta 2007). The TCD technique is developed from basic ultrasound, but minimum probe pressure is required to prevent a decrease in blood flow velocity (Tranquart et al. 2003) when applying ultrasound to measure the blood flow velocity (FV) in the middle cerebral artery (MCA). The ophthalmic artery is affected by the ICP intracranially, and the extracranial segment can be affected by applying pressure externally to the orbit. The pressure cuff is used to gradually compress the orbital tissues, while TCD is used to determine the point at which blood flow in the intra- and extracranial segments of the ophthalmic artery equalize. The externally applied pressure is equal to the ICP at this time (Bruce 2014). ICP can be estimated from the TCD measurements because it impedes the blood flow and consequently decreases the velocity of blood (Popovic et al. 2009).

In spite of the insufficient accuracy of ICP estimates, TCD is still attractive in the area of detecting ischemia when compared to the standard method. TCD is also affordable and mobile, it provides real-time information with high temporal resolution, and is readily available in most hospitals and healthcare facilities. Before it can be recommended for routine use, the TCD technique needs to be evaluated and developed, focusing on its accuracy, cost-effectiveness, and validity.

2.2.3 Cerebral blood flow velocity

Cerebral arterial blood flow velocity is related to both cerebral perfusion pressure (CPP) and cerebrovascular resistance (CVR). CPP is decreased in cases of elevated ICP. CVR is significantly increased as a result of cerebrovascular system compression due to increased ICP. Hanlo et al (1995) defined a new Doppler index, trans systolic time (TST), which reflects specific changes in TCD waveforms induced by changes in the mean ICP. Alperin et al (2005) discussed the postural-related changes in total cerebral blood flow (TCBF) and ICP. An upright position

leads to 12% lower mean TCBF when compared to a supine position. In addition, Asiedu et al (2014) found 58% less CSF, a 2.8 times increase in intracranial compliance, and a corresponding MRI-derived ICP decrease when measured in the seatedposition.

2.2.4 Near-infrared spectroscopy

Near-infrared spectroscopy (NIRS) is commonly used to measure the tissue oxygenation index. It can provide an estimation of cerebral blood volume by recording the concentration of deoxygenated (Hb) and oxygenated (HbO_2) hemoglobin in the blood. It is suitable for continuous detection of cerebral blood volume changes (Zweifel et al. 2010). Weerakkody et al. (2010) discussed the relationship of slow fluctuation in cerebral oximetry detected by NIRS. NIRS allows detection of changes in brain tissue, cerebral blood volume (CBV), and CBF by recording relative Hb and HbO_2 changes associated with slow ventilation. It could be used as a noninvasive marker of increased ICP slow waves.

2.2.5 Transcranial time-of-flight

Ragauskas and Daubaris (1995) first developed transcranial time-of-flight as a brain physiological monitoring technology. Piper (1997) and Ragauskas et al (2003) then discussed the possibility of adding an acoustic path which connects the human head, consisting of brain parenchyma with microvessel arterioles for cerebrovascular autoregulation. This technology is based on the measurement of acoustic properties of the ultrasound speed and ultrasound attenuation inside such a parenchymal acoustic path in the intracranial media. In addition, the majority of patented methods for this technology are based on the assumption that ICP changes affect the physical dimensions and/or acoustic properties (Michaeli and Rappaport 2002, Fountas et al 2005, Popovic et al 2009). The time-of-flight related methods are influenced by the acoustic properties of tissue and fluids in the brain. Changes in the volume of any of these components change the time-of-flight (Ragauskas et al 2003).

2.2.6 Spontaneous venous pulsations

Another method of optic nerve examinations used to approximate ICP is observation of spontaneous venous pulsations (SVPs). SVPs consist of subtle variations in retinal vein caliber seen on the optic disc. Jacks and Miller (2003) described a useful technique in the use of digital pressure on the globe through the eyelid to induce venous pulsations in patients for whom SVPs do not appear to be present. Once venous pulsations are observed at a particular location, the pressure is removed and observation of the area is continued to determine whether venous pulsations, not detected initially, remain.

2.2.7 Venous ophthalmodynamometry

Baurmann (1925) first suggested that the pressure within the central retinal vein depends on ICP. For decades, ophthalmologists have been familiar with ophthalmodynamometry (ODM), a technique that allows the physician to determine pressure within the central retinal vein. Jonas et al (2008) set up an experiment for a 28-year-old female patient with blurred vision and nuchal pain, in which they used prominent optic discs and modified ophthalmodynamometry to determine ICP. ODM showed increased central retinal vein pressure in both eyes which corresponded to elevated cerebrospinal fluid pressure measurements on lumbar puncture; this led to the diagnosis of idiopathic intracranial hypertension, proving that ODM can be helpful in the diagnosis of an elevated ICP.

2.2.8 Optical coherence tomography (OCT) of retina

Intracranial hypertension (IH) causes cellular or axonal level changes such as the swelling of the retinal nerve fiber layer (RNFL) that forms the innermost layer of the retina (Popovic et al 2009). Optical coherence tomography (OCT) measures total retinal thickness, RNFL thickness, and optic nerve head morphology based on infrared light (Hee et al 1995).

2.2.9 Optic nerve sheath diameter (ONSD) assessment

The optic nerve sheath complex consists of the optic nerve, which is a white matter tract of the central nervous system (CNS), and the perioptic nerve sheath, which is formed from the leptomeninges and is continuous with the dura mater of the brain. The sheath around the optic nerve is in fact a continuation of the dura, and the subarachnoid space extends along the optic nerve within the sheath. Optic nerve sheath diameter assessment has been discussed and developed by multiple researchers (e.g., Rajajee et al 2011, Borchert and Lambert 2000). Optic nerve sheath distension occurs within seconds of ICP elevation, making ONSD potentially useful for acute ICP elevation detection. Enlargement of the optic nerve sheath has been described in patients with increased ICP (Soldatos et al. 2008). Raised ICP is transmitted around the optic nerve through the cerebrospinal fluid, causing distention of the optic nerve sheath diameter (ONSD). Previous work has shown that patients with increased ICP have increased ONSDs. Optic nerve sonography offers rapid bedside optic nerve sheath diameter assessment and has been introduced for measuring ICP noninvasively, especially in severe brain injury patients (Tsung et al. 2008). High-resolution MRI has also been used to estimate the optic nerve and its sheath for evidence of elevated ICP (Rosenberg et al 2011). Transorbital sonography is a safe method to measure the ONSD for rapid diagnosis of increased ICP in children (Wiegand and Richards 2007).

2.2.10 Pupillometry

Preliminary studies have been performed on another noninvasive ICP measurement. Quantitative pupillometers can measure subtle changes/constriction in the pupillary light response. Meeker et al (2005) and Du et al (2005) described how pupillometers are more accurate than manual scoring, and have the ability to measure subtle pupillary constrictions that are too small to be seen using manual examination (Larson and Muhiudeen 1995, Rosenberg et al 2011).

2.2.11 Sensing tympanic membrane displacement

Marchbanks (1989) developed the tympanic membrane displacement (TMD) technique, which was the first proposed audiological method for assessing ICP noninvasively. The technique is based on measurements of TMD in response to elicitation of the acoustic reflex. It indirectly measures cochlear fluid pressure, which is a direct measure of ICP (Stettin et al 2011, Pranevicius et al 2012). TMD takes advantage of the communication between the CSF and the perilymph via the perilymphatic duct. Stimulation of the stapedial reflex causes a movement of the tympanic membrane, which is correlated to ICP (Raboel et al 2012). These pressure waves displace the tympanic membrane. Specific tympanic membrane displacement changes are indicative of high or low ICP (Gaihede et al 1995). Since the membrane is flexible, CSF and perilymph communicate through the cochlear aqueduct and elevated ICP is directly transmitted to the stapes footplate, changing its initial position and thereby affecting the direction and magnitude of displacement of the eardrum in response to the sound (Popovic et al 2009).

2.2.12 Analyzing otoacoustic emissions (OAE)/acoustic measure

Otoacoustic acoustic emissions (OAEs) were first recorded by Kemp (1978). They are sounds generated by the inner ear in response to a loud sound, and can be evoked by several techniques (Popovic et al 2009, Bruce 2014). The sounds are transmitted to the stapes, then further to the tympanic membrane through the ossicles. Avan et al (1996), Voss et al (2006), Olzowy et al (2008), and Bruce (2014) reported that distortion-product OAEs change with ICP. The characteristics of the OAE response vary with ICP, and can therefore be used as a relative indicator of ICP. Similarly to TMD, changes in OAE require a patent cochlear aqueduct and demonstrate significant patient variability; OAEs are not related to additional middle-ear reflex arc components such as the brainstem however, required for TMD measurements.

2.2.13 Transcranial acoustic (TCA) signals

Levinsky et al (2016) proposed a novel method for non-invasive ICP estimation based on transcranial acoustic (TCA) signals mixed with head-generated sounds estimate the static and pulsatile invasive ICP (iICP) through an ear probe placed in the right outer ear channel. They observed total 39 patients and realized 5789 predictions for static iICP and 6791 for pulsatile iICP respectively. Their validation showed a good agreement between iICP/nICP observations, with mean difference of 0.39 mmHg for static ICP and 0.53 mmHg for pulsatile ICP.

2.2.14 Visual-evoked potentials

Visual-evoked potentials (VEP) accurately reflect visual pathway disturbances. York et al (1981, 1984) demonstrated a strong linear relationship between VEP N_2 wave increased latency and ICP elevations, with correlation coefficients of 0.8–0.9 and best predictive value of VEP for ICP measurements of ≥300 mmH_2O. Zhao et al (2005) found a similar correlation between N_2 wave latencies and ICP in response to mannitol administration, obtaining a 0.97 correlation coefficient based on a larger study of 152 patients with mixed intracranial pathologies. These study results may not be representative however, since they do not consider patients with hypophyseal tumors, oxygen saturation less than 95%, liver dysfunction, uremia, severe acidosis, and diseases affecting visual acuity. In addition, VEP is not suitable for many specific patients, such as with frontal hematomas, retinal injuries, or optic nerve pathologies.

2.2.15 Electroencephalography

A method patented by Rosenfeld (1986) is based on electroencephalographic visual-evoked potentials (VEP) and uses a few occipital EEG electrodes to record electrical brain activity. Wu et al (2007) improved and investigated the relationship between ICP and the third positive-going wave of VEP recorded with high-density electrode arrays. The accuracy of EEG-derived ICP levels is difficult to estimate rigorously because the above assessment is only semiquantitative; further, there are large interindividual variabilities of latencies of VEP components, making it

difficult to discern between physiological long latencies and pathological delays caused by moderate increases in ICP (Popovic et al 2009).

Continuous ICP monitoring from the EEG is theoretically possible, but difficult to achieve practically. EEG can be recorded continuously at most for 8−12 h before the conductive gel on the electrodes dries up and the electrodes need to be replaced. In addition, continuous visual stimulation would certainly be fatiguing for conscious subjects (Popovic et al 2009).

2.2.16 Skull vibrations

The cranium can move in relation to the dura mater, which is deformed as the ICP fluctuates. Mick (1992) disclosed a method for noninvasively measuring changes in ICP by measuring changes in the natural frequency of the skull bone and its response spectrum. Changes in the natural frequency and its skull response spectrum are measured using a mechanically forced oscillation stimulus. A mechanical wave is created to transmit through the bone, and then to sense the frequency response spectrum. ICP trends and changes are shown by comparing spectral response data over time (Yue and Wang 2009). Variation in ICP alters the stress level experienced by the skull bone (Mick 1991, Sinha et al 2000). An ICP produces an initial stress field in the skull, leading to a stress-related term describing skull stiffness. Head vibrational responses are related to the stiffness of the skull (Li and Luo 2010).

2.2.17 Brain tissue resonance

The heart beat radiates through the organs and tissues and imparts a characteristic vibration and resonant response to the soft tissue and fluid of the brain. Tissue resonance analysis allows for characterization of physiological characteristics of various organs. Michaeli et al (2002) developed a new portable and computerized device based on tissue resonance analysis (TRA) technology for noninvasive ICP monitoring and measurement. ICP is dependent on the brain tissue mechanical resonance level value (Maloney-Wilensky et al 2009). Results using the method by Michaeli et al (2002) and the traditional method for blinded tests in 40 patients with

different diseases, with various ICP values over the range 1–66 mmHg, were highly correlated (r = 0.99), proving that TRA allows for accurate noninvasive ICP recordings. The method and device for noninvasive ICP measurement based on tissue resonance analysis have both qualitative and quantitative options. The qualitative method determines a specific ICP range: (either 10–20 mmHg, 20–40 mmHg, or >40 mmHg) based on long-term recording of ICP wave patterns. The quantitative method yields an ICP result in mmHg. Combining the transit times with measured acoustic impedance, resonant frequency, or ultrasound wave through the brain parenchyma tissue have been proposed.

2.2.18 Jugular vein

Jugular vein occlusion is known to increase ICP. Allocca (1980) described occluding the jugular vein for a short period of time (c. 5 s) and noninvasively measuring blood flow in the occluded jugular vein upstream change rate with a Hall sensor or an ultrasound transducer. There exists a linear relationship between jugular blood flow change rate and ICP (Verwei et al 2001). The jugular vein method is simple and can easily be made portable and field-deployable.

CHARPTER 3: WIRELESS ICP MEASUREMENT

This chapter 3 is partly taken from:

Xuan Zhang, Joshua E. Medow, Bermans J. Iskandar, Fa Wang, Mehdi Shokoueinejad, Joyce Koueik, and John G. Webster. Invasive and noninvasive means of measuring intracranial pressure: A review May.2017 Physiol. Meas.

Fa Wang,, Xuan Zhang, Mehdi Shokoueinejad, John G. Webster, Bermans J. Iskandar, Joshua E. Medow. A novel intracranial pressure read out circuit for passive wireless LC sensor. Revision. Feb 2017 IEEE Trans. Instrum. Meas.

Fa Wang,, Xuan Zhang, Mehdi Shokoueinejad, John G. Webster, Bermans J. Iskandar, Joshua E. Medow. Implantable passive intracranial pressure sensor modelling and spiral planar coil parameter design.. Revision. Jan 2017 IEEE Sensors J.

3.1 Implantable sensor

In the early 1990s, microsensor devices that read ICP when placed within the brain parenchyma were developed based on either fiberoptics (Camino) or electrical impedance (Codman 'Microsensor', Spiegelberg pressure sensor). These devices provide readings comparable to intraventricular catheters, are minimally invasive, and have minimal baseline drift if placed for a few days. They have become the standard method for measuring ICP accurately by neurosurgical teams worldwide (Luerssen 1997). Advances in monitoring technology and new microsensor tips have improved the ease, safety, and ICP measurement accuracy, allowing more widespread use in emergency and elective situations (Wiegand and Richards 2007).

3.1.1 Epidural and subdural

Epidural pressure sensors are small tongue-shaped sensors that fit into a cavity between the dura and the skull and in which the pressure-sensor diaphragm faces the dura and the brain. Subdural pressure sensors fit under the dura and the pressure sensor faces the brain.

Even though epidural and subdural pressure sensors have the disadvantage of not allowing therapeutic CSF drainage, they carry a lower rate of infection, hemorrhage, and seizures compared to the EVD (Gaab et al. 1989, Raabe et al. 1998). A specific advantage of epidural probes is the avoidance of dural penetration and the hazard of CSF leak and infection. However, the relationship between ICP and extradural space pressure is unclear.

Epidural devices currently do not provide the necessary accuracy for routine/clinical use. Bruder et al. (1995) showed that an epidural Camino sensor considerably overestimated ICP with a mean of about 9 mmHg, extending to almost 30 mmHg. Eide et al. (2008) described a significantly different mean ICP of 10.8 ±2.3 mmHg however, with comparable parameters such as mean wave amplitude of 3.4 ±1.0 mmHg and wave rise time of 0.27 ±0.02 s as related to ICP.

Epidural devices have been virtually abandoned because they are bulky and their insertion requires a large skull opening. One reusable device named Gaeltec ICP/B solid-state miniature ICP sensor was designed for use in the epidural space with zero reference-checking ability *in vivo*. However, measurement artifacts and measurement quality decay caused by repeated use were the limiting factors for this technology (Morgalla et al. 1997).

Subdural catheters are inserted almost exclusively following craniotomy because they require a much bigger dural opening than a burr hole allows. They are arguably less reliable in measuring elevated ICP (Bhatia and Gupta 2007,Wiegand and Richards 2007).

3.1.2 Intraparenchymal sensor

Intraparenchymal systems are inserted through a support bolt or are tunneled subcutaneously from a burr hole. Intraparenchymal devices are easy to place, have very few infectious complications, and are simple to handle, meaning they are the most reliable devices in daily practice. Mechanical complications can be due to placement problems or later problems during the monitoring period. Intraparenchymal probes are the most widely used devices to meaure ICP.

They are usually placed in the right frontal region at depths of approximately 2 cm. However, the placement can be modified depending on clinical needs or anatomical variations (Popovic et al. 2009). This type of device is the current choice in the emergency room and for elective surgical cases.

Camino and the Codman MicroSensor are the current two market leaders using the intraparenchymal technique. Both companies place a thin disposable wire through a twist drill hole into the cranial cavity. Considering the accuracy, most clinicians end the tip in the brain parenchyma, ideally 1–2 cm into the brain tissue.

The Camino Innerspace device is based on fiberoptic technology, so the wire needs to be kept in a straight line without kinking. Pressure change results in an alteration of the reflection of the light beam. A bolt for passing the wire is an essential part of the package (Gelabert-Gonzalez et al. 2006).

The Codman MicroSensor device has a micro-miniature strain gauge pressure sensor—pressure change results in a change of resistance—and can be inserted without a bolt. Wiegand and Richards (2007) state that ICP trace shifting used to be a problem for first-generation devices; however, it is not a significant problem in current models (Pople et al. 1995, Rossi et al. 1998, Anderson et al. 2004).

Intraparenchymal probes are a good alternative to ventricular catheters and usually have a low infection rate (Mack et al. 2003). The main disadvantage of this technique is a small drift of the zero line and the inability to drain CSF. This device is zeroed with respect to the atmosphere before insertion (Luerssen 1997, Gelabert-Gonzalez et al. 2006). The output is significantly dependent on the sensor zero drift, but both systems are only zeroed relative to atmospheric pressure before insertion instead of using *in vivo* calibration. Technical complications such as kinking of the cable for the Camino device and dislocation of the sensor for first-generation

Codman devices have also been reported (Stende et al. 2003). Furthermore, the local pressure value detected by the device may be misleading since the ICP is not uniform within the skull. In other words, supratentorial measurements may not reflect ICP as well as other methods such as intraventricular catheters. Wiegand and Richards (2007) described how direct intraparenchymal ICP monitoring based on various devices on the market is technically straightforward, accurate, and carries a low risk. It has become routine in pediatric neurosurgery.

Hummingbird Neuromonitoring products manage patients with conditions causing elevated ICP. Berlin et al. (2015) compared the ventricular and parenchymal ICP readings from a multi-parametric neurological Hummingbird® Synergy Ventricular System.

This system indicated that congruence from a total of 2259 observations is within ±0–3 mmHg of 93% of readings between ventricular ICP and parenchymal ICP. Following prescribed interventions, 98% of readings became congruent (within ±0–3 mmHg). The mean difference between the two methods was −0.95 mmHg and all mean ICP readings were between −2 and +2 mmHg. The results recommend use of the parenchymal ICP component for routine ICP monitoring, also permitting the ventricular catheter to drain cerebrospinal fluid (CSF).

An external ventricular drain (EVD) instead of an intraparenchymal fiberoptic monitor (IPM) may be better at controlling refractory intracranial hypertension. Liu et al. (2015) monitored and treated 122 patients with traumatic brain injury (TBI) of age ≥13 years in neurosurgical intensive care units between January 2009 and December 2012. For randomly monitoring either EVD or intraparenchymal fiberoptic enrolled patients, there was no significant difference between the groups in device-related complications ($p = 0.448$). Refractory intracranial hypertension was diagnosed in 44 of 122 patients, and the IPM group had a higher percentage of refractory intracranial hypertension compared to the EVD group (51.7% v. 21.0%, $p < 0.001$). The 1-month survival rate was 76.7% in the IPM group and 90.3% in the EVD group. In addition, the EVD group had a significantly higher 6-month post-injury survival rate compared to the IPM group

(88.7% v. 68.3%). Based on these findings, Liu et al. (2015) recommend routine placement of an EVD in patients with TBI, unless only parenchymal-type monitoring is available. Further, well-designed, multicenter studies, instead of a single-institution study, are needed to confirm these results as well as consider individual variability.

3.1.3 Problems of current passive LC ICP sensor

The passive *LC* pressure sensor for intraocular pressure (IOP) monitoring has matured since it was first proposed (Collins et al 1967). However, when applying this approach to the field of ICP measurement, the distance between the implanted sensor and the external reader is much larger as required by physiological factors, when compared to IOP measurement. In ICP monitor practice, achieving large enough measurement distance (larger than skull thickness) was a challenge, because of the poor coupling factor at that long distance. Nopper et al (2010)proposed a ICP sensor that could achieve a measurement distance of 8.5 mm. Coosemans et al (2004) proposed a similar approach for IOP measurement with a maximum distance of 7.5 mm, however, male adult scalp thickness ranges from 2 to 3.5 mm (Hori et al 1972)**,** and skull thickness average ranges from 6.08 mm to 8.09 mm, and differs at locations(Law 1993)**.** The signal strength received by the external reader is constrained first by electromagnetic (EM) wave absorption in the scalp and skull, second by limited transmitting power for biosafety, and third by limited sensor size for biocompatibility. Previous studies listed sensor parameter numbers directly(Nopper et al 2010, Coosemans et al 2004, Marioli et al 2005, Kaiser 2006). In addition, their principle analysis was based on a simple series resonant tank circuit and their designs did not fully consider all the parameters impacting the signal strength, such as: parasitic capacitance, skin effect on the parasitic resistance and substrate resistance. To enhance the signal strength, an accurate circuit model and improved sensor pattern are desirable.

3.2 Telemetry

To realize longer-term usability, the Microsensors such as Codman ICP sensor must be fully implanted within the patient, contain its own power source, and have wireless communication to the outside reader. A few non-commercialized attempts have so far been made to create such a system, most of them using inductive coupling to an external antenna and various active elements in the design that would influence incoming power and outgoing signal. Such miniaturized devices would also be useful in monitoring various other pressures in the body, and commercial efforts have used microelectromechanical systems (MEMs) type devices particularly for cardiac and ocular applications. Implantable catheter-tip sensor ICP devices have been connected to a telemetry unit. Miyake et al. (1997) described telemetric monitors used for long-term ICP monitoring in hydrocephalus patients. The telemetric technique is another invasive method with minimal infection risk, inpatient treatment time reduction, and inpatient setting monitoring. Further, the telemetric catheter can be implanted for up to 3 months, which significantly increases the monitoring duration. However, telemetric pressure sensors are not presently in wide use because the technology is not yet reliable and readily available. And even if an implantable sensor were to become technically feasible, the sensor would require multiple procedures for recalibration or surgical replacement to achieve zero drift stability.

3.2.1 Current telemetry

Welschehold et al. (2012) presented a system consisting of an implantable Neurovent-P-tel telemetric ICP probe, a reading device, and PC software for storing and analyzing data manufactured by Raumedic AG, Helmbrechts, Germany. The implanted telemetry ICP probe of 25 mm length and 1.76 mm thickness consists of an intraparenchymal pressure sensor at the end of the tip, as well as a subgaleal sensor with 31.5 mm diameter width and 4.3 mm thickness.

Kawoos et al. (2005) proposed a fully implantable MEMs-based ICP sensor, and a portable monitor to read out the sensor's data. This sensor is cylindrical, 10 mm in diameter and 8.85 mm

in height. The sensor is packaged within a titanium cylinder which is MRI compatible. The wireless communication method is based on bluetooth at 2.4 GHz frequency.

Yoon et al. (2004) reported a microtelemetry pressure sensor for CSF shunt systems. This sensor is based on an *LC* (where *L* represents an inductor and *C* a capacitor) tank circuit, and pressure to the resonant frequency conversion is measured by a network analyzer (HP 8510C). The total size of the sensor is 8.05×7.8 mm. The phase shift decreases from –33 to –42° linearly when pressure increases from 0 to 110 mmHg.

Kawoos et al. (2014) developed an implantable device for telemetric measuring of ICP over the long term in an animal model of blast-induced brain injury. They presented an analog implant for long-term ICP dynamics study after brain injuries of different origin. When measuring over the range 0–50 mmHg in steps of 5 mmHg, the pressure values shifted by 2.1 ±0.33 mmHg under the premise that the devices were calibrated *in vitro* over a range of 0–50 mmHg with maximum estimated error of 4.86% in the ICP measurements. The results showed that an immediate elevation of ICP within the first 1–3 h and a more gradual elevation occurred two days after the blast. In addition, after implanting in animals they also reported that the digital device requires a longer stabilization period than the analog version.

Chen et al. (2014) reported a wireless, real-time ICP monitoring system with passive, flexible, millimeter-scale sensors as small as 1×1×0.1 mm. This miniature novel sensor overcomes the traditional operating frequency limits and exhibits insensitivity to lossy tissue environments. They tested real-time continuous wireless monitoring of rat ICP *in vivo*. The tiny sensor structure is a distributed resonant tank, formed by stacking a deformable dielectric layer (microstructured styrene-butadiene-styrene (SBS) elastomer) between the two inductive spirals on flexible polyimide substrates in a sandwich structure. Pressure reduces the separation distance between the spiral layers, increases the effective coupling capacitance, and shifts the resonant frequency to lower frequencies. SBS has low loss in the high-frequency range compared to poly(dimethyl

siloxane) (PDMS) or polyurethane. However, drift in capacitance values is one drawback of SBS during cycling measurements.

Lilja et al. (2014) tested 21 patients in a Danish neurosurgical center clinic with an implanted Raumedic® telemetric ICP probe (NEUROVENT®-P-tel). They recorded diagnosis, implantation indication, surgical complications, ICP reading duration, number of ICP recording sessions related to symptoms of elevated ICP, and their corresponding clinical consequence. The 21 patients included 11 females and 10 males with a median age of 28 (2–83) years and median duration of disease of 11 (0–30) years. A total of 11 patients had various kinds of hydrocephalus, 7 patients had IIH, and 3 patients had normal pressure hydrocephalus. The median duration of implantation was 248 (49–666) days and median duration from implantation to last recording session was 154 (8–433) days. The results showed that 86 recording sessions included 29 surgical shunt revisions, 30 acetazolamide dose changing or programmable valve settings, 20 no action, and 5 new recording sessions. This supported the manuscript conclusion that telemetric ICP monitoring is useful in complicated CSF dynamic disturbance patients, who would otherwise require repeated invasive pressure monitoring.

Data on the accuracy of the Neurovent-P-tel telemetric monitoring device within a broad ICP range are missing. Freimann et al. (2013) applied a porcine model for a large ICP study. They tested a total of 34 comparative ICP measurements within an ICP range from 2 to 31 mmHg. A total of 34 comparative ICP measurements within an ICP range from 3 to 31 mmHg were performed. The mean difference between the telemetric ICP sensor and direct measurement from a water column within a riser tube was 0.4 mmHg; the limits of agreement were from –2.4 to 3.1 mmHg. This experiment showed that the telemetric Neurovent-P-tel sensor system afforded acceptable accuracy over a limited pressure range exceeding normal ICP values.

Guild et al. (2015) examined intracranial pressure in conscious rats via telemetry, in order to verify the long-term stability and viability of this technology in freely moving rats. They found

that the signals were stable throughout the 1 month period with an average ICP value of 6 ±0.8 mmHg.

Stehlin et al. (2015) proposed a prototype of an implantable ICP monitoring device, and investigated the potential patient risk related to interactions between the device and an MR scanner. The silicon-based piezoresistive sensor catheter had a drift of less than 2 mmHg over a 100-day period, which was not acceptable for long-term monitoring over the course of many years. It too is implanted inside the skull *c.* 20 mm into the brain parenchyma with wires that pass through a catheter to electronic components outside the skull but beneath the skin. The current prototype device was encapsulated in a silicone jacket and transmitted telemetric data via radio frequency (RF). The electronic unit consisted of a 2.4 GHz wireless data antenna link, an inductive coil for transcutaneous energy transfer, a rechargeable lithium ion battery, and a related circuit for signal conditioning and amplification. MRI interactions of the prototype implantable pressure sensing device towards minimizing heating risk and demonstrated a low safety risk below standard daily activity safety risk levels for the patient under expected clinical conditions and device configurations for the ICP device. However, artifacts from the device have the potential to adversely interfere with image quality.

Kang et al. (2016) proposed bioresorbable multifunctional silicon-based electronic sensors for measuring ICP as well as temperature, acceleration, etc. The construction consisted of a 30 μm poly(lactic-co-glycolic) acid (PLGA) membrane, a nanoporous silicon (60–80 μm thick; 71% porosity) or magnesium foil (60–80 μm thick), a serpentine geometry silicon nano–membrane, and an overcoat of silicon oxide (SiO_2, *c.* 100 nm thick). Both encapsulation material and its thickness controls the operational lifetimes of bioresorbable sensor, tested *in vivo* in rats. The implantable near-field communication (NFC) wireless system was constructed largely of bioresorbable materials. The NFC wireless system within the scalp subgaleal layer was connected to the bioresorbable sensor in the cranial vault via bioresorbable wires. Micro-patterned

magnesium coils in the NFC system transferred power and transmitted data by inductive coupling to an external reader. The measurement performance of this resorbable device compared favorably with that of nonresorbable devices.

Yang et al. (2015) described a biocompatibility evaluation of a thermoplastic rubber Arbomatrix™ (based on polyisobutylene) for wireless telemetric ICP sensor coating. They found similar cellular distribution in the brain–implant boundary and surrounding via a 60-day implant rat model for both Arbomatrix™ and biocompatible commercial silicone rubber shunt tubing. They concluded that Arbomatrix™ is well tolerated and may be an excellent protective coating for a new telemetric ICP monitoring chip.

Poupko et al. (2012) introduced a noninvasive intracranial pressure (nICP) monitor by tracking the change of electrical impedance across the head, which would be helpful to estimate the intracranial pressure and additional cerebral parameters under certain circumstances.

Kiefer et al. (2012) reported that long-term telemetric ICP measuring devices Neurovent P-Tel and S-Tel, could provide reliable dynamic measurements over an 18-month period.

Antes et al. (2014) reported on long-term telemetric ICP measurement device complications. A total of 185 telemetric ICP catheters were implanted between April 2010 and February 2013 for diagnostic purposes. One brain abscess (0.5%) and two cutaneous infections (1.1%) occurred, both with *Staphylococcus*. Six patients experienced single new-onset seizures (3.2%) and one patient (0.5%) had a temporary hemiparesis. A total of 15.6% of patients had intracerebral hemorrhages, most of which were small punctate. Almost half (46.9%) of the patients had focal edematous reactions surrounding the inserted telemetric sensor.

Wireless telemetry with a biocompatible sensor reduces the risk of infection and other complications related to external wires. A physician can receive the pressure readings for early detection of shunt malfunction and help patients avoid unnecessary shunt revisions (Zhang 2014).

3.2.2 Problem of current telemetry

Some studies (Nopper et al 2010, Coosemans et al 2010, Butler et al 2002)developed similar telemetry devices based on traditional grid dip oscillator technology. But grid dip oscillator technology has some constraints which prevent it from being applied to ultrasmall sensors, which always resonate at GHz frequencies: First, its sweeping frequency range is limited by the tuner capacitor, thus the frequency range is usually around 20 MHz (10 MHz to 30 MHz in (Nopper et al 2010); 22–41 MH (Coosemans et al 2010); 12.76 and 13.01 MHz in (Butler et al 2002)), which is narrow. Second, the center and highest frequency of the oscillator is limited by the oscillator's parasitic capacitance, which won't reach up to the GHz range. Third, the oscillator's resonant frequency is determined by the imaginary portion of the system, including the antenna and the sensor. Especially when the sweeping frequency approaches the sensor resonant frequency, the capacitance components of the sensor influence the oscillator's resonant frequency to form a "frequency drift". This phenomenon inhibits us from getting accurate measurement results when trying to detect the tiny pressure change on the sensor. Also, this is an analog circuit with limited frequency resolution. Our reader overcomes these constraints. Its output frequency ranges from 35 MHz to 2.7 GHz, with a minimal 0.5 kHz resolution. In addition, the output frequency is only determined by the microcontroller's commands, and is isolated from the antenna and sensor.

Measurement distance is also a challenge and a significant consideration for ICP monitor design. Nopper et al. proposed a reader that could achieve a measurement distance of 8.5 mm (Nopper et al 2010). Coosemans et al. proposed a similar reader for intraocular pressure measurement with maximum distance of 7.5 mm. In real practice, the male adult scalp thickness ranges from 2 to 3.5 mm (Hori et al 1972), and skull thickness average ranges from 6.08 mm to 8.09 mm, differs with location, and standard deviations range from 1.15 to 1.88 mm (Law 1993). The dura is a thick

membrane surrounding the brain, which has an average thickness of 0.27 mm (Reina et al 1996). So the minimal measurement distance should be at least 10 mm and desirably larger than 15 mm.

CHAPRTER 4: PASSIVE SENSOR DESIGN

This chapter 4 is partly taken from:

Fa Wang,, Xuan Zhang, Mehdi Shokoueinejad, John G. Webster, Bermans J. Iskandar, Joshua E. Medow. Implantable passive intracranial pressure sensor modelling and spiral planar coil parameter design.. Revision. Jan 2017 IEEE Sensors J.

4.1 Principle

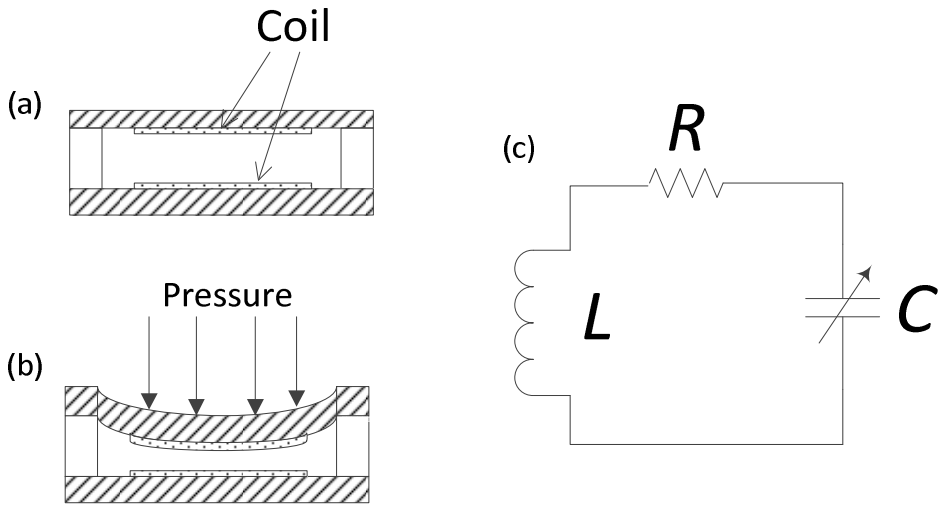

Fig. 4-1. The passive sensor model. (a) Two double layer spiral planar coils face each other, creating a resonant tank. (b) When pressure is applied on the top membrane, the two coils move closer to each other. (c) Equivalent circuit model of system, where *R* is parasitic resistance of planar coils, *L* is the coil inductance, and *C* is the variable capacitance between the coils which is dependent on the pressure.

The basic idea behind the passive biosensor is based on a resonant tank circuit. Two spiral planar coils are placed facing each other, creating a capacitor, as shown in (1) and Fig. 4-1.a. *A* is the area of overlap of the two parallel plates, ϵ_r is the dielectric constant of the material between the plates, ϵ_0 is the electric constant ($\epsilon_0 \approx 8.854\times10^{-12}$ F·m^{-1}), and *d* is the separation distance between the

plates. When pressure increases, the two coils move closer, as shown in Fig. 4-1.b, the separation distance between two coils *d* decreases, the capacitance *C* of the system increases, which reduces the resonant frequency *f* of the tank circuit as shown in Fig. 4-1.c (2). Therefore, pressure applied on the sensor can be detected by measuring the resonant frequency of the tank.

$$C = \epsilon_{\mathrm{r}}\epsilon_0 \frac{A}{d} \tag{1}$$

$$f = \frac{1}{2\pi\sqrt{LC}} \tag{2}$$

Tiny dimensions and pattern of spiral planar microcoils are desirable for implantation into the brain. In order to fabricate ultra-small sensors on a silicon substrate, Microelectromechanical Systems (MEMS) technology can be employed.

A reader with an antenna outside the brain measures the ICP changes remotely. When the antenna is coupled with the sensor in its near field, the reader measures the antenna-sensor system's phase. At the resonant frequency of the sensor, the phase of the system has notable changes, as shown in Fig. 4-2, and helps us to determine the current sensor's resonant frequency. In this paper, we define the amplitude of "shift drop" at the resonant frequency as the signal strength, which we want to optimize to make the sensor detection easier.

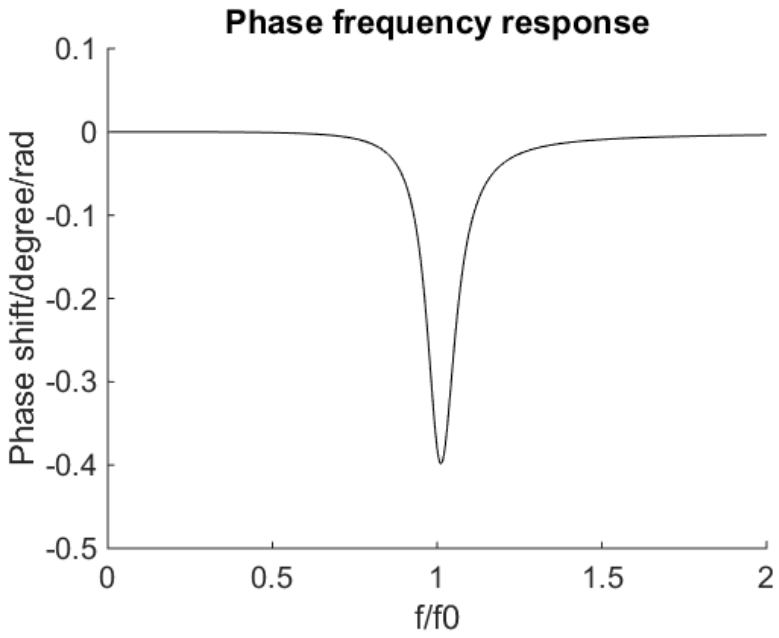

Fig. 4-2: Typical antenna-sensor system's impedance and phase change as a function of frequency.

Ideally, the antenna and sensor system could be modelled as Fig.4-3, without considering the substrate loss and parasitic capacitance. Most of previous studies were based on this ideal model. (Nopper et al 2010, Coosemans et al 2004, Marioli et al 2005, Kaiser 2006)

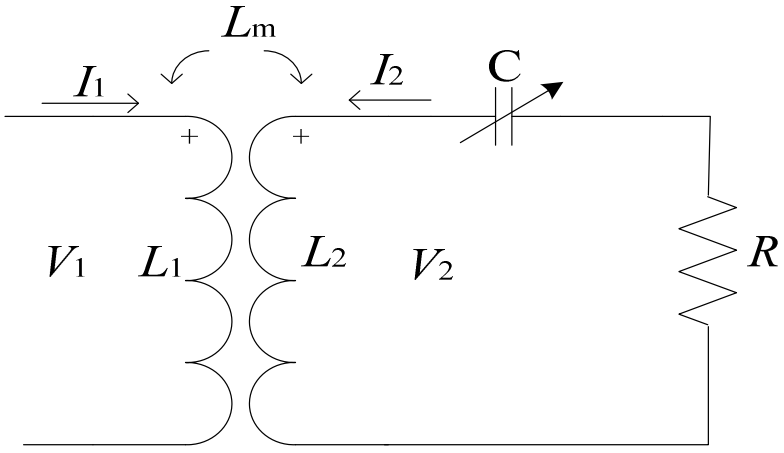

Fig. 4-3. Ideal antenna-sensor circuit model.

This paper develops a more accurate sensor circuit model in section II. Section III presents the approach to calculate better system parameters, such as antenna size, sensor size, resonant frequency, planar coil turns, and spacing width of each planar coil and determines the corresponding influence on the signal strength received by telemetry. This design suggestion is proved by the measurement result from fabricated PCB sensor. Section IV summarizes the sensor design progress. PCB sensor and MEMS sensor are designed based on this summary. Measurement result of the PCB sensor and simulation result of MEMS sensor are given,

4.2 Circuit model

4.2.1 Single layer spiral planar coil circuit model

Fig. 4-4 shows a typical spiral planar coil structure, which consists of the substrate and copper trace. The trace forms a coil L, and a series resistor R_s, which exists because the copper is not an ideal conductor. The adjacent trace forms a series capacitor, C_s, which is not desirable. Current flowing inside the copper may leak to the ground (space), R_{sub}, due to the substrate which is not an ideal insulator. The copper layer also forms a parallel capacitor C_{sub} to the ground for which C_{sub}'s dielectric layer is the substrate. Thus, Fig.5 shows equivalent circuit model, in which $C_p = 2C_{sub}$ and $R_p = \frac{1}{2}R_{sub}$. The value of these components is determined by the sensor's pattern and material properties. D is the diameter of sensor, W is the trace width, s is the spacing width, and β is the spacing to trace ratio s/W. n is the turns of the coil, l is the total trace length, b is the outer diameter/length of the coil, and b_{in} is the inner diameter. α is the inner diameter to outer diameter ratio b_{in}/b. t_{co} is the copper thickness and t_{sub} is the substrate thickness shown in Fig. 4-4 .

The geometry of Fig. 4-5 yields the following formulas (Jow et al 2007):c

$$2(1+\beta)Wn = (1-\alpha)D \tag{3}$$

$$\mathrm{l} = 4nD - 4nW - (2n+1)^2(1+\beta)W \tag{4}$$

If trace width and spacing are small enough when compared to the sensor side length (diameter), (4) could be simplified as:

$$\mathrm{l} = 2n(1+\alpha)D \tag{5}$$

Subtracting (4) from (5) yields the error of (5), which is $-4nW - (4n+1)s$

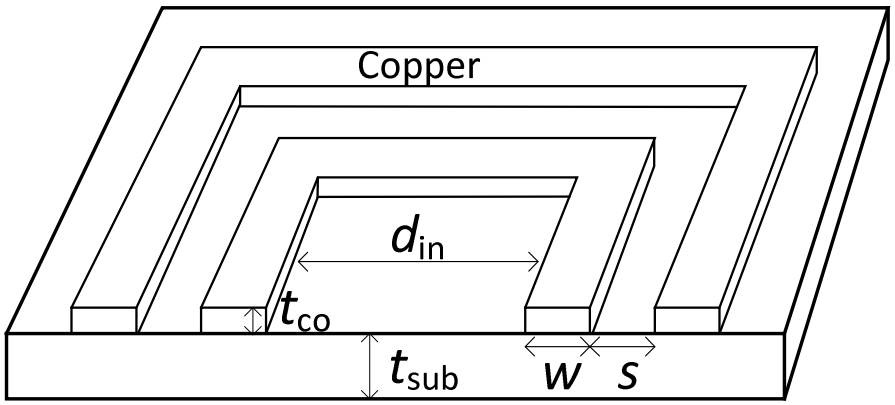

Fig. 4-4 Printed single layer of spiral planar coil and substrate

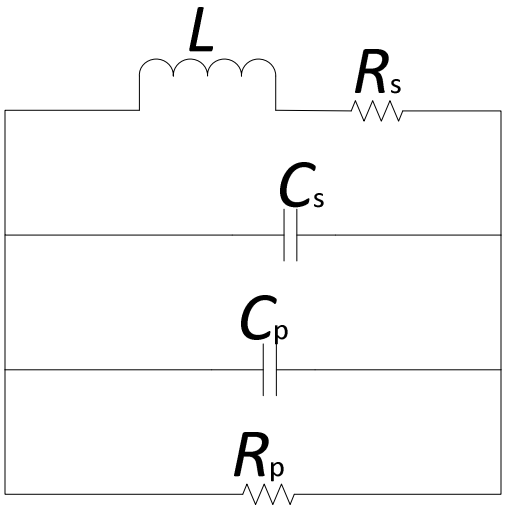

Fig.4-5 Equivalent circuit model for single layer spiral planar coil

4.2.2 Approximated value of components in the single layer spiral planar coil circuit model

4.2.2.1 Self-inductance *L*

The planar spiral coil's inductance has been well studied. Mohan et al (1999) suggested that, for the square shape spiral planar coil, the self-inductance is

$$L = \frac{2\mu}{\pi} n^2 d_{\text{avg}} \left(\ln\left(\frac{2.07}{\varphi}\right) + 0.18\varphi + 0.13\varphi^2 \right) \tag{6}$$

Where μ is the magnetic permeability of the metal (copper) traces, which is approximately equal to $\mu_0 = 4\pi \times 10^{-7}$. d_{avg} is the average diameter of the square, which is $\frac{D+D_{in}}{2} = \frac{1+\alpha}{2} D$, and $\varphi = \frac{1-\alpha}{1+\alpha}$. The accuracy degrades when $\varphi < 0.1$ or $n < 2$ (Jow et al 2007).

(6) is rewritten for future discussion which includes the symbols from section II.*A*:

$$L = \frac{\mu}{\pi} n^2 D(1+\alpha) \left(\ln\left(\frac{1+\alpha}{1-\alpha}\right) + 0.18\left(\frac{1-\alpha}{1+\alpha}\right) + 0.13\left(\frac{1-\alpha}{1+\alpha}\right)^2 + 0.726 \right) \tag{7}$$

4.2.2.2 Series resistance R_s

Considering the skin effect, the expression of series resistance along the copper trace is:

$$R_{\mathrm{s}} = \frac{\rho_{\mathrm{co}} l}{W\delta(1 - e^{-\frac{t}{\delta}})} \tag{8}$$

Where ρ_{co} is the resistivity of copper, which is $1.7 \times 10^{-8}\ \Omega/\mathrm{m}$, δ is the skin depth of the copper, which depends on the material property and frequency:

$$\delta = \sqrt{\frac{\rho_{co}}{\pi\mu f}} \tag{9}$$

4.2.2.3 Parallel resistance R_{p}

R_{p} could be expressed as:

$$R_{\mathrm{p}} = \frac{\rho_{\mathrm{sub}} t_{\mathrm{sub}}}{Wl} \tag{10}$$

R_{p} depends on the substrate material. When the sensor is fabricated on a printed circuit board (PCB), the substrate material is FR4 and ρ_{sub} (10^8 MΩ/cm) is large enough so R_{p} can be neglected. However, for silicon substrate sensors, R_{p} is in the kΩ range which should be taken into consideration.

4.2.2.4 Series capacitance C_{s}

C_{s} is the capacitance of the adjunct coplanar strip. Neagu et al (1997) roughly modeled C_{s} as two long parallel wires with diameter W:

$$C_{\mathrm{s}} = \frac{\pi\epsilon_o\epsilon_r(l - 4D)}{nln\left(1 + \beta + \sqrt{\beta^2 + 2\beta}\right)} \tag{11}$$

(11) is sufficient when series capacitance does not dominate the capacitance of the whole system. Gevorgian et al (2003) and Troedsson et al (2004) give a more accurate model, which consists of two parts of series capacitance, shown in Fig.4-6.

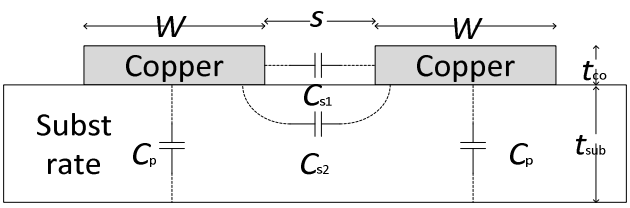

Fig. 4-6 Series capacitance consists of two parts: capacitance between two copper trace capacitance C_{s1}, and adjunct coplanar strip C_{s2}. Parallel capacitance from trace to substrate is also shown.

C_{s1} is the capacitance between the two sidewalls of the trace per unit length, which similar to the parallel plate capacitor, could be expressed as:

$$C_{\mathrm{s1unit}} = \epsilon_0 \frac{t_{\mathrm{co}}}{s} \tag{12}$$

C_{s2} is the capacitance of adjunct coplanar strip:

$$C_{\mathrm{s2unit}} = \epsilon_{\mathrm{o}} \epsilon_{\mathrm{eff}} \frac{K(k_0')}{K(k_0)} \tag{13}$$

Where ϵ_{eff}:

$$\epsilon_{\mathrm{eff}} = 1 + (\epsilon_{\mathrm{r}} - 1) \frac{K(k')K(k_0)}{2K(k)K(k_0')} \tag{14}$$

Where $\epsilon_{\mathrm{r}}$is the permittivity of the substrate. $K(k)$ is the complete elliptic integral of the first kind:

$$K(k) = \frac{\pi}{2} \sum_{n=0}^{\infty} \left[\frac{(2n-1)!!}{(2n)!!} \right]^2 k^{2n} \tag{15}$$

And $k_0, k, k',\ k_0'$ in (14) are defined as:

$$k = \frac{\tan h\left(\frac{\pi s}{4t_{\mathrm{sub}}}\right)}{\tan h\left(\frac{\pi(s+W)}{4t_{\mathrm{sub}}}\right)} \tag{16}$$

$$k_0 = \frac{s}{s + 2W} = \frac{\beta}{\beta + 2} \tag{17}$$

$$k' = \sqrt{1 - k^2} \tag{18}$$

$$k_0' = \sqrt{1 - k_0^2} \tag{19}$$

(12) and (13) give the unit length capacitance, which is multiplied by the total length of the trace. Troedsson et al (2004) suggested that total capacitance should be divided by a factor K_{series} due to the voltage drops along the trace, which are determined by the geometry and pattern of the plate. For commonly used geometries and patterns $K_{\text{series}} \approx n^2$. So if n is sufficiently large, C_s can be neglected.

The final expression of C_s is:

$$C_s = \left(\epsilon_0 \frac{t_{co}}{s} + \epsilon_0 \epsilon_{\text{eff}} \frac{K(k_0')}{K(k_0)} \right) * \frac{l}{K_{\text{series}}} \tag{20}$$

4.2.2.5 Parallel capacitance

The substrate capacitance to the ground could be expressed as:

$$C_p = \epsilon_0 \epsilon_r \frac{Wl}{t_{\text{sub}}} \tag{21}$$

(21) demonstrates C_p is determined by the copper cover area and substrate thickness. Troedsson et al (2004) suggested that C_p should be divided by a factor K_{parallel} due to the fringe capacitance. K_{parallel} is determined by β, and for a typical pattern, $K_{\text{parallel}} \approx 1.5$, and slightly decreases when β decreases:

$$C_{\mathrm{p}} = \epsilon_0 \epsilon_{\mathrm{r}} \frac{Wl}{t_{sub} K_{\mathrm{parallel}}} \tag{22}$$

4.2.3 Double layer spiral planar coils circuit model

Previous sections focused on the single planar layer circuit model of the sensor. We introduce the circuit model of the whole sensor which includes two planar spiral planar coil circuit models. The top plate and bottom plate face each other in the sensor. The sensor lumped circuit model is based on the single plate model:

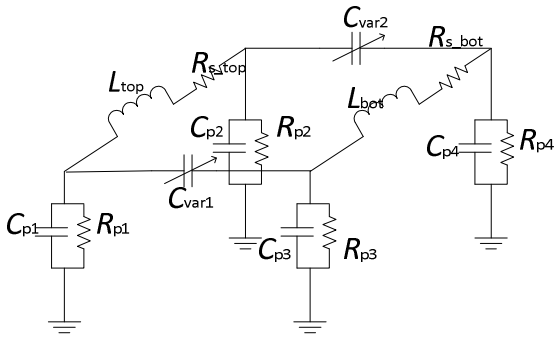

Fig. 4-7 Lumped circuit model for double layer spiral planar coils

C_{var} is the capacitance between two plates, which increases with pressure. If two plates have the same pattern, it is:

$$C_{\mathrm{var}} = \epsilon_0 \frac{Wl}{\mathrm{distance}} \tag{23}$$

L_{top} and L_{bot} have the same voltage in the electromagnetic field, which makes them parallel to each other. Fig. 7 is simplified as Fig. 4-8(a), and each component value is:

$$C_{\mathrm{p}} = C_{\mathrm{ptop}} + C_{\mathrm{pbot}} \tag{24}$$

$$C_{\mathrm{s}} = C_{\mathrm{stop}} + C_{\mathrm{sbot}} \tag{25}$$

$$R_{\mathrm{s}} = {}^{1}\Big/_{\frac{1}{R_{\mathrm{stop}}} + \frac{1}{R_{\mathrm{sbot}}}} \tag{26}$$

$$L_2 = \frac{L_{\mathrm{top}}L_{\mathrm{bot}} - M_{\mathrm{tb}}^2}{L_{\mathrm{top}} + L_{\mathrm{bot}} - 2M_{\mathrm{tb}}} \tag{27}$$

M_{tb} is the mutual inductance between top and bottom plates. If these two plates have the same pattern, and they are close enough to each other, then we can assume $L_{\mathrm{top}} \approx L_{\mathrm{bot}} \approx M_{\mathrm{tb}}$ which results in $L_2 \approx L_{\mathrm{top}}$.

If we use $C_{\mathrm{tot}} = C_{\mathrm{p}} + C_{\mathrm{s}} + C_{\mathrm{var}}$, a simpler equivalent circuit model results modeled in Fig.4-8(b).

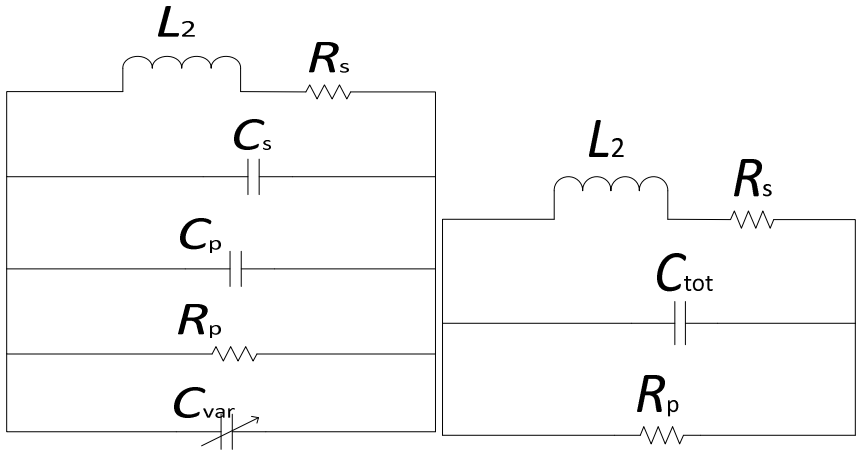

(a) **(b)**

Fig. 4-8 (a) Equivalent circuit model for double layer spiral planar ICP sensor (b) simplified circuit of model Fig. 9(a) in which $C_{\mathrm{tot}} = C_{\mathrm{p}} + C_{\mathrm{s}} + C_{\mathrm{var}}$

4.2.4 Reader's antenna and sensor coupling system

Fig. 4-9 shows a reader with an antenna is employed to measure the wireless sensor. Assuming the antenna's parasitic capacitance is $C_{antenna}$ and series resistance is R_{loss}, Fig. 4-10 shows the reader's antenna and sensor coupling system's equivalent circuit model could be built.

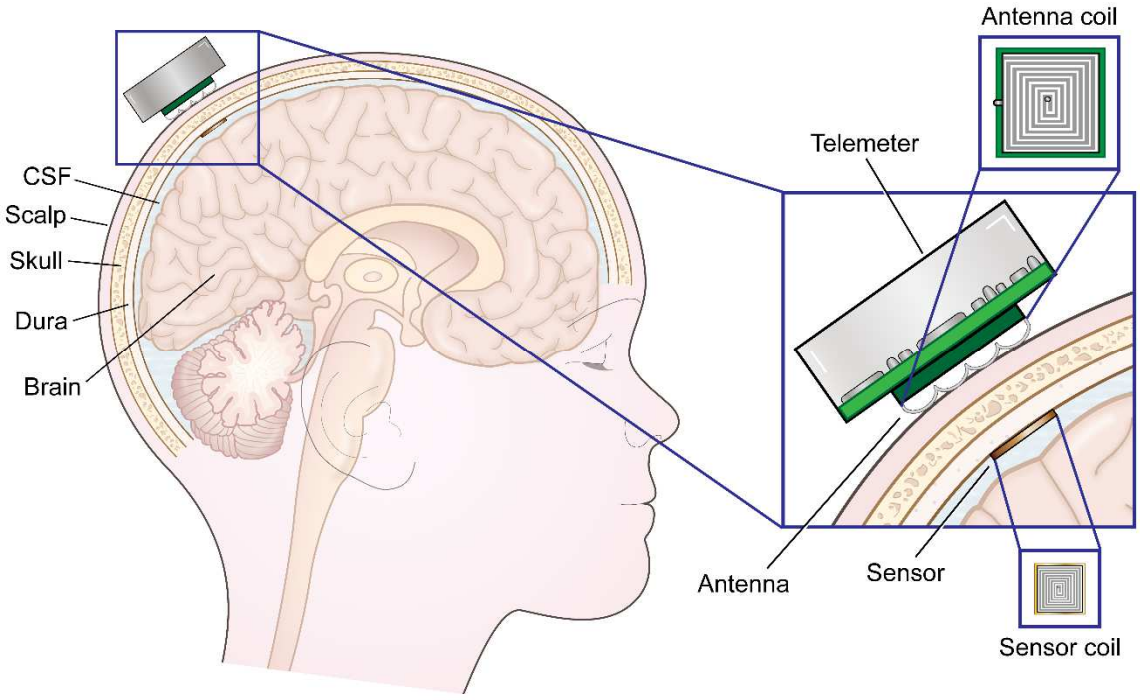

Fig. 4-9 Reader and sensor coupling system

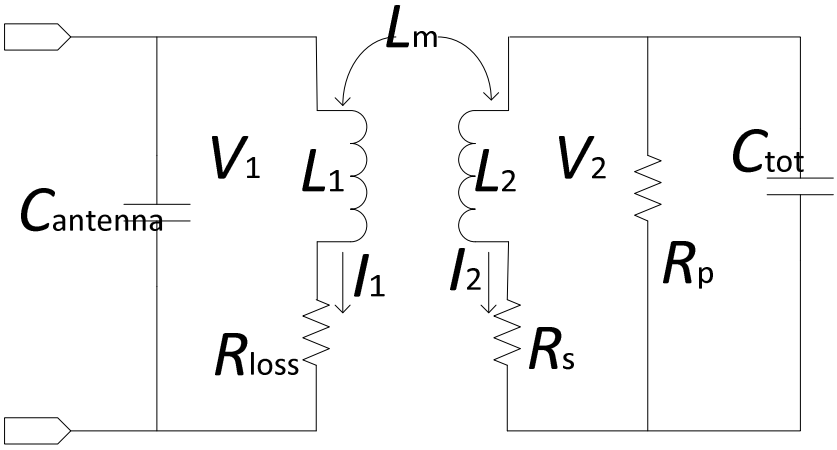

Fig.4-10 Reader and sensor coupling system equivalent circuit model

L_{m} is the mutual inductance between the telemeter's antenna and spiral planar mircocoil on the sensor. L_{m} is expressed as shown in the following equations (Raju et al 2014):

$$L_m = \left(\frac{4}{\pi}\right)^2 \sum_{i=1}^{i=n_a} \sum_{j=1}^{j=n_b} M_{\mathrm{ij}} \tag{28}$$

$$M_{ij} = \frac{\mu_0 \pi a_{\mathrm{i}}^2 b_{\mathrm{j}}^2}{2\left(a_i^2 + b_{\mathrm{j}}^2 + z^2\right)^{\frac{3}{2}}} \left(1 + \frac{15}{32}\gamma_{\mathrm{ij}}^2 + \frac{315}{1024}\gamma_{\mathrm{ij}}^4\right) \tag{29}$$

$$\gamma_{ij} = \frac{2a_i b\mathrm{j}}{a_{\mathrm{i}}^2 + b_{\mathrm{j}}^2 + z^2} \tag{30}$$

Where a_i is the i^{th} turn's antenna radius, and b_j is the j^{th} turn radius of spiral planar coil ICP sensor shown in Fig. 9. z is the distance between antenna and ICP sensor. If spacing and trace width of the ICP sensor is relatively small compared to the whole sensor diameter, b_j could be expressed as:

$$b_j = \frac{D}{2} - (n_j - 1)(1 + \beta)W \tag{31}$$

Based on Kirchhoff's law the following equations (32)(33)(34) are derived from Fig. 10:

$$V_1 = j\omega L_1 I_1 + j\omega L_{\mathrm{m}} I_2 \tag{32}$$

$$V_2 = j\omega L_2 I_2 + j\omega L_{\mathrm{m}} I_1 \tag{33}$$

$$V_2 = -R_{\mathrm{s}} I_2 - \frac{R_{\mathrm{P}}}{\mathrm{j}\omega C_{\mathrm{tot}} R_p + 1} * I_2 \tag{34}$$

The impedance seen from V_1 could be derived from (32)(33)(34)

$$Z_1 = \frac{V_1}{I_1} = j\omega L_1 - \frac{\omega^2 \mathrm{L_m}^2}{\square \omega L_2 + R_s + \frac{R_\mathrm{p}}{\mathrm{j}\omega C_\mathrm{tot} R_\mathrm{p} + 1}} \tag{35}$$

Fig. 2 shows at the resonant angular frequency ω_0 which is shown in (36), the reader could detect the maximum phase drop amplitude (PD), which is given in (37):

$$\omega_0 = \sqrt{\frac{1}{L_2 C_\mathrm{tot}} - \frac{1}{R_\mathrm{p}^2 C_\mathrm{tot}^2}} \tag{36}$$

$$\text{Amplitude} \triangleq \frac{\mathrm{Re}(Z1)_{\omega=\omega_0}}{\mathrm{Im}(Z1)_{\omega=\omega_0}} = \frac{\frac{\omega^2 \mathrm{L_m}^2}{R_s + \frac{R_\mathrm{p}}{1 + R_\mathrm{p}^2 \omega^2 C_\mathrm{tot}^2}}}{\omega \mathrm{L}_1} = \frac{\omega \mathrm{L_m}^2}{R_\mathrm{s} L_1 + \frac{R_\mathrm{p} L_1}{1 + R_\mathrm{p}^2 \omega^2 C_\mathrm{tot}^2}} \tag{37}$$

The amplitude of phase drop is a signal that can be measured by the reader. Section III focuses on (37) to discuss the ICP system's parameter optimization in order to get higher signal strength.

4.3 Parameter Optimization

4.3.1 Resonant frequency

Resonant frequency f_0, which is given by (36), should follow two major requirements: 1) f_0 should be within Industry Science and Medical (ISM) bands. ISM bands are radio bands reserved for the use of industrial, scientific and medical purposes. It is highly recommended to locate the f_0 in ISM bands to prevent potential interference with other telecommunication devices. 2) f_0 should be small enough compared to f_{SR}, the coil's self-resonant frequency, which is specified by (38). However f_0 should not be too small because it is positively correlated to the amplitude, as shown in (37).

$$f_\mathrm{SR} = \frac{1}{2\pi} \sqrt{\frac{1}{L_2(C_\mathrm{p} + C_\mathrm{s})} - \frac{1}{R_p^2 (C_\mathrm{p} + C_\mathrm{s})^2}} \tag{38}$$

For commonly used ICP sensors f_{SR} is from 5 GHz to 20 GHz.

Thus based on these facts, 902.000 MHz to 928.000 MHz and 2.400 GHz to 2.500 GHz bands may be the best choices for f_0.

(36), in which component values could be calculated by (6)(10)(20)(22)(23), could be employed to "predict" the resonant frequency to ensure that f_0 locates in our desired band. To verify the (36)'s accuracy, several PCB sensors, with different D, n, α, β were fabricated (as shown in Fig.4-11) and measured (as shown in Fig.4-12) by a vector network analyzer (VNA).

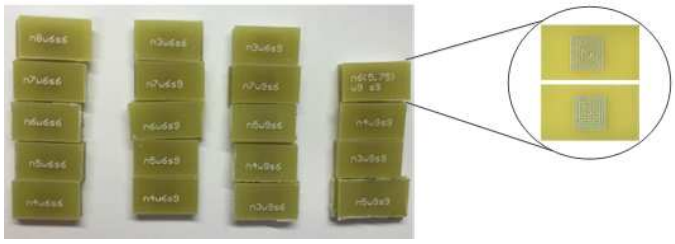

Fig. 4-11 PCB sensors fabricated

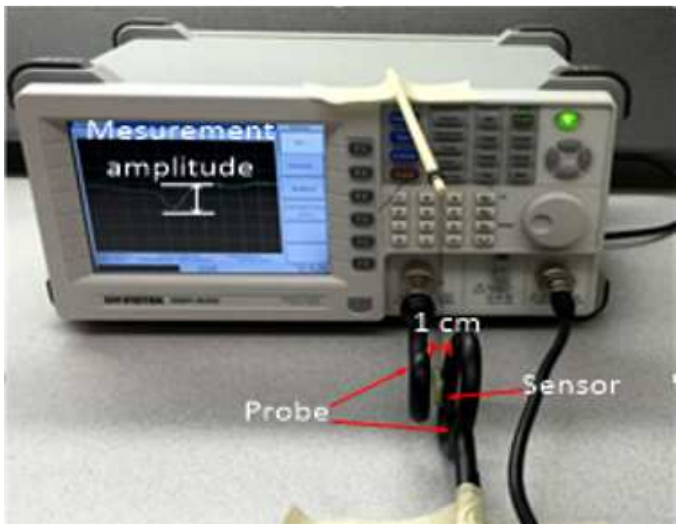

Fig. 4-12 PCB sensors measurement setup

For each pattern, we fabricated two identical sensors, and only kept the sensors which yielded similar results (resonant frequency and amplitude) as measured by the VNA. "Similar" here is

defined as the difference is less than 5%, and the final result is an average from two sensors. The measurement result was compared with (36), which is based on an improved model presented by our paper, and also compared with (2), which is based on the simple *LCR* model. Fig.4-13 shows our model predicts the resonant frequency precisely, with 3.95% error rate, compared to the *LCR* model's 11.97% error rate.

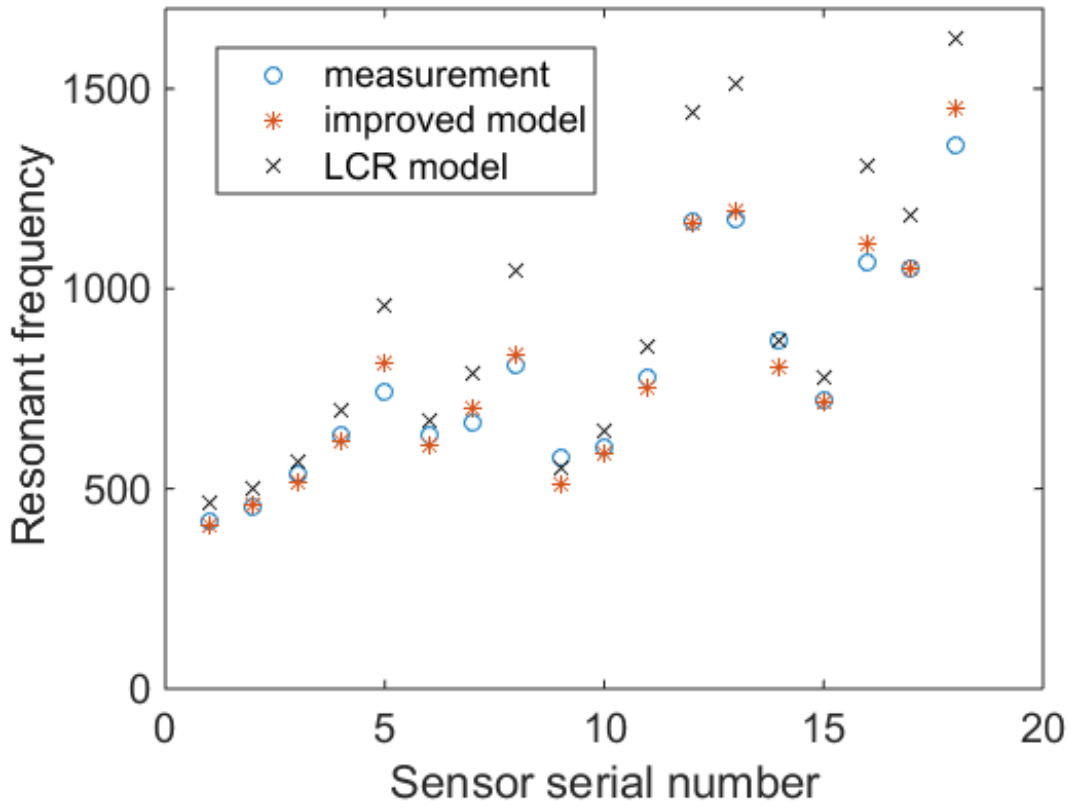

Fig.4-13 PCB sensor measurement f_0 compared to the predicted f_0 based on the improved model in this paper, and predicted f_0 based on the simple *LCR* model.

4.3.2 Sensor size

After summing terms of (28), we eliminated the influence of γ^2 and γ^4, and assuming b_j is much smaller than $a_i + z$, which simplifies $\frac{\mu_0 \pi a_i^2 b_j^2}{2\left(a_i^2+b_j^2+z^2\right)^{\frac{3}{2}}}\left(1+\frac{15}{32}\gamma_{ij}^2+\frac{315}{1024}\gamma_{ij}^4\right)$ to $\frac{\mu_0 \pi a_i^2 b_j^2}{2\left(a_i^2+z^2\right)^{\frac{3}{2}}}$:

$$L_m = \left(\frac{4}{\pi}\right)^2 \sum_{i=1}^{i=n_a} \frac{\mu_0 \pi a_i^2}{2(a_i^2+z^2)^{\frac{3}{2}}} \left(\left(\frac{(2n-1)(n-1)}{6}(1+\beta)^2 W^2 + \frac{\alpha D(n-1)(1+\beta)W}{2} + \frac{1}{4}\alpha^2 D^2\right) n\right) \tag{39}$$

(39) is derived based on the sum of an arithmetic progression's square, since $\sum_{j=1}^{j=n_b} b_j$ is an arithmetic series where the first item is αb and common difference is $(1+\beta)W$, and $b = \frac{1}{2}D$, respectively.

Treat the size of antenna a and distance z as constants, then (39) is:

$$L_m = K_{Lm}\left(\left(\frac{(2n-1)(n-1)}{6}(1+\beta)^2 W^2 + \frac{\alpha D(n-1)(1+\square)W}{2} + \frac{1}{4}\alpha^2 D^2\right) n\right) \tag{40}$$

Where

$$K_{Lm} = \left(\frac{4}{\pi}\right)^2 \sum_{i=1}^{i=n_a} \frac{\mu_0 \pi a_i^2}{2(a_i^2+z^2)^{\frac{3}{2}}} \tag{41}$$

Substitute (3),(5),(8),(10),(20),(22),(42) into (37) which yields:

Amplitude (42)

$$= \frac{\omega_0 {K_{\mathrm{Lm}}}^2 \left(\left(\frac{(2n-1)(n-1)}{24n^2}(1-\alpha)^2 D^2 + \frac{\alpha(1-\alpha)D^2(n-1)}{4n} + \frac{1}{4}\alpha^2 D^2 \right) n \right)^2}{L_1 \left(\frac{\rho_{co} n^2 (1+\alpha)(1+\beta)}{(1-\alpha)\delta(1-e^{-\frac{t}{\delta}})} + \frac{\frac{\rho_{\mathrm{sub}} t_{\mathrm{sub}}(1+\beta)}{(1+\alpha)(1-\alpha)D^2}}{1+\left(\frac{\rho_{\mathrm{sub}} t_{\mathrm{sub}}(1+\beta)}{(1+\alpha)(1-\alpha)D^2}\right)^2 \omega_0^2 C_{\mathrm{tot}}^2} \right)}$$

where

$$C_{\mathrm{tot}} = \epsilon_0 \epsilon_{\mathrm{r}} \frac{2(1+\alpha)(1-\alpha)D}{t_{\mathrm{sub}}(1+\beta)} + \frac{\pi \epsilon_{\mathrm{o}} \epsilon_{\mathrm{r}} (2n(1+\alpha)D - 4D)}{n ln\left(1+\beta+\sqrt{\beta^2+2\beta}\right)} + \epsilon_0 \frac{2(1+\alpha)(1-\alpha)D}{\mathrm{distance}(1+\beta)} \quad (43)$$

(42) has been simplified based on the assumption that the top plate and bottom plate's pattern are the same. From (42), we conclude signal strength amplitude increases with D^4, since the effect of D is negligible in the denominator of (42). Therefore we could fabricate the sensor as large as possible. Our measurement result also supports this idea, the signal strength of 5 mm diameter sensors is 0.1491 dB average and 0.0408 dB standard deviation, compared to 0.0566 dB average and 0.0141 deviation for 4 mm diameter sensor, and 0.0135 dB average and 0.0032 deviation for 3 mm diameter sensor. However, the sensor's diameter is limited by the largest holes that could be drilled through the skull.

4.3.3 Sensor coil turns n

In (42) and (43), R_{p} and C_{tot} are determined by the copper covered area, and are not sensitive to the number of turns. R_{s} increases with n^2, and L_{m} increases with n. $\frac{\omega_0^2 {L_{\mathrm{m}}}^2}{R_{\mathrm{s}} + \frac{R_{\mathrm{p}}}{1+R_{\mathrm{p}}^2 \omega_0^2 C_{\mathrm{tot}}^2}}$ plateaus when n is sufficiently large and the influence of R_{p} can be ignored. So the lower bound for n is given by

$$\frac{\rho_{\mathrm{co}}(1+\alpha)(1+\beta)}{2(1-\alpha)\delta(1-e^{-\frac{t}{\delta}})}n^2 \gg \frac{R_{\mathrm{p}}}{1+R_{\mathrm{p}}^2\omega_0^2C_{\mathrm{tot}}^2} \tag{44}$$

Or

$$n > \sqrt{10\frac{R_{\mathrm{p}}2(1-\alpha)\delta(1-e^{-\frac{t}{\delta}})}{(1+R_{\mathrm{p}}^2\omega_0^2C_{\mathrm{tot}}^2)\rho_{\mathrm{co}}(1+\alpha)(1+\beta)}} \tag{45}$$

If R_{p} is large enough, n could be chosen to be 1 or 2 without damaging the signal strength.

If n is too large, the inductance of the sensor coil, which is specified by (6) increases dramatically, thus self-resonant frequency f_{SR}, which is specified by (36) may decrease too quickly. f_{SR} should always be greater than f_0, which may prevent us from obtaining a desirable f_0 which we discussed in section III.*A*, thus we found the upper bound for n:

$$n < \sqrt{\frac{R_{\mathrm{p}}^2(C_{\mathrm{p}}+C_{\mathrm{s}})}{\frac{\mu}{\pi}D(1+\alpha)\left(\ln\left(\frac{1+\alpha}{1-\alpha}\right)+0.18\left(\frac{1-\alpha}{1+\alpha}\right)+0.13\left(\frac{1-\alpha}{1+\alpha}\right)^2+0.726\right)\left(4\pi^2f_0^2R_{\mathrm{p}}^2(C_{\mathrm{s}}\right.}} \tag{46}$$

4.3.4 *Inner diameter to outer diameter ratio α*

α approaches 0 when copper trace covers all the plate's surface, and approaches 1 when there is only one turn. The first conjecture would suggest that α should be as small as possible, to make full use of limited plate surface area. But the numerical calculation result in Fig.4-14 by (44) shows us that when the turns number is small, optimized α is around 0.8, which results in a large uncovered area on the plate. When n increases, the optimized α converges to 0.38, which leaves some area uncovered. When the inner turns radiuses are too small, the turn's contribution to the mutual inductance is relatively small compared to the contribution to the series resistance, thus reducing the signal strength amplitude. The measurement results of PCB sensors have also been taken to verify the correctness of (42), as shown in Fig. 15, which could match the simulated curve. Because

in the progress of α optimization, we assumed that the other parameters (f_0,D,n,β) were kept same. But it was hard to control the same f_0 for every PCB sensor, thus the y-axis in Fig.4-15 is amplitude/resonant frequency.

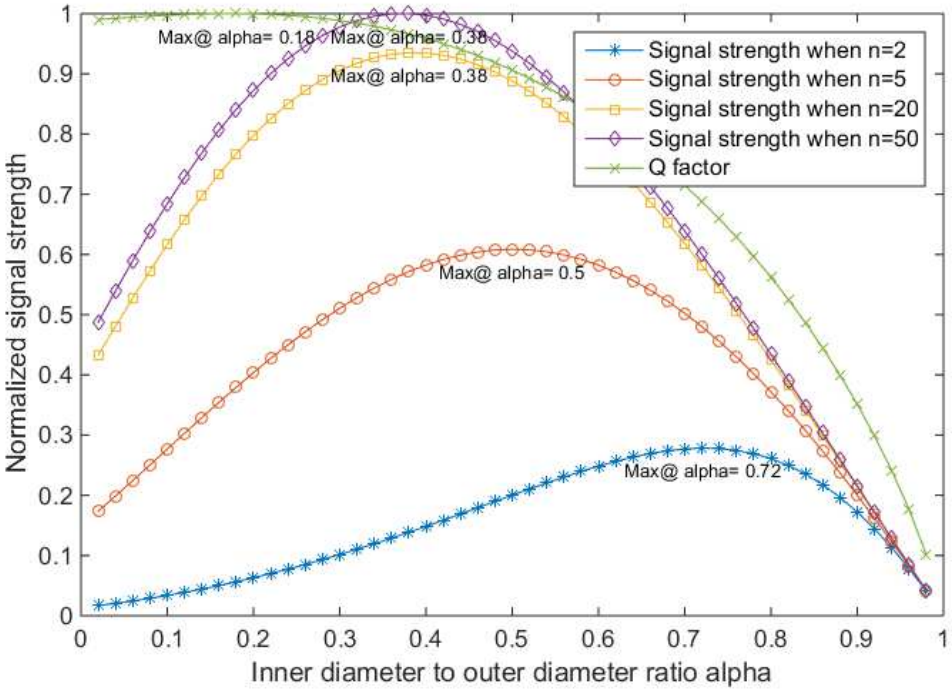

Fig. 4-14 Normalized signal strength vs. turns increase for a typical ICP sensor, for D = 5 mm, β = 0.8.

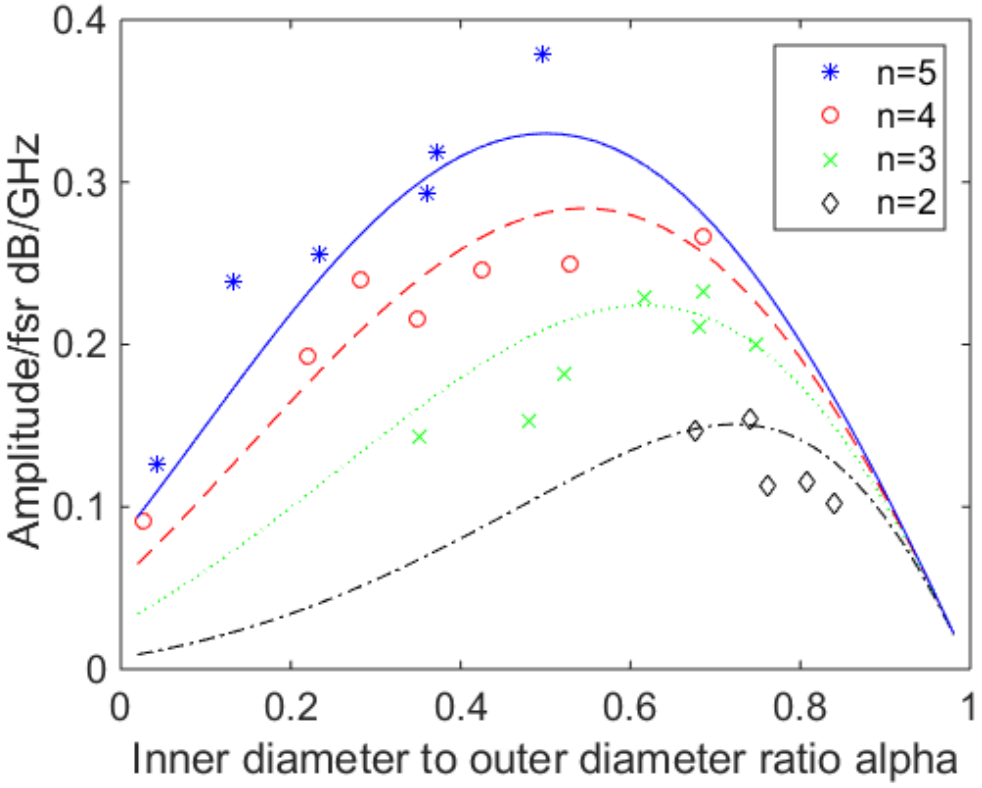

Fig. 4-15 Measurement result match the numerical calculation result of (42)

4.3.5 Spacing width to trace width ratio β

If *D, n, α* have been determined, the summation of trace width and spacing width, which is $s + W = (1 + \beta)W$, is determined by (1). Given this fixed summation width, the β ratio could determine the trace width and spacing width respectively. Mutual inductance is not influenced by the β change. On the other hand decreasing β could increase the trace width, thus decreasing the series resistance R_s, which may improve the signal performance. However, the only way this approach works is when C_s is relatively small when compared to C_{tot}. Equations (11)–(19) show that C_s increases if β decreases. If C_s dominates C_{tot}, and the influence of R_p is ignored, ω_0 is roughly estimated as：

$$\omega_0 = \sqrt{\frac{1}{L_2 C_s}} \tag{47}$$

And (44) is approximately

$$\text{amplitude} = \frac{{L_m}^2}{\frac{L_2\rho_{\text{co}}n^2(1+\alpha)(1+\beta)}{2(1-\alpha)\delta\left(1-e^{-\frac{t}{\delta}}\right)}\frac{\pi\epsilon_{\text{o}}\epsilon_{\text{r}}(l-4D)}{nln\left(1+\beta+\sqrt{\beta^2+2\beta}\right)}} \tag{48}$$

$$= K_{\beta}\frac{ln\left(1+\beta+\sqrt{\beta^2+2\beta}\right)}{(1+\beta)}$$

K_β represents the parameters which are not related to β. By solving $\frac{\partial R_{\text{sensor}}}{\partial \beta} = 0$, β = 0.8. Using numerical analysis, we find that

$$\text{amplitude}(0.4 < \beta < 1.8) > 0.9\text{amplitude}(\beta = 0.8)$$

Therefore, β in the range of [0.4, 1.8] is acceptable.

4.3.6 Copper trace thickness

The effective copper trace thickness is $\delta(1-e^{-\frac{t}{\delta}})$, which is dependent on the skin depth. When $t = \delta$, the effective thickness is 0.632 δ. When $t = 3\delta$, the effective thickness increases to 0.95 δ. So $t = 3\delta$ is a desirable choice of copper thickness. Excessive thickness may increase the complexity of the progress to fabricate sensors in the clean room.

4.3.7Substrate thickness

Substrate thickness could influence the R_{p} and C_{p}, but for the typical ICP sensor, the influence of these is relatively small. A more important factor to determine substrate thickness is the bend factor (Timoshenko et al 1959)**:**

$$y = \frac{\eta \cdot p \cdot D^4 12 \cdot (1-v^2)}{E \cdot {t_{\text{sub}}}^3} \tag{49}$$

Where, E is the substrate material elastic modulus, v is the Poisson ratio, b is a factor determined by the shape of the sensor plate, and p is the pressure applied on the sensor. The bend factor

determines the maximum pressure the sensor can withstand and the resolution of pressure measurement.

4.3.8 Other sensor shapes

Previous discussions focused on the square shaped coil.

For the circular shaped coil, (5) becomes

$$l = \frac{\pi}{2} n(1+\alpha)D \tag{50}$$

(6) becomes (Stojanović et al 2005)

$$L = \frac{2\mu}{\pi} n^2 d_{\text{avg}} \left(\ln\left(\frac{2.46}{\varphi}\right) + 0.2\varphi^2 \right) \tag{51}$$

The $\left(\frac{4}{\pi}\right)^2$ factor in (28) is eliminated.

For the rectangular coil, use (53), (54) where $D1$ and $D2$ are the side lengths of the rectangular coil, and g is the diagonal length.

$$l = n(1+\alpha)(D1+D2) \tag{52}$$

$$L = \frac{\mu}{\pi} * n\text{^}2 \left(-2(D1+D2) + 2g - D1 \ln\left(\frac{D1+g}{D2}\right) \right. \tag{53}$$
$$\left. - D2 \ln\left(\frac{D2+g}{D1}\right) + D1 \ln\left(\frac{2D1}{W}\right) + D2 \ln\left(\frac{2D2}{W}\right) \right)$$

4.3.9 Insulator layer between trace and substrate

FR4 is a good insulator, thus R_p for PCB is quite large, which is desirable. But for a silicon substrate, resistivity is relatively small, so R_p is normally in the kΩ range, which cannot be neglected. Adding an insulator layer between the copper and silicon can improve the sensor performance. So the SiO_2 layer's capacitance is:

$$C_{\mathrm{p}} = \epsilon_0 \epsilon_{\mathrm{ox}} \frac{Wl}{t_{\mathrm{ox}}} \tag{54}$$

An equivalent circuit model, shown in Fig. 4-16(a), is transferred to Fig. 4-16(b), which is similar to Fig. 4-4. But R_{p} and C_{p} are modified as:

$$C_{\mathrm{p}} = C_{\mathrm{ox}} \left(\frac{1 + \omega^2 (C_{\mathrm{si}} + C_{\mathrm{ox}}) C_{\mathrm{si}} R_{\mathrm{si}}^2}{1 + \omega^2 (\square_{\mathrm{si}} + C_{\mathrm{ox}})^2 R_{\mathrm{si}}^2} \right) \tag{55}$$

$$R_p = \frac{1}{\omega^2 C_{\mathrm{ox}}^2 R_{\mathrm{si}}} + \left(R_{\mathrm{si}} \left(\frac{(C_{\mathrm{si}} + C_{\mathrm{ox}})^2}{C_{\mathrm{ox}}^2} \right) \right) \tag{56}$$

From the equations, the insulator layer increases C_{p} slightly, but increases R_{p} dramatically. Therefore, it is recommended to add an insulator layer on the silicon substrate.

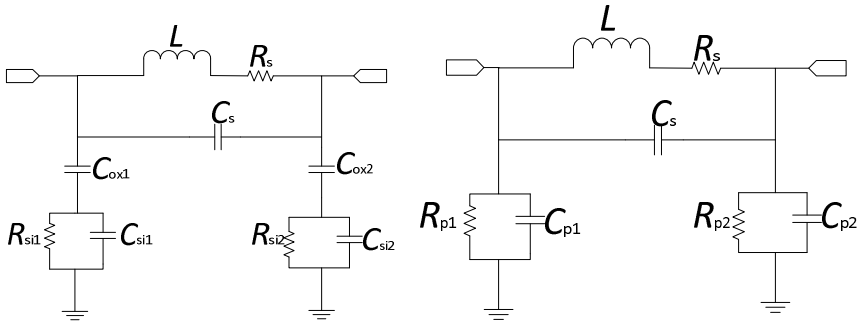

(a) (b)

Fig. 4-16 lumped (a) and equivalent (b) circuit model after adding SiO_2 insulator layer

4.4 Sensor design

4.4.1 PCB sensor

Based on the discussion in section III, a PCB sensor, which is: D = 5 mm, n = 2, W = s= 0.254 mm(which leads to α = 0.7859, β = 1), t_{cu} = 35 μm, plated separate distance = 75 μm, was fabricated. In the measurement set up, the sensor was placed in saline and the VNA probe was

placed 2 cm away. It was demonstrated that the sensor could sense the pressure change by resonant frequency shift, as shown in Fig. 4-17. There is a tradeoff between frequency resolution and measurement time consumption. Our homemade reader spends 165 μs for one increment of frequency. For a typical 5 MHz total measurement span and 50 kHz increment for one step, total time for one measurement is 16.2 ms, which can catch the cardiac cycle.

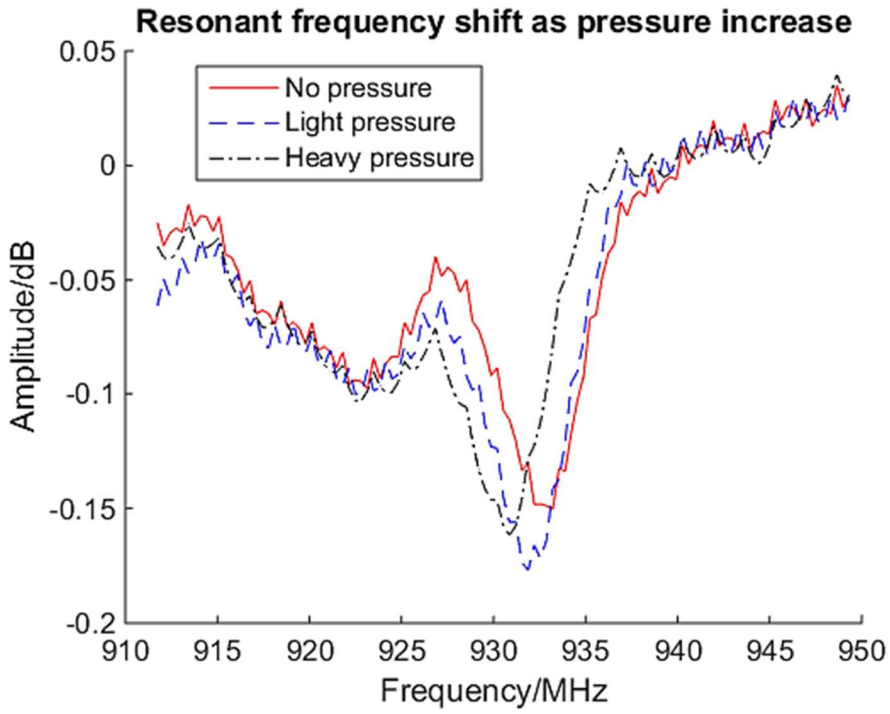

Fig.4-17. Resonant frequency shift as pressure changes.

4.4.2 MEMS sensor

We designed the MEMS sensor: 5 × 5 × 1.3 mm dies with 4 × 4 mm deformation diaphragm and 0.5 mm on boundary for anodic bonding, $n = 2$, $W = s = 0.2$ mm (which leads to $\alpha = 0.7895$, $\beta = 1$), $t_{silicon}$=50 μm, t_{SiO2}, t_{cu} = 10 μm, t_{cr} = 20 nm, t_{glass} = 500 μm, plated separate distance = 90 μm. Fabrication progress is shown in Fig. 4-18. Silicon substrate for one plate forms the deformation diaphragm.SiO_2 layer is the insulator layer, and Cr is the adhesive layer between silicon and SiO_2. A Solidwork simulation in Fig.4-19 showed that the capacitance change corresponded to the

pressure. It demonstrates the sensor's good linearity: $r = 0.99$, and frequency/pressure resolution is 40.9kHz/mmHg, as shown in Fig. 4-20.

The trick of MEMS sensor design is the coil was connected to a circular pad at the center. It is because silicon elastic modulus is much smaller than FR4, and the most obvious diaphragm deflection occurs at the center. To increase the frequency/pressure resolution, 2.4 mm diameter circular pad is necessary.

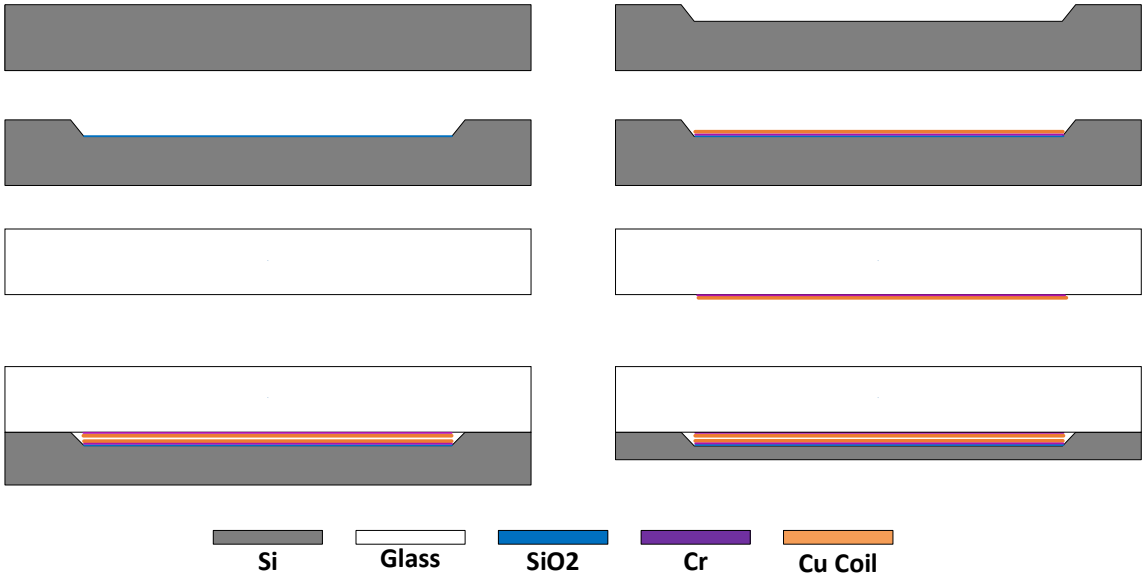

Fig. 4-18 Fabrication process of MEMS sensor

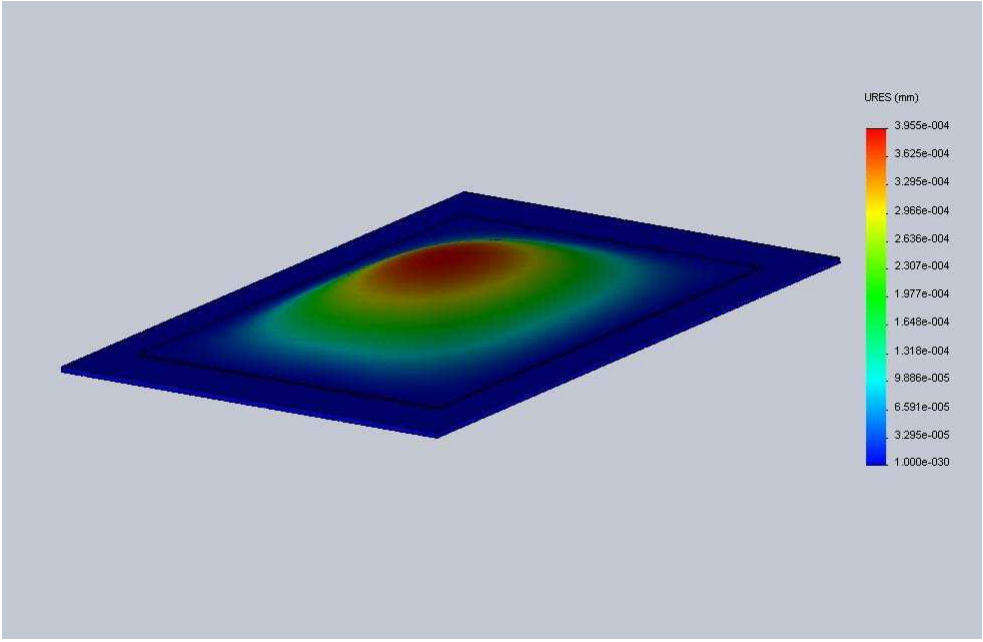

Fig. 4-19 Solidwork simulation result of diagram deformation at pressure when pressure = 20mmHg. Maximal deformation is 3.96e-04mm at this pressure

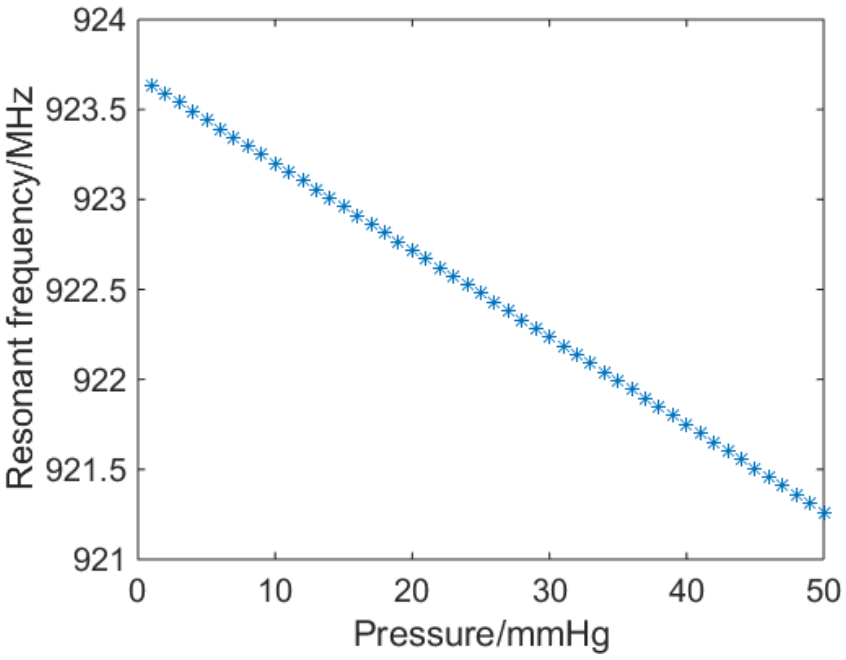

Fig 4-20. Simulated resonant frequency under pressure

CHARPTER 5. READER FOR THE PASSIVE SENSOR

This chapter 5 is partly taken from:

Fa Wang,, Xuan Zhang, Mehdi Shokoueinejad, John G. Webster, Bermans J. Iskandar, Joshua E. Medow. A novel intracranial pressure read out circuit for passive wireless LC sensor. Revision. Feb 2017 IEEE Trans. Instrum. Meas.

5.1 Methodology

5.1.1 System model

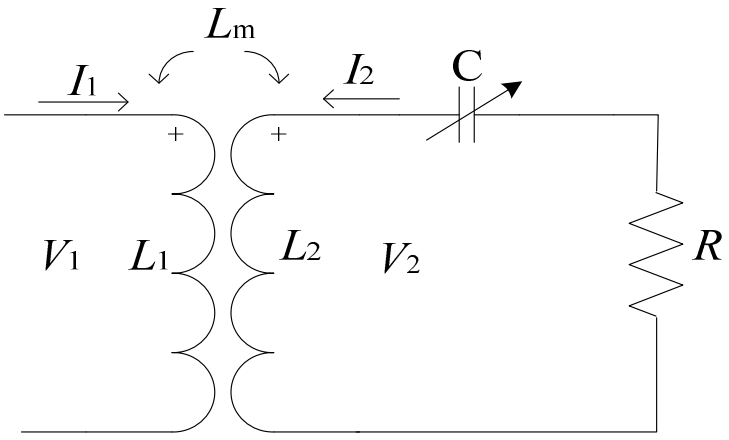

Fig. 5-1. Antenna coupling with sensor circuit model. Inductive coupling factor is L_m, and a current I_1 flows through into the antenna, and excites the current in sensor I_2

Based on Kirchhoff's law:

$$V_1 = j\omega L_1 I_1 + j\omega L_m I_2 \quad (1)$$

$$V_2 = j\omega L_2 I_2 + j\omega L_m I_1 \quad (2)$$

$$V_2 = -RI_2 - \frac{1}{j\omega C} * I_2 \tag{3}$$

From equations (1) ~ (3) we solve Z_1:

$$Z_1 = \frac{V_1}{I_2} = j\omega L_1 - \frac{j\omega^2 L_m^2}{j\omega L_2 + R + \frac{1}{j\omega C}} \tag{4}$$

To make (4) more clear, we define $\omega_0 = \frac{1}{\sqrt{L_2 C}}$, coupling factor $k = \frac{L_m}{\sqrt{L_1 L_2}}$, and quality factor $Q = \frac{\omega_0 L}{R}$ and substitute into equation (4), which results in:

$$Z_1 = j\omega L_1 \left(1 + \frac{k^2 \left(\frac{\omega}{\omega_0}\right)^2}{j\frac{1}{Q}\frac{\omega}{\omega_0} + 1 - \left(\frac{\omega}{\omega_0}\right)^2}\right) \tag{5}$$

Fig. 5-2 shows Z_1 is a function of $\frac{\omega}{\omega_0}$. $f\left(\frac{\omega}{\omega_0}\right) = 1 + \frac{k^2 \left(\frac{\omega}{\omega_0}\right)^2}{j\frac{1}{Q}\frac{\omega}{\omega_0} + 1 - \left(\frac{\omega}{\omega_0}\right)^2}$. The maximum impedance of the whole system is measured when the exciting current from the reader sweeps frequency to near but lower than the sensor resonant frequency, and then decreases sharply. System impedance becomes minimal when the sweeping frequency nears but is larger than the resonant frequency. The maximal phase change is measured at resonant frequency. Fig. 5-3 shows that by measuring the impedance of the antenna and sensor system from the antenna side, sensor resonant frequency is tracked.

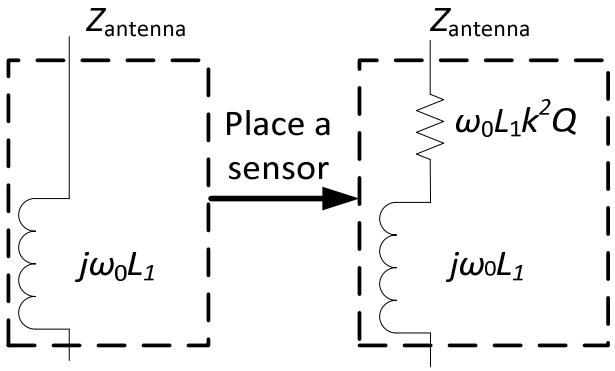

Fig. 5-2. The sensor, with qualify factor *Q*, placed nearby the antenna, with a coupling factor *k*, changes the whole system's impedance

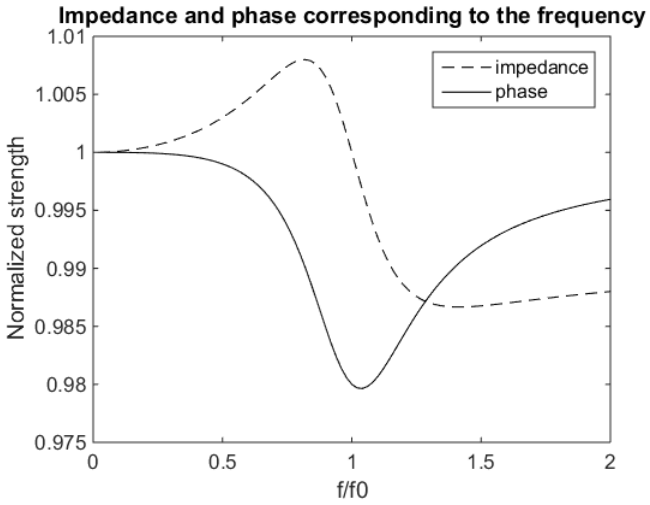

Fig. 5-3. Impedance and phase frequency response. Impedance and phase change sharply at the resonant frequency, which help to track the resonant point.

At resonant frequency,

$$Z_1|_{\frac{\omega}{\omega_0}=1} = j\omega_0 L_1 + \omega_0 L_1 k^2 Q \tag{6}$$

Eq. (6) and Fig. 4 show the impact of the sensor at resonant frequency to the whole system is equivalent to a series R_{sensor} value of $\omega_0 L_1 k^2 Q$ to the antenna's inductor. This equivalent resistor changes the system's impedance and phase sharply at resonant frequency.

5.1.2 Impedance measurement principle

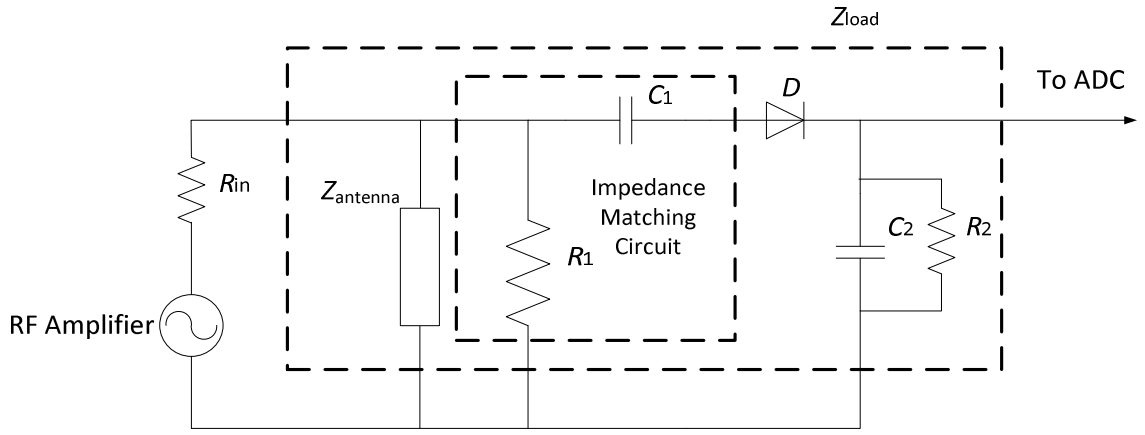

Fig. 5-4. Measurement principle. Impedance of the antenna and sensor coupling system functions as the load for the RF amplifier.

Fig.5-4 demonstrates a novel measurement principle to detect the sensor's resonant frequency. R_1 = 58 Ω and C_1 = 1000 pF form the impedance matching circuit to ensure $|Z_{\text{load}}|$ is close to 50 Ω at a wide frequency range when the sensor is not placed near the antenna. Fig. 6 shows that adding a series resistor to the antenna inductor will break this impedance matching and change the RF amplifier's output. To avoid using expensive high speed ADC, the envelope of the output signal is recovered by bypassing the output signal to a typical half-wave rectifier, which consists of D, C_2 = 3.3 pF R_2 = 2000 Ω. Thus the RF signal amplitude becomes quasi-static and could be easily measured by the microcontroller ADC.

The impact of R_{sensor} to the whole system's impedance Z_{load} is sensitive to the values of R_1, C_1, R_2, and C_2. Given the above stated value chosen in this prototype and assuming antenna inductance equal to 230 nH (the inductance of smaller antenna in the prototype, which is discussed in (section D of section. (II)), we solved the complicated series–parallel circuit equations. Fig. 6 shows that adding equivalent resistor R_{sensor} in series always decreases the Z_{load} when the resonant frequency range is from 35 MHz to 2.7 GHz. The output amplitude sent to the ADC is equal

to $\frac{2|Z_{load}|}{R_{in}+|Z_{load}|}V_{\text{match}}$, where V_{match} is the amplitude of signal source output for impedance matching. Thus output signal drops sharply at resonant frequency, which is $\left(1-\frac{2|Z_{load}|}{R_{in}+|Z_{load}|}\right)V_{\text{match}}$. The amplitude of signal drop is defined by $\omega_0 L_1 k^2 Q$. By solving the series–parallel circuit equations, Fig. 5-5 shows the relationship between the amplitude of signal drop $\left(1-\frac{2|\text{Z}_{\text{load}}|}{R_{\text{in}}+|\text{Z}_{\text{load}}|}\right)V_{\text{match}}$ and R_{sensor} ($\omega_0 \text{L}_1 k^2 Q$). In the above analysis the assumption value of L_1 is defined by the antenna's size and number of turns, which has been employed in the prototype. However this outcome remains the same if other antenna designs were employed.

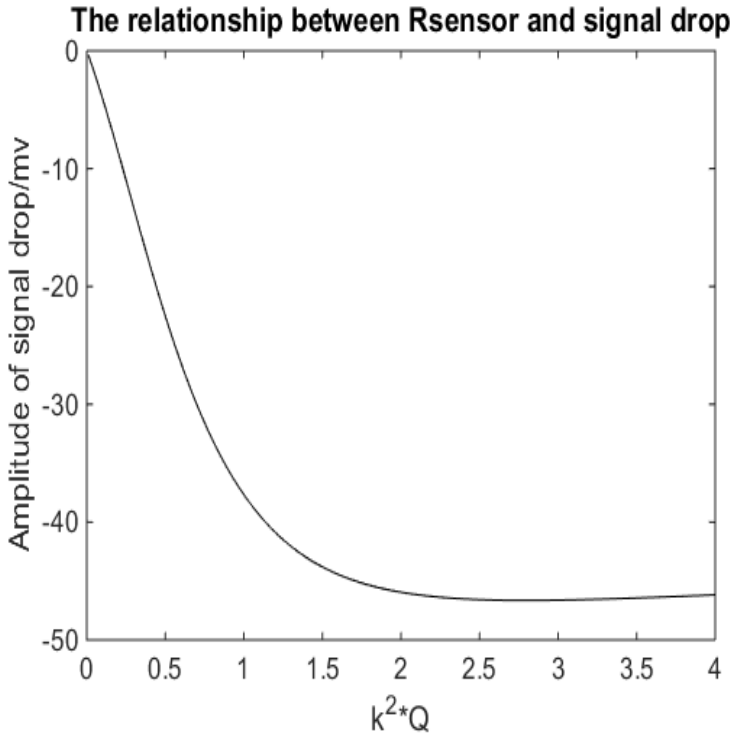

Fig. 5-5. The maximal output signal amplitude drop corresponding to the k^2Q, assuming V_{match} = 1 V, $\omega_0 = 600$ MHz(resonant frequency of sample PCB sensor in the prototype) and L_1 = 230 nH.

5.2 Method

5.2.1 Device overview

Fig. 5-6 shows the device flow chart. An RF signal generator is controlled by a microcontroller to sweep in the frequency range in which the sensor's resonant frequency located. An RF amplifier enhances the RF signal with a constant power output when the load impedance matched (9 dBm when load equals 50 Ω). When the antenna-sensor coupling system forms the load, any change of the antenna-sensor coupling system's impedance results in the change of the RF amplifier output. It is hard to measure the RF amplifier output directly due to its high frequency. A half-wave rectifier recovers the envelope amplitude. The amplitude value is sent back to the microcontroller for signal processing. At the same time, it is also sent to a NI DAQ, and is recorded by LabVIEW as a txt file. Fig.5-8 shows MATLAB software processes the signal data.

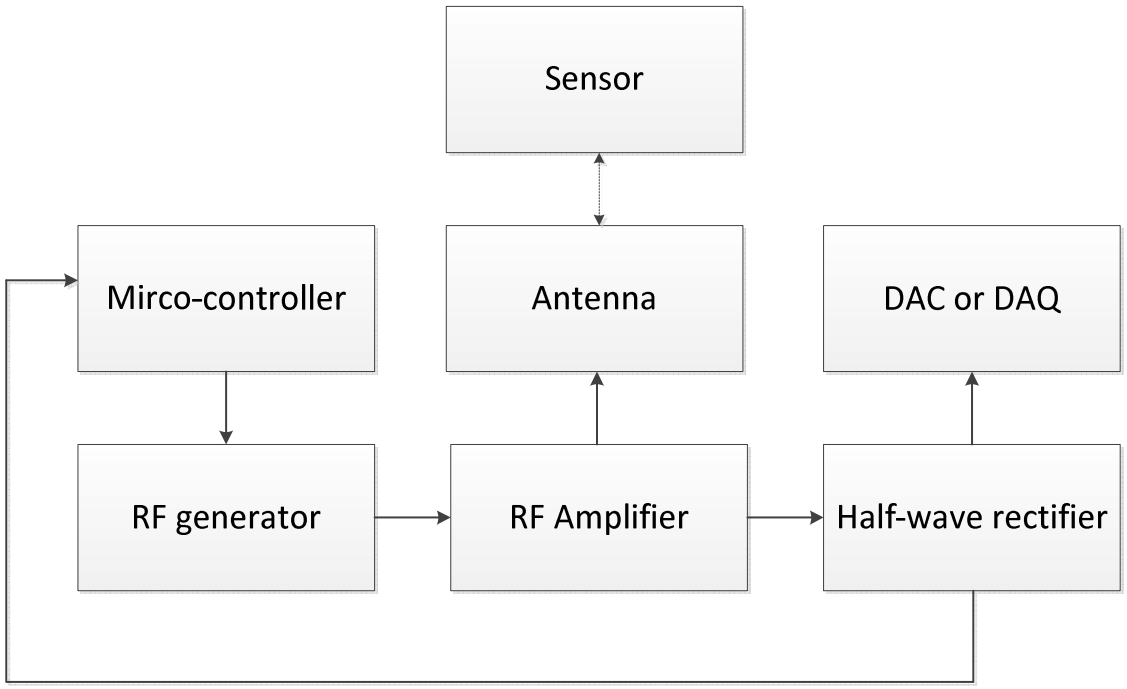

Fig. 5-6. Flow chart of system design.

5.2.2 RF signal generator and microcontroller

Currently, diaphragm based pressure sensors for ICP or intraocular pressure (IOP) measurement resonate from 63 MHz to 2.45 GHz (Chen et al 2014, Kawoos et al 2005, Park et al 1998, Chitnis

et al 2013). A slight difference of coil pattern design on the chip or distance between coils results in a huge difference in resonant frequency. Thus this telemetry device is adapted to an ultra-wide frequency range.

An ADF4351 chip (Analog Devices) is the main component for the RF signal generator. The ADF4351 has an integrated voltage-controlled oscillator (VCO) with an output frequency ranging from 2200 MHz to 4400 MHz. In addition, divide-by-1/-2/-4/-8/-16/-32/-64 circuits allow the user to generate RF output frequencies as low as 35 MHz. The output frequency is set by six inner registers through an SPI interface. A Microcontroller dsPIC33FJ32GP202 writes these registers to make the ADF4351 generate a sweeping RF signal in a specified range. The dsPIC33FJ32GP202 chip is a low cost microcontroller with an advanced built in ADC. This ADC measures the amplitude of the envelope of the RF amplifier output signal.

5.2.3 RF amplifier, impedance matching and half-wave rectifier

The AD8353 (Analog Devices, Inc.) with input/output internally matched to 50 Ω, provides a constant 9 dBm output when the load impedance is matched. A high pass filter consisting of a 58 Ω resistor and 1000 pF capacitor matches the impedance over a wide frequency range. An integrated half-wave rectifier, LT5505 (Linear Technology, Inc.), measures the amplitude of the AD8353 output signal's envelope.

5.2.4 Antenna

A single turn loop antenna features a low coupling factor in near field, which is unfavorable in this system. A multiple turn loop antenna usually corresponds to a high parasitic capacitance, which is unfavorable in the GHz range.

We used a spiral square antenna because it was able to overcome these two disadvantages. Fig. 5-8 enlarged photo shows two spiral antennas printed on the PCB, with parameters listed in table

5-I. A smaller antenna could achieve higher signal strength when the distance between sensor and antenna is closer (smaller than 4 mm).

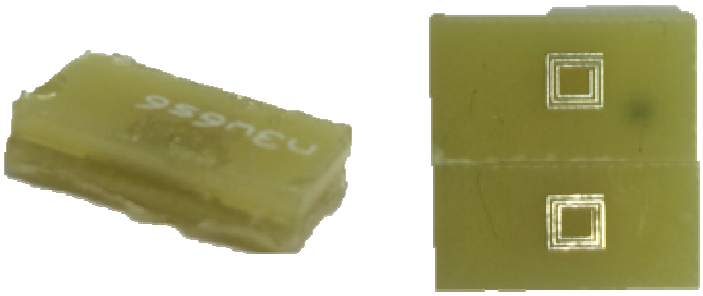

Fig. 5-7. Spiral square antennas mounted on a PCB.

TABLE 5-I PARAMETERS FOR TWO ANTENNAS

	ANT1	ANT2
Outer radius	5 mm	8 mm
Trace width	0.254 mm	0.254 mm
Spacing width	0.254 mm	0.254 mm
Turns	8	13
Inner radius	1.44 mm	1.904 mm
Self-inductance	230 nH	1700 nH

5.2.5 Sensor

Fig. 5-7 shows the sensor is fabricated on a PCB, and cut into small pieces by a Computer Numerical Control router (CNC). **Table 5-II** lists the parameters. The whole sensor was sealed by E6000 Viscosity Auto/Industrial Adhesive for waterproofing.

Sensor Parameter

TABLE 5-II

Outer radius	2 mm
Trace width	0.152 mm
Spacing width	0.152 mm
Turns	3
Trace thickness	35 μm
Plate thickness	1.57 mm
Distance between two plates	35 μm
Self-inductance	59.6 nH
Quality factor	133.4

5.3 Measurement

5.3.1 Experiment setup

Fig. 5-8 shows the measurement set up. A transparent plastic graduated cylinder supports a column of fluid to simulate intracranial pressure. The 55 cm height of this cylinder simulates pressure ranges from 0 mmHg (0 cmH_2O) to 40 mmHg (54.38 cmH_2O). The sensor is placed at the bottom of cylinder, aligned with the antenna. The position of cylinder is fixed and the position of antenna is adjustable by a screw, to control the distance between sensor and antenna.

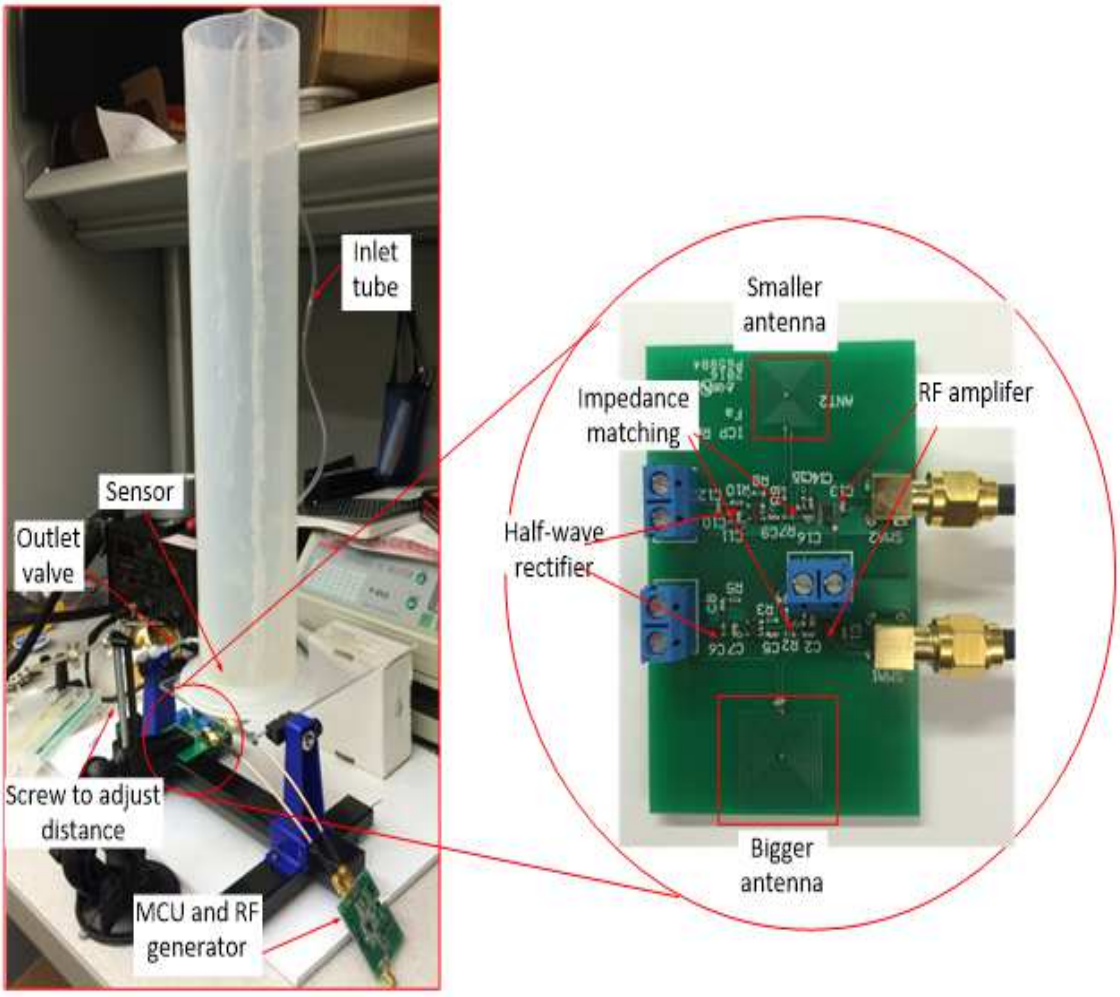

Fig. 5-8. Measurement set up with sensor at the bottom of water column.

5.3.2 Measurement result

The telemetry device swept twice in the range where the sensor's resonant frequency is located. The first time it swept without the sensor, and the second time with the sensor coupling. When the sensor is absent, the antenna's impedance which is defined as $Z_{\text{antenna}} = j\omega L_1$ forms the only load. When the sensor is present, the whole system's impedance Z_1 : $Z_1 = j\omega L_1\left(1 + \frac{k^2\left(\frac{\omega}{\omega_0}\right)^2}{j\frac{1}{Q}\frac{\omega}{\omega_0}+1-\left(\frac{\omega}{\omega_0}\right)^2}\right)$ forms the output load of the RF amplifier . The difference between the two signals, is the sensor's impedance: $Z_{\text{sensor}} = Z_1 - Z_{\text{antenna}} = j\omega L_1\left(\frac{k^2\left(\frac{\omega}{\omega_0}\right)^2}{j\frac{1}{Q}\frac{\omega}{\omega_0}+1-\left(\frac{\omega}{\omega_0}\right)^2}\right)$ .The sensor's impedance Z_{sensor} (at resonant frequency, transferred to pure resistance R_{sensor}) yields the output voltage drop at resonant frequency of the sensor Fig. 5-9 shows data collected by LabVIEW DAQ, and processed and displayed in MATLAB. The device's microcontroller also collects data using its own built-in DAC.For real time ICP monitoring, the first sweep (without sensor) only needs to be done once then stored when the reader initializes.

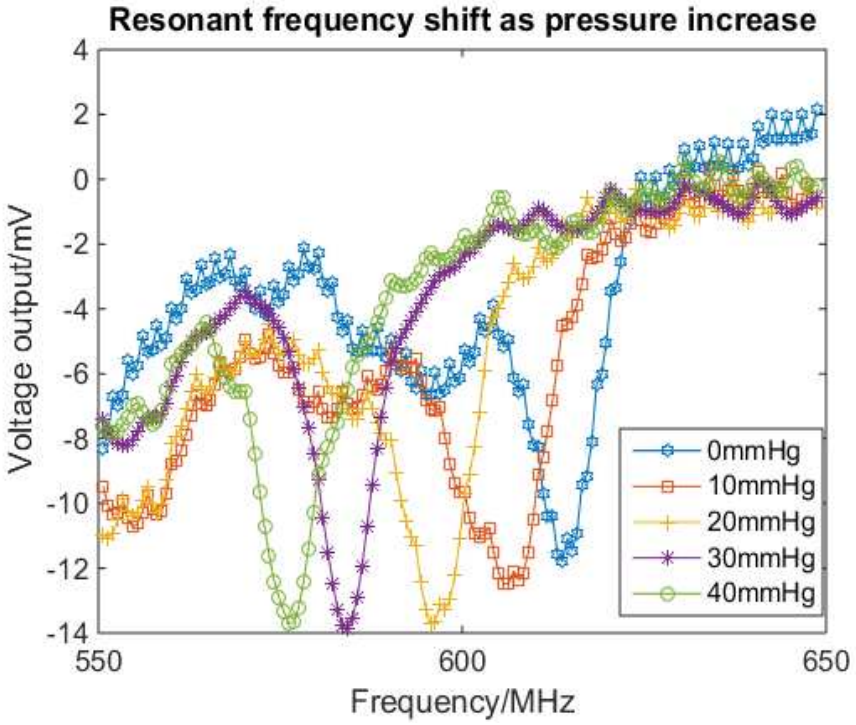

Fig. 5-9. Resonant frequency shift as pressure increases, at measurement distance 5 mm

Fig. 5-10 was collected by varying the sensor to antenna distance. The initial distance was 3 mm and each increment was 3 mm, yielding a range of 3 mm to 21 mm.

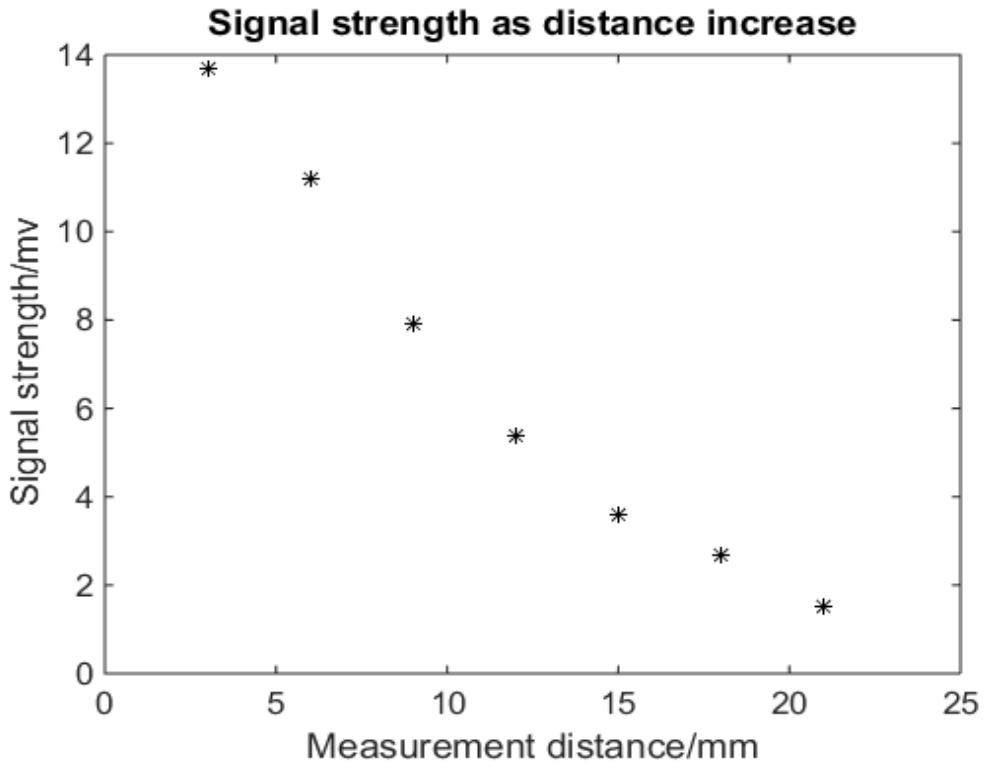

Fig. 5-10. Signal strength vs distance.

5.3.3 Measurement time

The sample frequency of our telemetry device is more than 6 Hz, which is suitable to catch the heartbeat for ICP monitoring. Below explains the detailed time consumption for one measurement.

First, the time required for the Serial Peripheral Interface (SPI) communication between microcontroller and RF generator for one step (changing output frequency once) consists of: 0.04 μs for each machine cycle (25 MHz crystal) times 4 cycles for one bit SPI communication bytes times 34 bytes per register (32 bytes data per register add start and stop bytes) times 6 registers for changing output frequency which totals to 32.64 μs.

Second, the RF generator phase lock time delay is 60 μs.

Third, because the value of the capacitor and the resistor in the LT5505 half-wave rectifier is relatively small (R = 2 kΩ, C = 3.3 pF, the time constant is 6.6 ns), thus this part of time consumption is neglectable.

Last is the ADC conversion time. The dsPIC33FJ32GP202 features an automatic ADC conversion speed up to 1.1 Msps (0.99 μs for one sample). For each step, 10 samples are measured and taken average.

Thus the total time consumed for one step is 102 μs. For a typical 10 MHz sweep range and a 10 kHz sweep resolution, a total sweep time is around 0.102 s. In practice, we take the component's setup time and signal processing time into consideration, causing the measurement time to be more than 0.15 s. If we could narrow the frequency range, or decrease the frequency resolution (increase the step length for one increment), this time could be shortened.

5.3.4 Measurement resolution and measurement accuracy

The frequency-to-pressure responsivity of this sample PCB sensor is 0.92 MHz/mmHg. The MEMS sensor usually has lower responsivity because of the high Young's modulus of silicon, for example: 120 kHz/mmHg (Akar et al 2001); 160 kHz/mmHg (Chen et al 2010). The minimal resolution of our telemetry device is 0.5 kHz, which corresponds to 0.84×10^{-3} mmHg, with the phase noise at 600 MHz specified by Fig. 5-11.

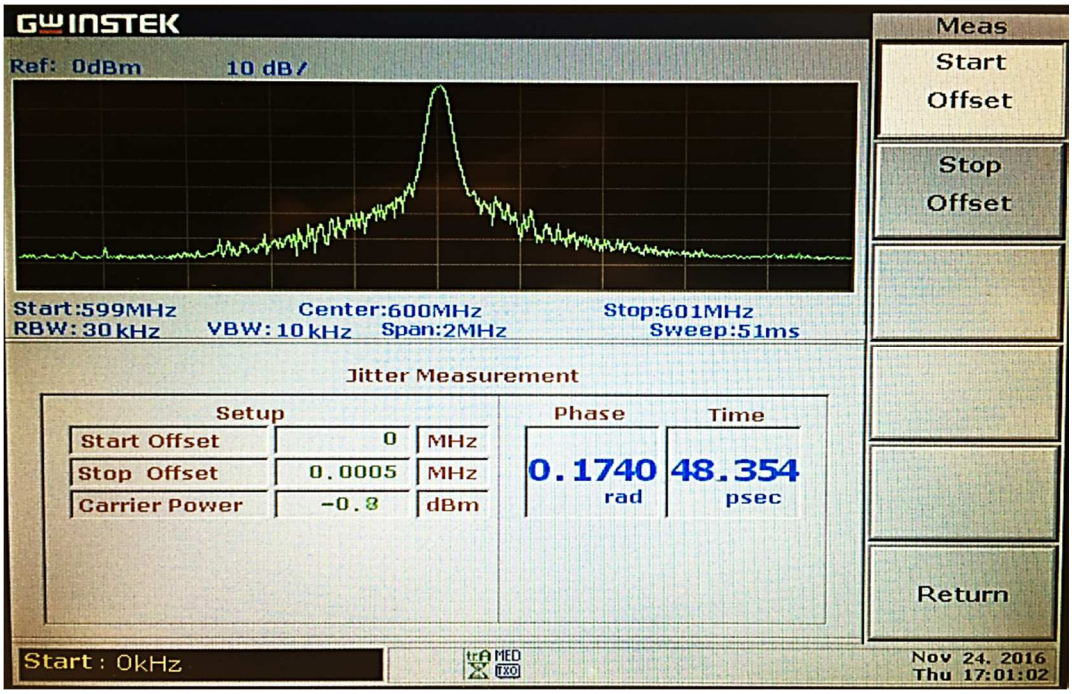

Fig. 5-11. Phase noise at 600 MHz

5.4 Discussion

The section discusses the considerations which may improve the measurement distance of the telemetry device.

5.4.1 Antenna radius

Fig. 5-3 shows maximal amplitude of signal drop at resonant frequency, is positively correlated to k^2Q. Antenna geometry influences the k factor, which was implemented in the design.

The mutual inductance between the telemetry device antenna and spiral coil on the sensor is specified by

$$k = \frac{L_m}{\sqrt{L_1 L_2}} \tag{7}$$

L_m is calculated as (Raju et al, 2014):

$$L_{\mathrm{m}} = \left(\frac{4}{\pi}\right)^2 \sum_{i=1}^{i=n_a} \sum_{j=1}^{j=n_b} M_{ij} \tag{8}$$

$$M_{ij} = \frac{\mu_0 \pi a_i^2 b_j^2}{2\left(a_i^2 + b_j^2 + z^2\right)^{\frac{3}{2}}} \left(1 + \frac{15}{32}\gamma_{ij}^2 + \frac{315}{1024}\gamma_{ij}^4\right) \tag{9}$$

$$\gamma_{ij=\frac{2a_i bj}{a_i^2+b_j^2+z^2}} \tag{10}$$

Where μ is the vacuum magnetic permeability: $\mu_0 = 4\pi \times 10^{-7}$. a_i is the i^{th} turn radius of antenna, and b_j is the jth turn radius of the sensor's coil, z is the distance between antenna and sensor.

Planar spiral inductor's inductance has been well studied. Mohan et al. described that, for the square shape planar spiral inductor, the inductance is expressed as (Mohan et al 1999)

$$L = \frac{2\mu_0}{\pi} n^2 d_{\mathrm{avg}} \left(\ln\left(\frac{2.07}{\varphi}\right) + 0.18\varphi + 0.13\varphi^2\right) \tag{11}$$

d_{avg} is the average diameter of the square, which is $\frac{D+D_{in}}{2}$. $\varphi = \frac{1-\alpha}{1+\alpha}$, α is the ratio of outer diameter to inner diameter.

Fig. 5-12 shows the k factor for two antenna with distance varying based on (7)~(11), given the antennas' and sensor's sizes. A small antenna features higher k factor at close distance (<3.8 mm), and bigger antenna's performance at longer distance is better.

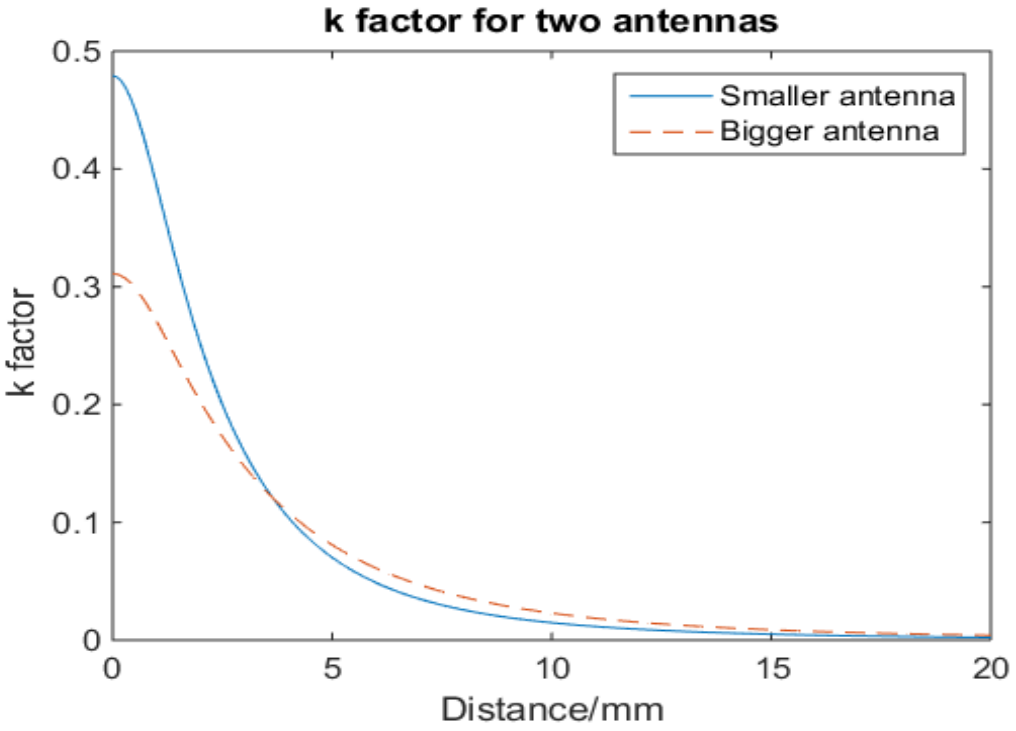

Fig. 5-12. K factors for two antennas decreases with.distance

5.4.2 More radiation power and RF safety

The maximum power the telemetry device radiates is 9 dBm when impedance is perfectly matched. Higher output power could obviously improve the signal strength and distance range measurement. The main constraint which limits increasing radiation power is the specific absorption rate (SAR). We developed a COMSOL stimulation to test our prototype's SAR simulation, which is based on COMSOL application 2190 (Comsol 2011). The brain's geometry was built based on "The Stanford volume data archive" (Levoy et al 2002), and Schmid et al.'s work on dielectric properties of human brain tissue (Schmid et al 2003). The antenna was placed 1 mm away from the left side of the head. Table 5-III lists parameters.

TABLE 5- III ANTENNA PARAMETERS

Parameter description	Value and Unit
Antenna	
Trace conductivity	5.96×10^7 S/m
Current	0.0126 A (50 Ω matched)
Trace outer size	10×10 mm
Trace turns	8
Trace width	0.25 mm
Trace spacing	0.25 mm
PCB size	30×30 mm
PCB relative permittivity	5.23
PCB relative permeability	1
PCB conductivity	0 S/m
Head	
Tissue basic relative permittivity	58.13
Tissue relative permeability	1
Tissue basic conductivity	1.15 S/m

Fig. 5-13 demonstrates that spatial peak SAR is less than 0.03 W/kg as averaged over 1 g of tissue, which is far below the IEEE regulations (Armahin et al 1995): maximal 8 W/kg as averaged over 1 g of tissue and 0.4 W/kg as averaged over the whole body. We tried to increase the current and found that when the radiation power increased to 30 dBm (current is 0.14 A), spatial peak SAR reached the IEEE limit. We predict that this maximal radiation power could be 141 times higher SNR at the same measurement distance, or a 5.2 times further measurement distance (coupling factor deceases as the distance $1/R^3$).

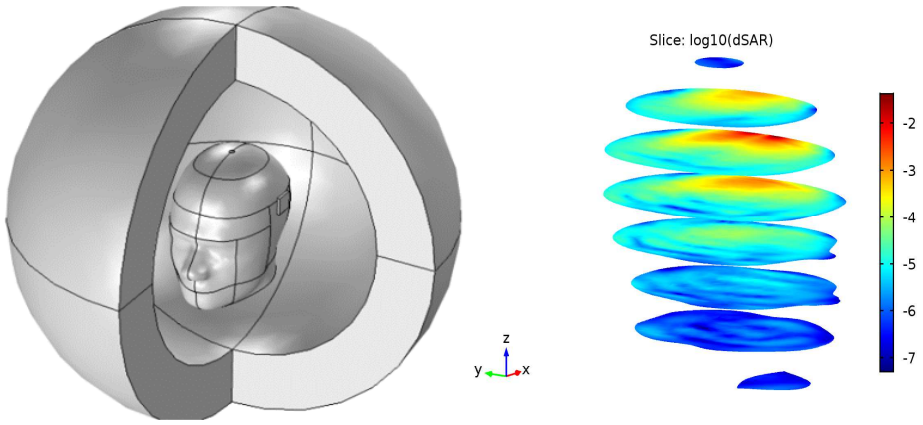

Fig. 13. Biosafety simulation result. Left is the simulation model in COMSOL. PCB antenna is placed close to the left side of the human head. Right is the SAR distribution in the head tissue. The result is in log scale. Red points (–2) mean that the spatial peak SAR in this area is larger than 0.01 W/kg.

5.4.3 Analog-to-Digital Convertor

Currently the maximal ADC input from the half wave rectifier is 1 V (when impedance matched), which doesn't make full use of the ADC dynamic range (3.3 V). In the future, we could amplify the signals from the half wave rectifier by a factor of 3 before sending them to the ADC.

In addition, currently we adapt the 12 bits ADC. In the future, a standalone ADC which has higher resolution could improve the signal quality performance.

5.4.4 Signal processing

Fig. 16 shows that the signal directly from the ADC is noisy. We applied a digital filter to the original signal to increase the SNR. Using the Fourier transform, we determined that the noise power spectrum distributed over a wide frequency range and the signal were located in a low frequency range. A moving average, which works as a low pass filter removed the noise:

$$Ly_s(i) = \frac{1}{2N+1}\big(y(i+N) + y(i+N-1) + \cdots + y(i-N)\big) \tag{12}$$

We chose $N = 5$.

However the signal from the moving average was not satisfactory. A further signal processing method is based on the moving average, known as Local Regression (Cleveland et al 1996). This algorithm assigned regression weights to the value within a dynamic range with a length chosen to be 5:

$$w_i = \left(1 - \left|\frac{x - x_i}{d(x)}\right|^3\right)^3 \tag{13}$$

Where x is the predicted value associated with the original signal data to be smoothed, x_i is the neighbor of x in the dynamic range, and $d(x)$ is half of the dynamic range length at the x-axis. Based on these weights, we performed a weighted linear least-squares regression. The regression used a second degree polynomial. Fig. 5-14 shows the final denoised result.

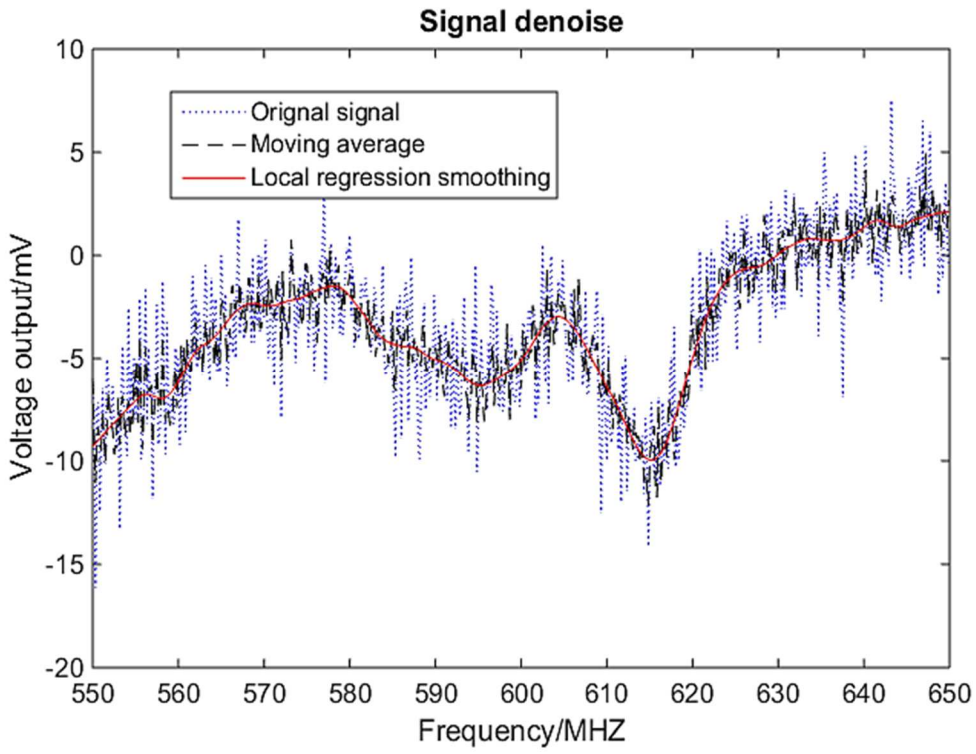

Fig. 5-14. Measurement data with 0 mmHg pressure: original data, moving average result, local regression smoothing result.

CHATPER 6: RFID BASED ICP MANAGEMENT SYSTEM: SMART SHUNT

This chapter 6 is partly taken from patent:

Bermans Iskandar,Joshua Medow,Christopher Luzzio,John Webster,Mehdi Shokoueinejad Maragheh,Fa Wang,Xuan Zhang,CEREBROSPINAL FLUID SHUNT VALVE SYSTEM

6.1. System overview

Real-time ICP data could also be applied to the implantable ICP management system, as the part of the closed loop control system. Whole system consists of : a catheter implanted within the brain of the patient with a proximal portion within the brain opposite a distal portion diverting CSF out of the brain to another region of the patient; a sensor implanted within the brain of the patient and producing a signal representing an intracranial pressure (ICP); a valve that permits excess CSF to drain out of the brain through the catheter in an open position and prevents the excess CSF from passing out of the brain through the catheter in a closed position; and a valve driver receiving the signal representing the ICP controlling the valve to switch the valve between the open position and closed position in a cycle for successive cycles so that the relative time that the valve is in the open position versus the closed position is a function of ICP as shown in fig 6-1. Telemeter is located outside the human head. Sensor tag, pressure sensor, valve driver and ICP valve are implantable parts, among them, sensor tag, pressure sensor and valve driver are implanted between skull and scalp, and sensor is implanted through dura layer which membrane may contact with CSF.

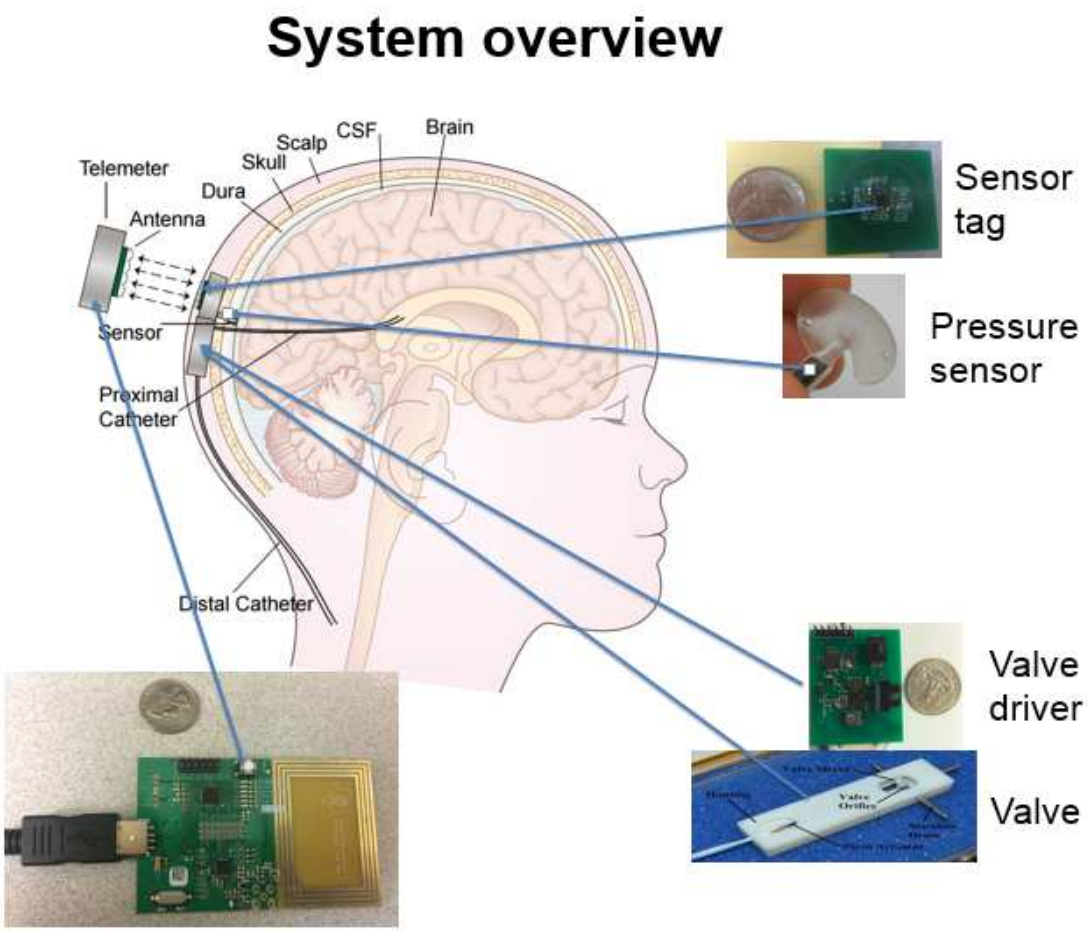

Fig. 6-1. ICP management system overview. It consists of telemeter, sensor tag, pressure sensor, valve driver and valve

6.2 Telemeter

The telemeter is an ISO15693 RFID reader, which based on the TRF7970 (Texas Instruments Inc). The telemeter could provide up to 200 mW radiation power to wirelessly charge the whole implantable part. The CLRC663 based (NXP Semiconductors N.V.) RFID reader, which could provide up to 2 W radiation power is also developed.

Beside the wireless charging function, the telemeter could also read real-time ICP data and transfer them to the computer, as shown in Fig. 6-2.

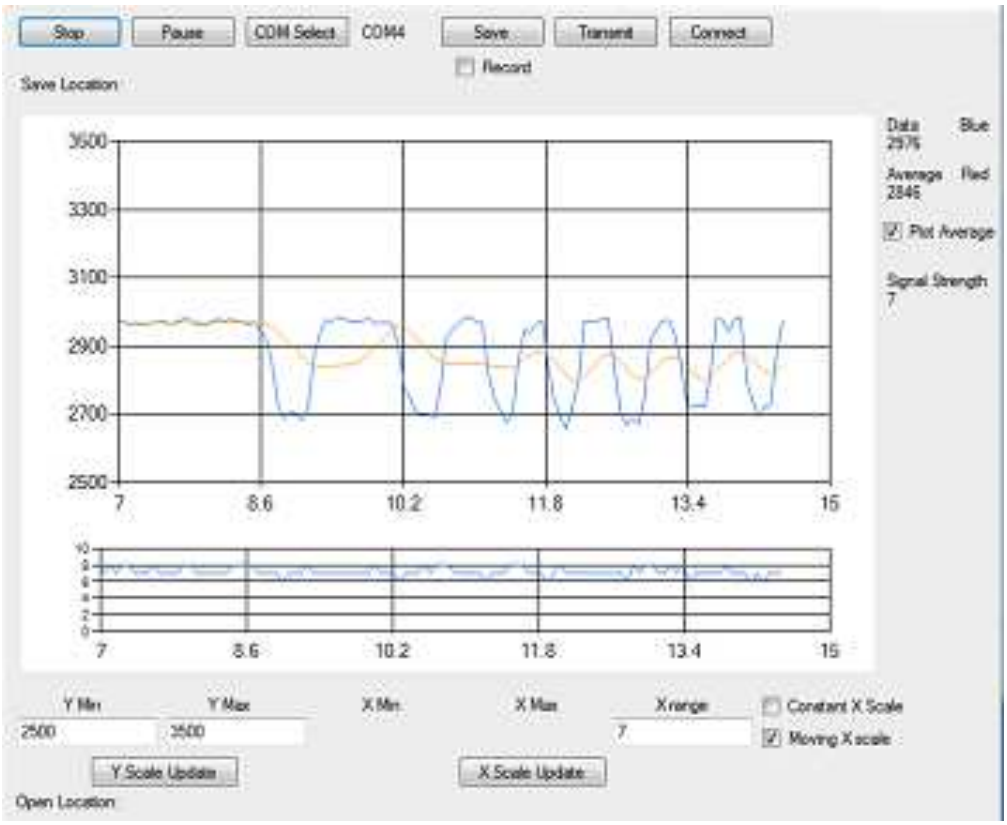

Fig. 6-2. Real-time ICP monitoring GUI on the computer, which connect to the telemeter

The telemeter could also transfer the commands to the implantable part. Fig. 6-3 is a demo to show that the physician could use the computer to change the parameter of the embedded system of the implantable part.

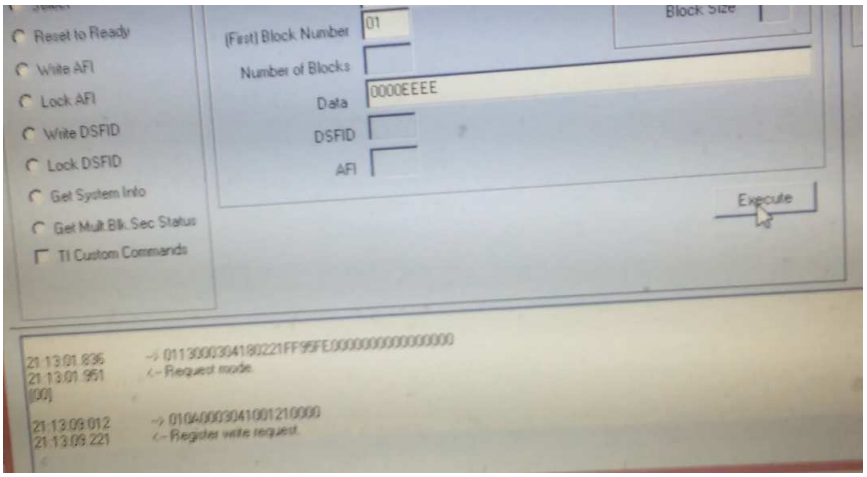

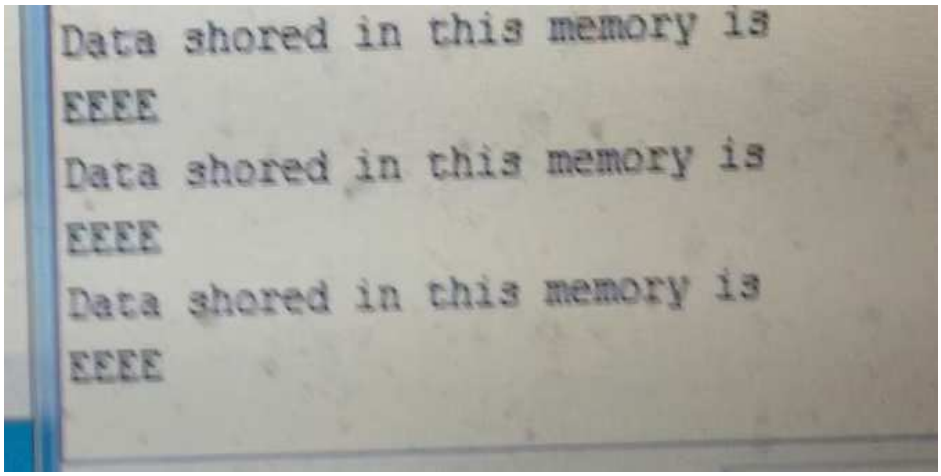

Fig. 6-3. A demo to show memory data in the embedded system of implantable parts could be edited by the telemeter.

6.3 Sensor tag

The sensor tag is based on the RF430FRL15xH NFC ISO 15693 Sensor Transponder (Texas Instruments Inc), as shown in Fig 6-4. It could achieve ISO/IEC 15693 wireless communication protocol, power supply from 13.56 MHz H-Field, and up to 4 cm wireless charging distance, as shown in Fig 6-5.

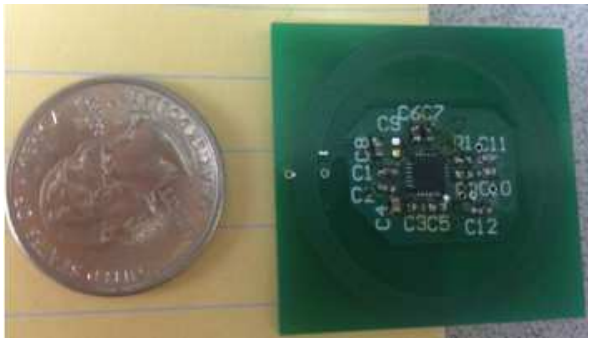

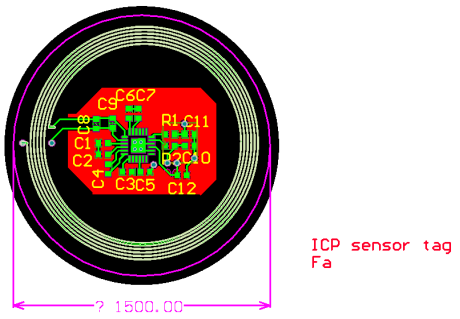

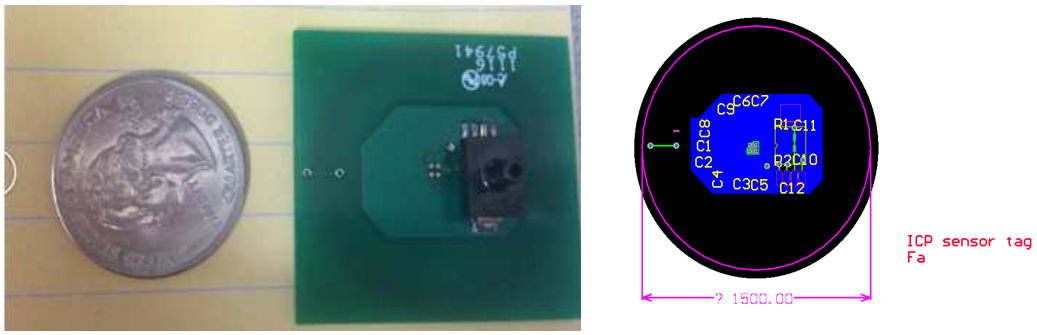

Fig. 6-4. Sensor tag: PCB design and prototype

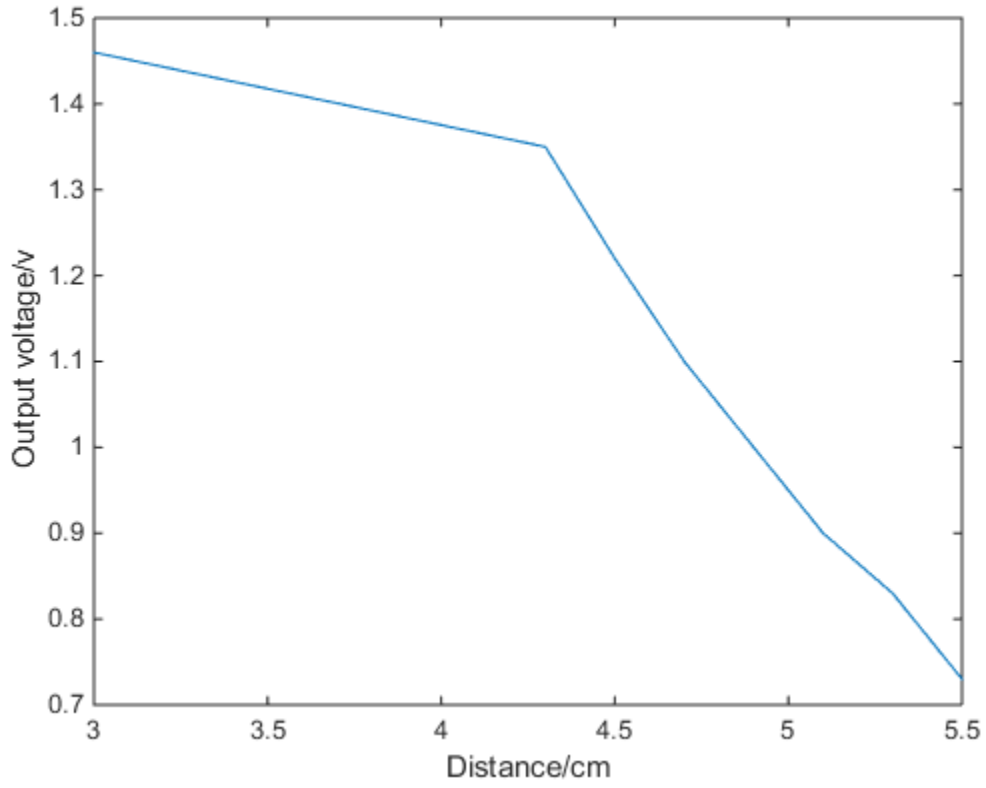

Fig. 6-5 Wireless charging voltage drop versus charging distance (from telemeter to the sensor tag) increase

6.4 Sensor

The pressure sensor could be either capacitive or piezo-resistive. Fig 6-6 is a prototype of the capacitance pressure sensor. MPX 2010 piezo-resistive pressure sensor is also a choice. This part

is my colleague Xuan Zhang's work.

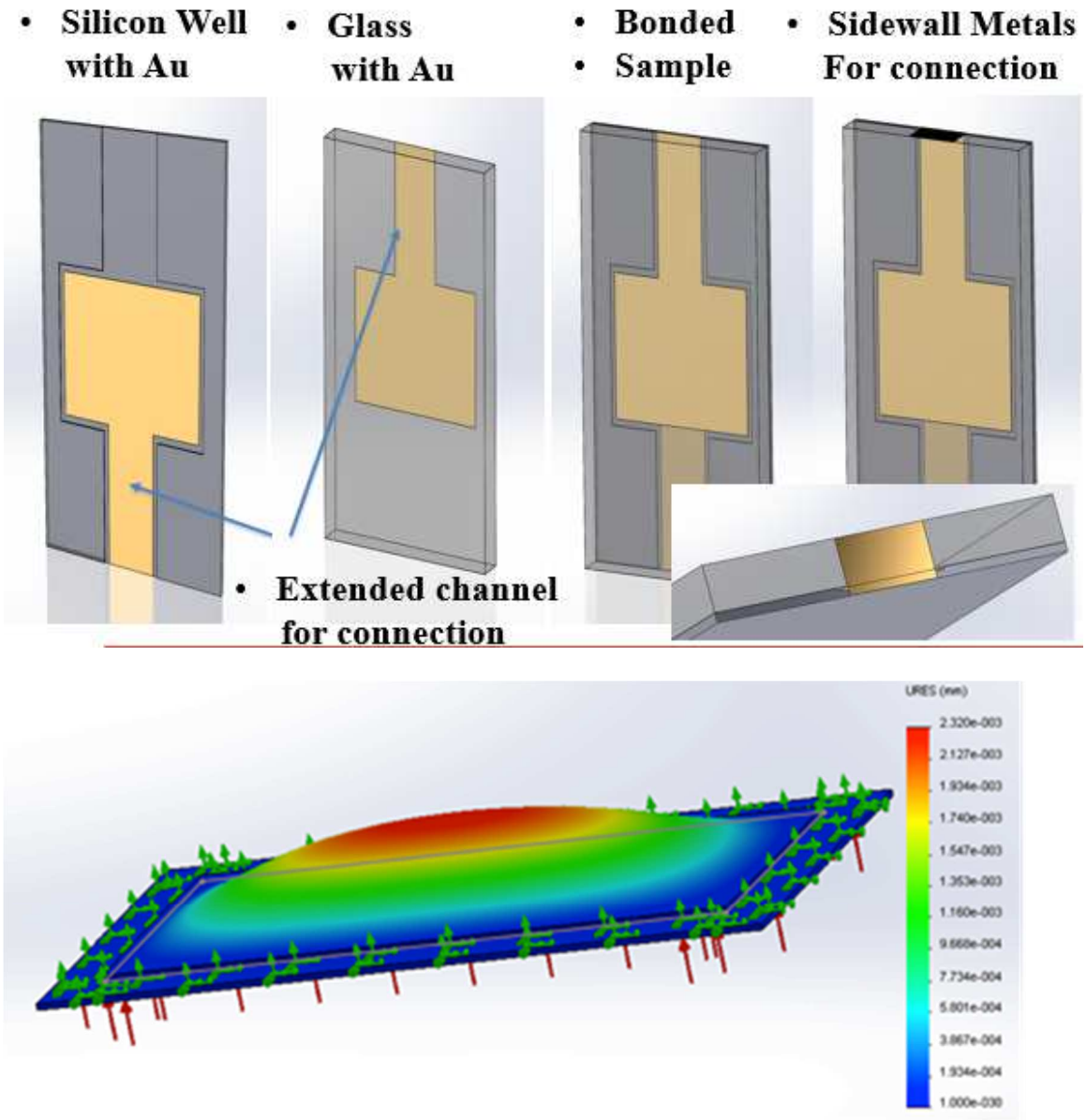

Fig.6-6 Capacitive pressure sensor

6.5 Valve driver

The DRV8662 (Texas Instruments Inc) is a single piezo haptic IC chip (4 × 4 × 0.9 mm) that contains an integrated differential amplifier and a booster. It can drive the piezoelectric valve up to 200 Vpp with fast transition time.

To perform efficiently, a smart shunt system requires a microcontroller that has an analog to digital converter (ADC) with a minimum sampling rate of 100 Hz for collecting ICP data, the ability to perform denoising and a moving window averager, a timer that helps to set up the interval window for updating the ICP average value, and the capability of sending an output signal to the control booster circuit according to the ICP average value. A microcontroller from Microchip Technology Inc. has been chosen (dspic30f4013).

The controlling algorithm is the programmable closed-loop system. Pressure sensor data will be sent to the controlling system directly. Local Regression, which is an advanced signal processing algorithm compared to the moving average, was applied to the raw data to denoise and smooth the signal. After signal denoising, a wavelet transform will be applied to the signal. The low frequency range (DC level) result representing the averaged ICP and shunt would be controlled based on that. The high frequency range result representing the percussion wave, rebound wave and dichrotic wave information can be further analyzed by the physician.

The averaged ICP is the key feature to control the shunt. If ICP is higher than the pre-set threshold TH ,(normally 12 mmHg), the shunt will open for T3 to release ICP. To save battery, the whole controlling system will only work continuously when necessary. Normally it sleeps for T1 and then is active for T2. T1, T2, T3, TH could be programed using the reader by the physician as shown in figure 6-7.

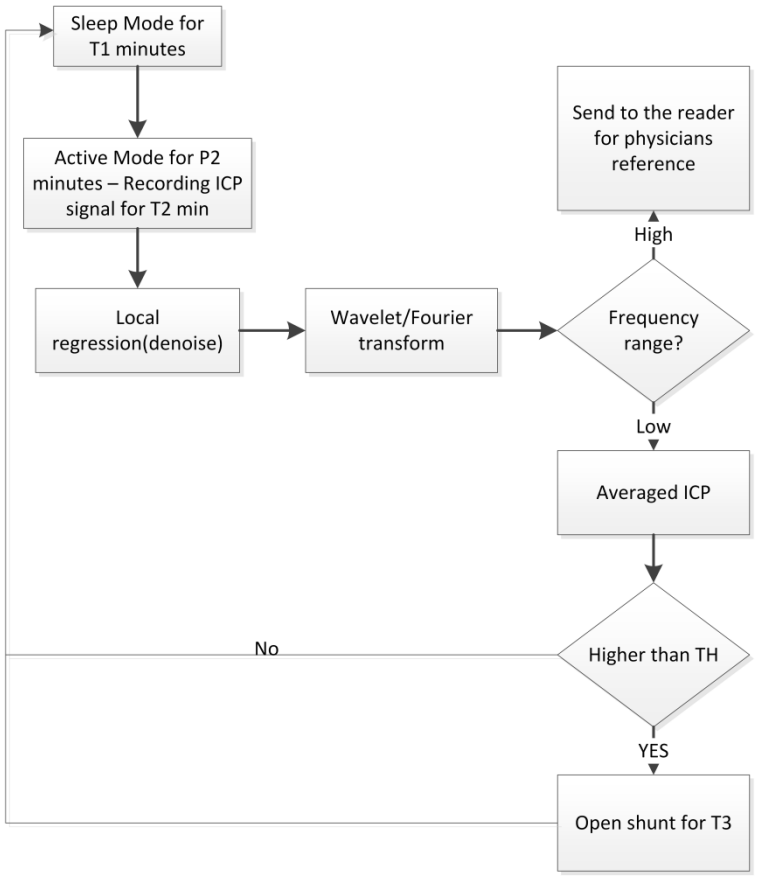

Fig.6-7 Smart shunt controlling algorithm flowchart

6.6 Valve

The valve is piezo-bender based, as shown in Fig.6-8. This part of work is done by colleague Mehdi Shokoueinejad.

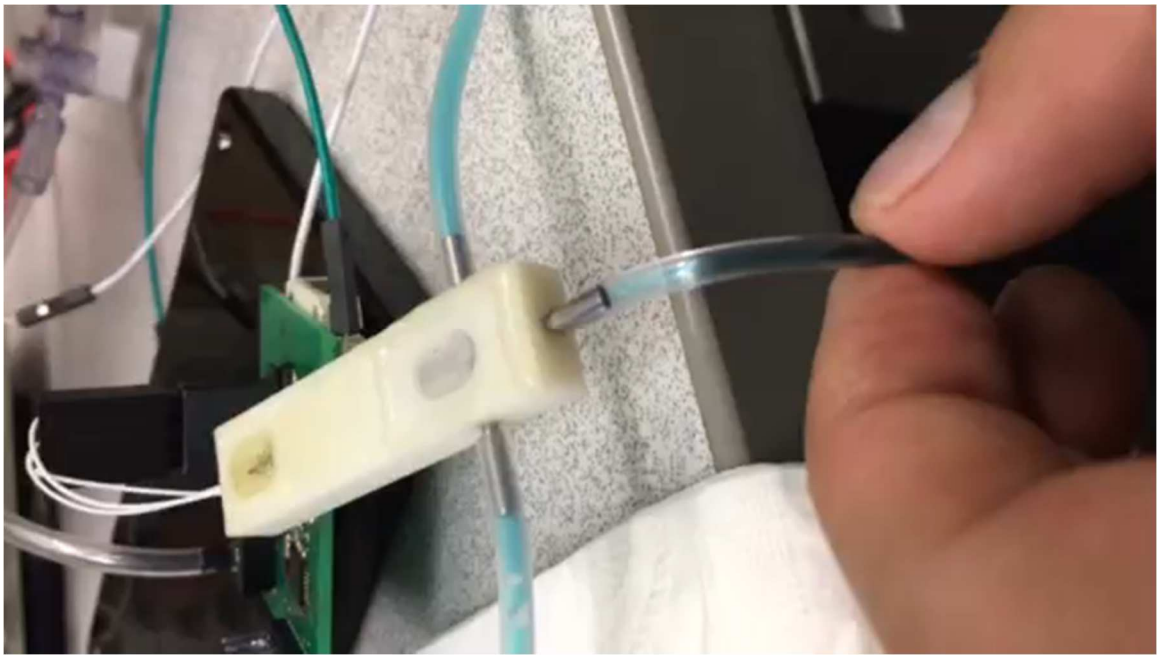

Fig.6-8. Piezo shunt valve

6.7 Ambient pressure sensor

An ambient pressure sensor could provide ambient pressure data for calibration when the patient is not at sea level. BME280 (SparkFun Electronics) module is chosen, which could build I2C commutation protocol to the external telemeter to provide real-time ambient pressure data.

6.8 SAR

We developed a COMSOL stimulation to test our prototype's SAR simulation. The antenna was placed 1 mm away from the left side of the head. Fig. 6-9 demonstrates that spatial peak SAR is less than 5 W/kg as averaged over 1 g of tissue, which is below the IEEE regulations maximal 8 W/kg as averaged over 1 g of tissue and 0.4 W/kg as averaged over the whole body.

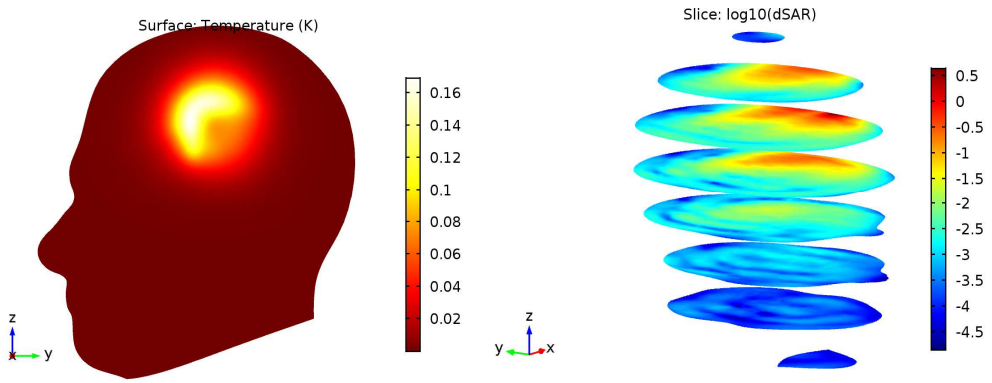

Fig. 6-9. Biosafety simulation result. Left is the simulation model in COMSOL. PCB antenna is placed close to the left side of the human head. Right is the SAR distribution in the head tissue. The result is in log scale.

CHARPTER 7: CONCLUSION

This dissertation presents a wearable read out system for a passive resonance pressure sensor to be used for wireless continuous ICP monitoring. The reader can work over a wide frequency range, which gives the reader freedom to design different size/different pattern sensors, for which resonant frequency may vary. This reader can work at high frequency, which can be used with ultra-small size sensors, which always resonate at high frequencies. The fine resolution and low phase noise allow the reader to detect small pressure changes. The whole design could be packaged into a helmet, with small weight (<50 g), which provides automatic and continuous daily ICP monitoring.

The ICP sensor design is also improved. Based on an improved circuit model of the ICP sensor, this paper proposed two formulas to predict resonant frequency range and the amplitude of the measured signal strength, with simple sensor physical parameters. The optimizational method for each parameter has been discussed. The design, fabrication and measurement of the ICP sensor based on this optimization method have been presented.

Besides the passive sensor and its read out system, an active sensor and its read out system are also presented. This system works as negative feedback controlling system for the ICP smart shunt valve. A prototype is developed to verify the functionality.

REFERENCES:

Akar, O., Akin, T., & Najafi, K. (2001). A wireless batch sealed absolute capacitive pressure sensor. Sensors and Actuators A: Physical, 95(1), 29-38.

Allocca J A 1980 *Method and apparatus for noninvasive monitoring of intracranial pressure* U.S. Patent 4,204,547

Alperin N J, Lee S H, Loth F, Raksin P B and Lichtor T 2000 MR-Intracranial Pressure (ICP): A method to measure intracranial elastance and pressure noninvasively by means of MR Imaging: baboon and human study 1 *Radiology* **217** 877–85

Alperin N, Hushek S G, Lee S H, Sivaramakrishnan A and Lichtor T 2005 MRI study of cerebral blood flow and CSF flow dynamics in an upright posture: the effect of posture on the intracranial compliance and pressure In Kirkness C J et al. (eds) *Intracranial Pressure and Brain Monitoring XII* (Springer; Vienna) pp. 177–81

Anderson R C, Kan P, Klimo P, Brockmeyer D L, Walker M L and Kestle J R 2004 Complications of intracranial pressure monitoring in children with head trauma *J. Neurosurg.: Pediatrics* **101** 53–8

Anonymous 2000 The Brain Trauma Foundation. The American Association of Neurological Surgeons. The Joint Section on Neurotrauma and Critical Care. Recommendations for intracranial pressure monitoring technology *J. Neurotraum.* **17** 497–506

Antes S, Tschan C A, Kunze G, Ewert L, Zimmer A, Halfmann A and Oertel J 2014 Clinical and radiological findings in long-term intracranial pressure monitoring. *Acta Neurochir.* **156** 1009–19

Asiedu D P, Lee K J, Mills G and Kaufmann E E 2014 A Review review of non-invasive methods of monitoring intracranial pressure *J. Neurolog. Res.* **4** 1–6

Avan P, Büki B, Lemaire J J, Dordain M and Chazal J 1996 Otoacoustic emissions: a new tool for monitoring intracranial pressure *InIntracranial and intralabyrinthine fluids* (Springer; Berlin Heidelberg) 165–73

Bauer D F, Razdan S N, Bartolucci A A and Markert J M 2011 Meta-analysis of hemorrhagic complications from ventriculostomy placement by neurosurgeons *Neurosurgery* **69** 255–60

Baurmann M 1925 Über die entstehung und klinische bedeutung des netzhautvenenpulses *Dtsch. Ophthalmol. Ges.* **45** 53–9

Beer R, Lackner P, Pfausler B and Schmutzhard E 2008 Nosocomial ventriculitis and meningitis in neurocritical care patients *J. Neurol.* **255** 1617–24

Bekar A, Doğan Ş, Abaş F, Caner B, Korfalı G, Kocaeli H, Yılmazlar S and Korfalı E 2009 Risk factors and complications of intracranial pressure monitoring with a fiberoptic device *J. Clin. Neurosci.* **16** 236–40

Berlin T, Murray-Krezan C and Yonas H 2015 Comparison of parenchymal and ventricular intracranial pressure readings utilizing a novel multi-parameter intracranial access system. *SpringerPlus* **4** 10

Bershad E M, Urfy M Z, Pechacek A, McGrath M, Calvillo E, Horton N J and Voss S E 2014 Intracranial pressure modulates distortion product otoacoustic emissions: A proof-of-principle study *Neurosurgery* **75** 445–55

Bhatia A and Gupta A K 2007 Neuromonitoring in the intensive care unit. I. Intracranial pressure and cerebral blood flow monitoring *Intens. Care Med*. **33** 1263–71

Binz D D, Toussaint III L G, and Friedman J A 2009 Hemorrhagic complications of ventriculostomy placement: a meta-analysis *Neurocrit. Care* **10** 253–6

Borchert M S and Lambert J L 1998 Non-invasive measurement of intracranial pressure WO Patent 98034536

Borchert M S and Lambert J L 2000 *Non-invasive method of measuring cerebral spinal fluid pressure* U.S. Patent 6,129,682

Brain T F 2007 Guidelines for the management of severe traumatic brain injury. V. Deep vein thrombosis prophylaxis *J. Neurotraum.* **24** S32

Bratton S L, Chestnut, R M, Ghajar J, McConnell H F, Harris O A, Hartl R, Manley GT, Nemecek A, Newell DW, Rosenthal G and Schouten J 2006 Guidelines for the management of severe traumatic brain injury. VII. Intracranial pressure monitoring technology *J. Neurotraum.* **24** S45–54

Bruce B B 2014 Noninvasive assessment of cerebrospinal fluid pressure *J. Neuro-Ophthalmol.* **34** 288–94

Bruder N, N'Zoghe P, Graziani N, Pelissier D, Grisoli F and François G 1995 A comparison of extradural and intraparenchymatous intracranial pressures in head injured patients *Intens. Care Med*. **21** 850–2

Büki B, Giraudet F and Avan P 2009 Non-invasive measurements of intralabyrinthine pressure changes by electrocochleography and otoacoustic emissions *Hearing Res.* **251** 51–9

Butler, J. C., Vigliotti, A. J., Verdi, F. W., & Walsh, S. M. (2002). Wireless, passive, resonant-circuit, inductively coupled, inductive strain sensor. Sensors and Actuators A: Physical, 102(1), 61-66.

Bullock M R and Povlishock J T 2007 Guidelines for the management of severe traumatic brain injury Editor's Commentary *J. Neurotraum.* **24** Suppl 1:2 p preceding S1.

Chen H, Wang J, Mao S, Dong W and Yang H 2012 A new method of intracranial pressure monitoring by EEG power spectrum analysis *Can. J. Neurol. Sci.* **39** 483–7

Chen L Y, Tee B C K, Chortos A L, Schwartz G, Tse V, Lipomi D J, Wong H S P, McConnell M V and Bao Z 2014 Continuous wireless pressure monitoring and mapping with ultra-small passive sensors for health monitoring and critical care. *Nat. Commun*. **5** 5028

Chen, P. J., Saati, S., Varma, R., Humayun, M. S., & Tai, Y. C. (2010). Wireless intraocular pressure sensing using microfabricated minimally invasive flexible-coiled LC sensor implant. Journal of Microelectromechanical Systems, 19(4), 721-734.

Chitnis, G., Maleki, T., Samuels, B., Cantor, L. B., & Ziaie, B. (2013). A minimally invasive implantable wireless pressure sensor for continuous IOP monitoring. IEEE Transactions on Biomedical Engineering, 60(1), 250-256.

Citerio G, Piper I, Chambers I R, Galli D, Enblad P, Kiening K, Ragauskas A, Sahuquillo J and Gregson B 2008 Multicenter clinical assessment of the raumedic neurovent–P intracranial pressure sensor: a report by the Brainit group *Neurosurgery* **63** 1152–8

Cleveland, W. S., & Loader, C. (1996). Smoothing by local regression: Principles and methods. In Statistical theory and computational aspects of smoothing (pp. 10-49). Physica-Verlag HD.

Collins, Carter C. "Miniature passive pressure transensor for implanting in the eye." IEEE Transactions on Biomedical Engineering 2 (1967): 74-83.

Comsol, COMSOL Multiphysics: Version 4.2: Comsol, 2011.

Coosemans, Johan, Michael Catrysse, and Robert Puers. "A readout circuit for an intra-ocular pressure sensor." Sensors and Actuators A: Physical 110.1 (2004): 432-438.

Czosnyka M and Pickard J D 2004 Monitoring and interpretation of intracranial pressure *J. Neurol. Neurosur. Ps.* **75** 813–21

Czosnyka M, Czosnyka Z and Pickard J D 1996 Laboratory testing of three intracranial pressure microtransducers: technical report *Neurosurgery* **38** 219–24

Dasic D, Hanna S J, Bojanic S and Kerr R C 2006 External ventricular drain infection: the effect of a strict protocol on infection rates and a review of the literature *Brit. J. Neurosurg.* **20** 296–300

Di Ieva A Schmitz E M and Cusimano M D 2013 Analysis of intracranial pressure past, present, and future *Neuroscientist* 1073858412474845

Du R, Meeker M, Bacchetti P, Larson M D, Holland M C and Manley G T 2005 Evaluation of the portable infrared pupillometer *Neurosurgery* **57** 198–203

Dunn L T 2002 Raised intracranial pressure *J. Neurol. Neurosur. Ps.* **73** i23–7

Duschek S and Schandry R 2007 Reduced brain perfusion and cognitive performance due to constitutional hypotension. *Clin. Auton. Res.* **17** 69–76

Eide PK 2006 A new method for processing of continuous intracranial pressure signals. *Med. Eng. Phys.* **28**: 579–87

Eide P K 2008 Comparison of simultaneous continuous intracranial pressure (ICP) signals from ICP sensors placed within the brain parenchyma and the epidural space *Med. Eng. Phys.* **30** 34–40

Eide P K and Brean A 2006 Lumbar cerebrospinal fluid pressure waves versus intracranial pressure waves in idiopathic normal pressure hydrocephalus *Brit. J. Neurosurg.* **20** 407–14

Eide P K and Sæhle T 2010 Is ventriculomegaly in idiopathic normal pressure hydrocephalus associated with a transmantle gradient in pulsatile intracranial pressure? *Acta Neurochir.* **152** 989–95

English, J. M., & Allen, M. G. (1999, January). Wireless micromachined ceramic pressure sensors. In Micro Electro Mechanical Systems, 1999. MEMS'99. Twelfth IEEE International Conference on (pp. 511-516). IEEE.

Firsching R, Müller C, Pauli S U, Voellger B, Röhl F W and Behrens-Baumann W 2011 Noninvasive assessment of intracranial pressure with venous ophthalmodynamometry: Clinical article. *J. Neurosurg.* **115** 371–4

Fountas K N, Kapsalaki E Z, Machinis T G, Boev A N, Robinson III J S and Troup E C 2006 Clinical implications of quantitative infrared pupillometry in neurosurgical patients *Neurocrit. Care* **5** 55–60

Fountas K N, Sitkauskas A, Feltes CH, Kapsalaki E Z, Dimopoulos V G, Kassam M, Grigorian A A, Robinson J S and Ragauskas A, 2005 Is non-invasive monitoring of intracranial pressure waveform analysis possible? Preliminary results of a comparative study of non-invasive vs. invasive intracranial slow-wave waveform analysis monitoring in patients with traumatic brain injury *Med Sci. Monit.* **11** CR58–63

Fried H I, Nathan B R, Rowe A S, Zabramski J M, Andaluz N, Bhimraj A, Guanci M M, Seder D B and Singh J M 2016 The insertion and management of external ventricular drains: an evidence-based consensus statement*Neurocrit. Care* **24**(1) pp. 61-81

Freimann F B, Sprung C, Chopra S S, Vajkoczy P and Wolf S 2013 Large-scale referencing of the telemetric Neurovent-P-tel intracranial pressure sensor in a porcine model. *Pediatr. Neurosurg.* **49** 29–32

Gaab M R, Heissler H E and Ehrhardt K 1989 Physical characteristics of various methods for measuring ICP *Intracranial Pressure VII* (Springer; Berlin Heidelberg) pp. 16–21

Gaihede M, Felding J U and Elbrônd O 1995 Biomechanical characteristics of the middle ear system measured by a new method: III: Comparisons with tympanometric measurements *Acta oto-laryngol.* **115** 522–7

Gardner P A, Engh J, Atteberry D and Moossy J J 2009 Hemorrhage rates after external ventricular drain placement: clinical article *J. Neurosurg.* **110** 1021–5

Geeraerts T, Merceron S, Benhamou D, Vigué B and Duranteau J 2008a Noninvasive assessment of intracranial pressure using ocular sonography in neurocritical care patients *Crit. Care* **12** 1–2

Gelabert-Gonzalez M, Ginesta-Galan V, Sernamito-Garcia R, Allut A G, Bandin-Dieguez J and Rumbo R M 2006 The Camino intracranial pressure device in clinical practice. Assessment in a 1000 cases *Acta Neurochir. (Wien)* **148** 435–41

Gevorgian, S., et al. "Application notes-basic parameters of coplanar-strip waveguides on multilayer dielectric/semiconductor substrates, Part 1: high permittivity superstrates." IEEE microwave magazine 4.2 (2003): 60-70.

Ghajar J 1995 Intracranial pressure monitoring techniques *New Horiz.* **3** 395–9

Glick R P, Niebruegge J, Lee S H, Egibor O, Lichtor T and Alperin N 2006 Early experience from the application of a noninvasive magnetic resonance imaging-based measurement of intracranial pressure in hydrocephalus *Neurosurgery* **59** 1052–61

Graham D I, Gennarelli T A, Cooper P R, and Golfinos J G 2000 Pathology of brain damage after head injury. In P R Cooper and J Golfinos (eds) *Head injury* 4th edn (New York: McGraw-Hill) 133–54

Guild S J, McBryde F D and Malpas S C 2015 Recording of intracranial pressure in conscious rats via telemetry *J. Appl. Physiol.* **119** 576–81

Hanlo P W, Gooskens R H J M, Faber J A J, Peters R J A, Nijhuis A A M, Vandertop W P, Tulleken C A F and Willemse J 1996 Relationship between anterior fontanelle pressure measurements and clinical signs in infantile hydrocephalus *Child Nerv. Syst.* **12** 200–9

Hanlo P W, Peters R J A, Gooskens R H J M, Heethaar R M, Keunen R W M, van Huffelen A C, Tulleken A F, and Willemse J 1995 Monitoring intracranial dynamics by transcranial Doppler—A new Doppler index: Trans systolic time *Ultrasound Med. Biol.* **21** 613–21

Hawthorne C and Piper I 2014 Monitoring of intracranial pressure in patients with traumatic brain injury *Front. Neurol.* **5** 121

Hee M R, Izatt J A, Swanson E A, Huang D, Schuman J S, Lin C P, Puliafito C A and Fujimoto J G 1995 Optical coherence tomography of the human retina *Arch. Ophthalmol-chic.* **113** 325–32

Hoefnagel D, Dammers R, Ter Laak-Poort M P and Avezaat C J J 2008 Risk factors for infections related to external ventricular drainage *Acta Neurochirur.* **150** 209–14

Hong W C, Tu Y K, Chen Y S, Lien L M and Huang S J 2006 Subdural intracranial pressure monitoring in severe head injury: clinical experience with the Codman MicroSensor *Surg. Neurol.* **66** S8–13

Hori, Hiroyuki, et al. "The thickness of human scalp: normal and bald." Journal of Investigative Dermatology 58.6 (1972): 396-399.

Hydrocephalus Association (2016) http://www.hydroassoc.org/

IEEE Standards Coordinating Committee 28, on Non-Ionizing Radiation Hazards. (1992). IEEE Standard for Safety Levels with Respect to Human Exposure to Radio Frequency Electromagnetic Fields, 3kHz to 300 GHz. Institute of Electrical and Electonics Engineers, Incorporated.

Jacks A S and Miller N R 2003 Spontaneous retinal venous pulsation: aetiology and significance *J. Neurol. Neurosur. Ps.* **74** 7–9

Jonas J B, Pfeil K, Chatzikonstantinou A and Rensch F 2008 Ophthalmodynamometric measurement of central retinal vein pressure as surrogate of intracranial pressure in idiopathic intracranial hypertension *Graef. Arch. Clin. Exp.* **246** 1059–60

Jonas J B, Wang N and Yang D 2012 Retinal vein pulsation is in phase with intracranial pressure and not intraocular pressure *Invest. Ophth. Vis. Sci.* **53** 6045

Jow, Uei-Ming, and Maysam Ghovanloo. "Design and optimization of printed spiral coils for efficient transcutaneous inductive power transmission." IEEE Transactions on biomedical circuits and systems 1.3 (2007): 193-202.

Kang S K, Murphy R K, Hwang S W, Lee S M, Harburg D V, Krueger N A, Shin J, Gamble P, Cheng H, Yu S and Liu Z 2016 Bioresorbable silicon electronic sensors for the brain *Nature* **530** 71–9

Kapadia F N and Jha A N 1996 Simultaneous lumbar and intraventricular manometry to evaluate the role and safety of lumbar puncture in raised intracranial pressure following subarachnoid haemorrhage *Brit. J. Neurosurg.* **10** 585–8

Kaiser, S. T. J. "Passive telemetric readout system." IEEE Sensors Journal 6.5 (2006): 1340-1345.

Kashif F M, Verghese G C, Novak V, Czosnyka M, and Heldt T 2012 Model-based noninvasive estimation of intracranial pressure from cerebral blood flow velocity and arterial pressure *Sci. Transl. Med.* **4** 129ra44

Kawoos U, Meng X, Huang S M, Rosen A, McCarron R M and Chavko M 2014 Telemetric intracranial pressure monitoring in blast-induced traumatic brain injury *IEEE Trans. Biomed. Eng.* **61** 841–7

Kawoos U, Mugalodi G K, Tofighi M R, Neff S and Rosen A 2005 April A permanently implantable intracranial pressure monitor *Proc. IEEE 31st Annu. Northeast Bioeng. Conf., 2005.* 17–9

Kemp D T 1978 Stimulated acoustic emissions from within the human auditory system *J. Acoust. Sci. Am.* **64** 1386–91

Kiefer M, Antes S, Leonhardt S, Schmitt M, Orakcioglu B, Sakowitz O W and Eymann R 2012 Telemetric ICP measurement with the first CE-approved device: data from animal experiments and initial clinical experiences *Acta Neurochir. Suppl.* **114** 111–6

Kiening K L, Schoening W N, Stover J F and Unterberg A W 2003 Continuous monitoring of intracranial compliance after severe head injury: relation to data quality, intracranial pressure and brain tissue PO2 *Brit. J. Neurosurg.* **17** 311–8

Kiening K L, Schoening W, Unterberg A W, Stover J F, Citerio G, Enblad P and Nilsson P 2005 Assessment of the relationship between age and continuous intracranial compliance *In Intracranial Pressure and Brain Monitoring XII* pp. (Springer; Vienna) 293–7

Kim, S., Kim, H. J., Park, J. S., & Yang, S. S. (2001, April). Telemetry silicon pressure sensor of lc resonance type. In Design, Test, Integration, and Packaging of MEMS/MOEMS 2001 (pp. 452-462). International Society for Optics and Photonics.

Koskinen L O D and Olivecrona M 2005 Clinical experience with the intraparenchymal intracranial pressure monitoring Codman MicroSensor system *Neurosurgery* **56** 693–8

Lang J M, Beck J, Zimmermann M, Seifert V and Raabe A 2003 Clinical evaluation of intraparenchymal Spiegelberg pressure sensor *Neurosurgery* **52** 1455–9

Langfitt T W, Weinstein J D, Kassell N F and Simeone F A 1964 Transmission of increased intracranial pressure. I. Within the craniospinal axis *J. Neurosurg.* **21** 989–97

Larson M D and Muhiudeen I 1995 Pupillometric analysis of the 'absent light reflex' *Arch. Neurol-Chicago* **52** 369–72

Law, Samuel K. "Thickness and resistivity variations over the upper surface of the human skull." Brain topography 6.2 (1993): 99-109.

Levoy M, "The Stanford volume data archive," ed, 2002.

Lenfeldt N, Koskinen L O, Bergenheim A T, Malm J and Eklund A 2007 CSF pressure assessed by lumbar puncture agrees with intracranial pressure *Neurology* **68** 155–8

Lescot T, Reina V, Le Manach Y, Boroli F, Chauvet D, Boch A L and Puybasset L 2012 In vivo accuracy of two intraparenchymal intracranial pressure monitors *Applied Physiology in Intensive Care Medicine* **37** (Springer; Berlin Heidelberg) pp. 249–53

Levinsky A, Papyan S, Weinberg G, Stadheim T and Eide P K 2016. Non-invasive estimation of static and pulsatile intracranial pressure from transcranial acoustic signals. *Med. Eng. Phys.* **38** 47784

Li Z and Luo Y 2010 Finite element study of correlation between intracranial pressure and external vibration responses of human head. *Adv. Theor. Appl. Mech.***3** 139–49

Liebeskind D S, Marcinkevicius E, Pranevicius M, Pranevicius O, Ragauskas A, Matijosaitis V, Zakelis R, Petrikonis K, Rastenyte D, Piper I and Daubaris G 2013 Clinical assessment of noninvasive intracranial pressure absolute value measurement method *Neurology* **80** 507–8

Lilja A, Andresen M, Hadi A, Christoffersen D and Juhler M 2014 Clinical experience with telemetric intracranial pressure monitoring in a Danish neurosurgical center *Clin. Neurol. Neurosur.* **120** 36–40

Liu H, Wang W, Cheng F, Yuan Q, Yang J, Hu J and Ren G 2015 External ventricular drains versus intraparenchymal intracranial pressure monitors in traumatic brain injury: a prospective observational study *World Neurosurg.* **83** 794–800

Lozier A P, Sciacca R R, Romagnoli M F and Connolly Jr E S 2002 Ventriculostomy-related infections: a critical review of the literature *Neurosurgery* **51** 170–82

Luerssen T G 1997 Intracranial pressure: Current status in monitoring and management Semin. Pediatr. Neurol. **4** 146–55

Mack W J, King R G, Ducruet A F, Kreiter K, Mocco J, Maghoub A, Mayer S and Connolly Jr E S 2003 Intracranial pressure following aneurysmal subarachnoid hemorrhage: monitoring practices and outcome data *Neurosurg. Focus* **14** 1–5

Maloney-Wilensky E, Gracias V, Itkin A, Hoffman K, Bloom S, Yang W, Christian S and LeRoux PD 2009 Brain tissue oxygen and outcome after severe traumatic brain injury: A systematic review* *Crit. Care Med.* **37** 2057–63

Marchbanks R J 1989 Method and apparatus for measuring intracranial fluid pressure U.S. Patent 4,841,986

Marioli, Daniele, et al. "A new measurement method for capacitance transducers in a distance compensated telemetric sensor system." Measurement Science and Technology 16.8 (2005): 1593.

Mayhall C G, Archer N H, Lamb V A, Spadora A C, Baggett J W, Ward J D, and Narayan R K 1984 Ventriculostomy-related infections *New Engl. J. Med.* **310** 553–9

Medow. J Doctor's 2011 October 25 Madison doctor creates possible life-saving device for children with hydrocephalus *Wisconsin State Journal* http://host.madison.com/wsj/news/local/health_med_fit/madison-doctor-creates-possible-

life-saving-device-for-children-with/article_ba627bc2-fe9b-11e0-802d-001cc4c03286.html

Meeker M, Du R, Bacchetti P, Privitera C M, Larson M D, Holland M C and Manley G 2005 Pupil examination: validity and clinical utility of an automated pupillometer *J. Neurosci. Nurs.* **37** 34–40

Mertz K. Bencsik B, Büki B and Avan P 2004 Noninvasive testing of intracranial pressure changes due to body position in infants *Orv Hetil.* **145** 1427–30

Meng, Xu, et al. "Dynamic evaluation of a digital wireless intracranial pressure sensor for the assessment of traumatic brain injury in a swine model." IEEE Transactions on Microwave Theory and Techniques 61.1 (2013): 316-325.

Michaeli D 2000 *Noninvasive monitoring of intracranial pressure* WO Patent 00068647

Michaeli D and Rappaport Z H 2002 Tissue resonance analysis: a novel method for noninvasive monitoring of intracranial pressure: Technical note *J. Neurosurg.* **96** 1132–7

Mick E C 1991 *Method and apparatus for the measurement of intracranial pressure* U.S. Patent 5,074,310

Mick E C 1992 *Method and apparatus for the measurement of intracranial pressure* U.S. Patent 5,117,835

Miyake H, Ohta T, Kajimoto Y and Matsukawa M 1997 A new ventriculoperitoneal shunt with a telemetric intracranial pressure sensor: clinical experience in 94 patients with hydrocephalus *Neurosurgery* **40** 931–5

Mokri B 2001 The Monro–Kellie hypothesis applications in CSF volume depletion *Neurology* **56** 1746-8

Mohan, Sunderarajan S., et al. "Simple accurate expressions for planar spiral inductances." IEEE Journal of solid-state circuits 34.10 (1999): 1419-1424.

Morgalla M H, Cuno M, Mettenleiter H, Will BE, Krasznai L, Skalej M, Bitzer M and Grote E H 1997 ICP monitoring with a re-usable transducer: Experimental and clinical evaluation of the Gaeltec ICT/b pressure probe *Acta Neurochir.* **139** 569–73

Muehlmann M, Koerte I K, Laubender R P, Steffinger D, Lehner M, Peraud A, Heinen F, Kiefer M, Reiser M and Ertl-Wagner B 2013 Magnetic resonance–based estimation of intracranial pressure correlates with ventriculoperitoneal shunt valve opening pressure setting in children with hydrocephalus *Invest. Radiol.* **48** 543–7

Münch E C, Bauhuf C, Horn P, Roth H R, Schmiedek P and Vajkoczy P 2001 Therapy of malignant intracranial hypertension by controlled lumbar cerebrospinal fluid drainage *Crit. Care Med.* **29** 976–81

Neagu, C. R., et al. "Characterization of a planar microcoil for implantable microsystems." Sensors and Actuators A: Physical 62.1-3 (1997): 599-611.

Nopper, Reinhard, Remigius Niekrawietz, and Leonhard Reindl. "Wireless readout of passive LC sensors." IEEE Transactions on Instrumentation and Measurement 59.9 (2010): 2450-2457.

Olzowy B, von Gleichenstein G, Canis M and Mees K 2008 Distortion product otoacoustic emissions for assessment of intracranial hypertension at extreme altitude? *Eur. J. Appl. Physiol.* **103** 19–23

Park, E. C., Yoon, J. B., & Yoon, E. (1998). Hermetically sealed inductor-capacitor (LC) resonator for remote pressure monitoring. Japanese journal of applied physics, 37(12S), 7124.

Piper I 1997 Chapter 6 Intracranial pressure and elastance In Reilly P and Bullock R (eds) *Head Injury*. London: Chapman & Hall.

Piper I, Barnes A, Smith D and Dunn L 2001 The Camino intracranial pressure sensor: is it optimal technology? An internal audit with a review of current intracranial pressure monitoring technologies *Neurosurgery* **49** 1158–65

Pople I K, Muhlbauer M S, Sanford R A and Kirk E 1995 Results and complications of intracranial pressure monitoring in 303 children *Pediatr. Neurosurg.* **23** 64–7

Popovic D, Khoo M, and Lee S 2009 Noninvasive monitoring of intracranial pressure *Recent Patents on Biomedical Engineering* **2** 165–79

Poupko B Z, Reichman Y, Rappaport A and Ben-Ari S. 2012 *Non-invasive intracranial monitor* U.S. Patent 8,211,031

Pranevicius O, Pranevicius M, Pranevicius H, Marcinkevicius E and Liebeskind D S 2012 *Noninvasive method to measure intracranial and effective cerebral outflow pressure* U.S. Patent 8,109,880

Quincke H 1891 Lumbalpunktion des hydrocephalus *Berl. Klin. Wochenschr.* 929–33

Raabe A, Totzauer R, Meyer O, Stöckel R, Hohrein D and Schöche J 1998 Reliability of epidural pressure measurement in clinical practice: behavior of three modern sensors during simultaneous ipsilateral intraventricular or intraparenchymal pressure measurement *Neurosurgery* **43** 306–11

Raboel P H, Bartek J, Andresen M, Bellander B M, and Romner B 2012 Intracranial pressure monitoring: invasive versus non-invasive methods—a review *Crit. Care Res. Pract.* **2012** ID 950393

Ragauskas A 2006 *Method and apparatus for noninvasive determination of the absolute value of intracranial pressure* U.S. Patent 7,147,605

Ragauskas A, Bartusis L, Piper I, Zakelis R, Matijosaitis V, Petrikonis K and Rastenyte D 2014 Improved diagnostic value of a TCD-based non-invasive ICP measurement method compared with the sonographic ONSD method for detecting elevated intracranial pressure *Neurol. Res.* **36** 607–14

Ragauskas A, Daubaris G, Dziugys A, Azelis V and Gedrimas V 2005 Innovative non-invasive method for absolute intracranial pressure measurement without calibration *In Intracranial Pressure and Brain Monitoring XII* (Springer; Vienna) pp. 357–61

Ragauskas A, Daubaris G, Petkus V, Ragaisis V and Ursino M 2005 Clinical study of continuous non-invasive cerebrovascular autoregulation monitoring in neurosurgical ICU *In Intracranial Pressure and Brain Monitoring XII* (Springer; Vienna) pp. 367–70

Ragauskas A, Daubaris G, Ragaisis V and Petkus V 2003 Implementation of non-invasive brain physiological monitoring concepts *Med. Eng. Phys.* **25** 667–78

Ragauskas A, Matijosaitis V, Zakelis R, Petrikonis K, Rastenyte D, Piper I and Daubaris G 2012 Clinical assessment of noninvasive intracranial pressure absolute value measurement method *Neurology* **78** 1684–91

Ragauskas A.and Daubaris G 1995 *Method and apparatus for non-invasively deriving and indicating of dynamic characteristics of the human and animal intracranial media* U.S. Patent 5,388,583

Rai P and Varadan V K 2010 March Organic electronics based pressure sensor towards intracranial pressure monitoring *SPIE Smart Structures and Materials+ Nondestructive Evaluation and Health Monitoring* 764617

Rajajee V, Vanaman M, Fletcher J J and Jacobs T L 2011 Optic nerve ultrasound for the detection of raised intracranial pressure *Neurocrit. Care* **15** 506–15

Raju, Salahuddin, et al. "Modeling of mutual coupling between planar inductors in wireless power applications." IEEE Transactions on Power Electronics 29.1 (2014): 481-490.

Rangel-Castillo L, Gopinath S, and Robertson C S 2008 Management of intracranial hypertension *Neurol. Clin.* **26** 521–41

Reina, M. A., Lopez-Garcia, A., Dittmann, M., & De Andrés, J. A. (1996). Structural analysis of the thickness of human dura mater with scanning electron microscopy. Revista espanola de anestesiologia y reanimacion, 43(4), 135-137.

Rosenfeld J G Watts C and York D H 1986 *Method and apparatus for intracranial pressure estimation* U.S. Patent 4,564,022

Ross N and Eynon C A 2005 Intracranial pressure monitoring *Trends in Anaesthesia & Critical Care* **16** 255–61

Rossi S, Buzzi F, Paparella A, Mainini P and Stocchetti N 1998 Complications and safety associated with ICP monitoring: a study of 542 patients *Acta Neurochir Suppl.* **71** 91–3

Saladino A, White J B, Wijdicks E F and Lanzino, G 2009 Malplacement of ventricular catheters by neurosurgeons: a single institution experience *Neurocrit. Care* **10** 248–52

Schade R P, Schinkel J, Visser L G, Van Dijk J M C, Voormolen J H and Kuijper E J 2005 Bacterial meningitis caused by the use of ventricular or lumbar cerebrospinal fluid catheters *J. Neurosurg.* **102** 229–34

Schmidt B, Czosnyka M, Raabe A, Yahya H, Schwarze J J, Sackerer D, Sander D and Klingelhöfer J 2003 Adaptive noninvasive assessment of intracranial pressure and cerebral autoregulation *Stroke* **34** 84–9

Schmid, G., Neubauer, G., & Mazal, P. R. (2003). Dielectric properties of human brain tissue measured less than 10 h postmortem at frequencies from 800 to 2450 MHz. Bioelectromagnetics, 24(6), 423-430.

Schmutzhard J, Aregger FC, Otieno A, Bunk S, Zorowka P and Schmutzhard E 2013 Release of intracranial pressure leads to improvement of otoacoustic emissions–a case report of a Kenyan child with complicated tuberculous meningitis. *J. Trop. Pediatr.* **59**: 326–9

Sinha D N 2000 *Method for noninvasive intracranial pressure measurement* U.S. Patent 6,117,089

Soldatos T, Karakitsos D, Chatzimichail K, Papathanasiou M, Gouliamos A and Karabinis A 2008 Optic nerve sonography in the diagnostic evaluation of adult brain injury *Crit. Care* **12** R67

Speck V, Staykov D, Huttner H B, Sauer R, Schwab S and Bardutzky J 2011 Lumbar catheter for monitoring of intracranial pressure in patients with post-hemorrhagic communicating hydrocephalus *Neurocrit. Care* **14** 208–15

Stehlin E F, McCormick D, Malpas S C, Pontré B P, Heppner P A and Budgett D M 2015 MRI interactions of a fully implantable pressure monitoring device *J. Magn. Reson. Imaging* **42** 1441–9

Steiner L A and Andrews P J D 2006 Monitoring the injured brain: ICP and CBF *Brit. J. Anaesth.* **97** 26–38

Stendel R, Heidenreich J, Schilling A, Akhavan-Sigari R, Kurth R, Picht, T, Pietilä T, Suess O, Kern C, Meisel J and Brock M 2003 Clinical evaluation of a new intracranial pressure monitoring device *Acta Neurochir.* **145** 185–93

Stettin E, Paulat K, Schulz C, Kunz U and Mauer U M 2011 Noninvasive intracranial pressure measurement using infrasonic emissions from the tympanic membrane *J. Clin. Monitor. Comp.* **25** 203–10

Timoshenko, Stephen, and Sergius Woinowsky-Krieger. "Theory of plates and shells." (1959).

Tranquart F, Bergès O, Koskas P, Arsene S, Rossazza C, Pisella P J and Pourcelot L 2003 Color Doppler imaging of orbital vessels: personal experience and literature review *J. Clin. Ultrasound* **31** 258–73

Troedsson, Niklas, and Henrik Sjöland. "A distributed capacitance analysis of co-planar inductors for a CMOS QVCO with varactor tuned buffer stage." Analog Integrated Circuits and Signal Processing 42.1 (2004): 7-19.

Tse T S, Cheng K F, Wong K S, Pang K Y and Wong C K 2010 Ventriculostomy and infection: a 4-year-review in a local hospital *Surg Neurol Int.* **1** 47

Tsung J W, Blaivas M, Cooper A and Levick N R 2005 A rapid noninvasive method of detecting elevated intracranial pressure using bedside ocular ultrasound: application to 3 cases of head trauma in the pediatric emergency department *Pediatr. Emerg. Care* **21** 94–8

Tuettenberg J, Czabanka M, Horn P, Woitzik J, Barth M, Thomé C, Vajkoczy P, Schmiedek P and Muench E 2009 Clinical evaluation of the safety and efficacy of lumbar cerebrospinal fluid drainage for the treatment of refractory increased intracranial pressure: Clinical article *J. Neurosurg.* **110** 1200–8

Verweij B H, Muizelaar J P and Vias F C 2001 Hyperacute measurement of intracranial pressure, cerebral perfusion pressure, jugular venous oxygen saturation, and laser Doppler flowmetry, before and during removal of traumatic acute subdural hematoma *J. Neurosurg.* **95** 569–72

Voss S E, Horton N J, Tabucchi T H, Folowosele F O and Shera C A 2006 Posture-induced changes in distortion-product otoacoustic emissions and the potential for noninvasive monitoring of changes in intracranial pressure *Neurocrit. Care* **4** 251–7

Weerakkody R A, Czosnyka M, Zweifel C, Castellani G, Smielewski P, Keong N, Haubrich C, Pickard J and Czosnyka Z 2010 Slow vasogenic fluctuations of intracranial pressure and cerebral near infrared spectroscopy—an observational study *Acta Neurochir.* **152** 1763–9

Welschehold S, Schmalhausen E, Dodier P, Vulcu S, Oertel J, Wagner W and Tschan C A 2012 First clinical results with a new telemetric intracranial pressure-monitoring system *Neurosurgery* **70** Suppl 44–9

Wen, P. Y., and S. K. Teoh. "Clinical presentation and diagnosis of brain tumors." Office practice of neurology. 2nd ed. Philadelphia: Churchill Livingstone (2003): 1013-7.

Wen-Teng, Chang, and Lai Su-Hao. "Measuring reactive near-field interference using the quartz oscillators intermodulation." Electronics, Control, Measurement, Signals and their Application to Mechatronics (ECMSM), 2015 IEEE International Workshop of. IEEE, 2015.

Wiegand C and Richards P 2007 Measurement of intracranial pressure in children: a critical review of current methods *Dev. Med. Child Neurol.* **49** 935–41

Wu X and Ji Z 2007 Non-invasive detection for intracranial high pressure with FVEP picked-up by independent component analysis *Sheng Wu Yi Xue Gong Cheng Xue Xa Zhi* **24** 1015–8

Yang J, Charif A C, Puskas J E, Phillips H, Shanahan K J, Garsed J, Fleischman A, Goldman K, Luebbers M T, Dombrowski S M and Luciano M G 2015 Biocompatibility evaluation of a thermoplastic rubber for wireless telemetric intracranial pressure sensor coating *J. Mech. Behav. Biomed.* **45** 83–9

Yoon H J, Jung J M, Jeong J S and Yang S S 2004 Micro devices for a cerebrospinal fluid (CSF) shunt system *Sensors Actuat. A-Phys.* **110** 68–76

York D H, Pulliam M W, Rosenfeld J G and Watts C 1981 Relationship between visual evoked potentials and intracranial pressure *J. Neurosurg.* **55** 909–16

York D, Legan M, Benner S and Watts C 1984 Further studies with a noninvasive method of intracranial pressure estimation *Neurosurgery* **14** 456–61

Yue X and Wang L 2009 Deformation of skull bone as intracranial pressure changing *Afr. J. Biotechnol.* **8** 745–50

Yue X, Wang L, Sun S and Tong L 2008 Viscoelastic finite-element analysis of human skull-dura mater system as intracranial pressure changing *Afr. J. Biotechnol*. **7** 689–95

Zhang B O and Li S B 2012 Cine-PC MR in assessment of cerebrospinal fluid velocity in the aqueduct of the midbrain correlated with intracranial pressure–Initial study *Med. Hypotheses* **78** 227–30

Zhang X 2014 Intracranial Pressure Sensor *Master of Science in Electrical and Computer Engineering, University of Wisconsin-Madison*

Zhao Y L, Zhou J Y and Zhu G H 2005 Clinical experience with the noninvasive ICP monitoring system *Intracranial Pressure and Brain Monitoring XII* (Springer; Vienna) pp. 351–5

Zhong J, Dujovny M, Park H K, Perez E, Perlin A R and Diaz F G 2003 Advances in ICP monitoring techniques *Neurol. Res.* **25** 339–50

Zweifel C, Castellani G, Czosnyka M, Helmy A, Manktelow A, Carrera E, Brady K M, Hutchinson P J, Menon D K, Pickard J D and Smielewski P 2010 Noninvasive monitoring of cerebrovascular reactivity with near infrared spectroscopy in head-injured patients *J. Neurotraum.* **27** 1951-8.